A UNIFIED T-MATRIX APPROACH TO QUARK-GLUON PLASMA

A Dissertation

by

SHUAI LIU

Submitted to the Office of Graduate and Professional Studies of
Texas A&M University
in partial fulfillment of the requirements for the degree of

DOCTOR OF PHILOSOPHY

Chair of Committee,	Ralf Rapp
Committee Members,	Che-Ming Ko
	Saskia Mioduszewski
	Charles M. Folden III
Head of Department,	Grigory Rogachev

May 2018

Major Subject: Physics

ABSTRACT

We develop a non-perturbative microscopic approach to study the quark-gluon plasma (QGP), which treats all partons (light, heavy and static) in a unified framework. The starting point is a relativistic effective Hamiltonian using a universal color force. Employing a many-body T-matrix approach to solve the Hamiltonian non-perturbatively, we calculate three sets of lattice QCD (lQCD) "observables": the equation of state (EoS), the heavy quark (HQ) free energy ($F_{Q\bar{Q}}$), and quarkonium correlator ratios, to compare with corresponding lQCD data. Newly developed methods are introduced to calculate both $F_{Q\bar{Q}}$, using a static T-matrix, and EoS, using a resummed Luttinger-Ward functional. The lQCD benchmarks constrain the inputs to the Hamiltonian. We find that the solution describing the lQCD data is not unique. In order to determine the physical implications of the solutions, two limiting cases are explored: a weakly coupled solution (WCS), which has a weak color potential (close to free energy), resulting in sharp spectral functions (quasi-particle spectral functions), and weak but sharp resonances near T_c; and a strongly coupled solution (SCS), which has a strong color potential (much larger than free energy), resulting in broad (non-quasi-particle) parton spectral functions, and strong broad resonances near T_c. For a final determination of the microscopic picture of the QGP, these two solutions are used to evaluate the HQ transport coefficients and the QGP viscosity. The transport coefficients generated by the SCS are more consistent with phenomenological applications to heavy-ion collisions. Particularly, we implement HQ transport coefficients in the HQ Langevin simulations to generate heavy-meson spectra and compare with experimental results. We find that the SCS is consistent with experimental results.

To my wife and parents

ACKNOWLEDGEMENTS

This dissertation could never have been achieved without the help and support of special ones in my life.

I am most thankful for the guidance of my advisor, Prof. Ralf Rapp. He has helped me through difficult times. From the many discussions with him, I gained unique knowledge and many insights, which inspired ideas to solve problems. His passion and dedication to our research encouraged me to move forward when faced with difficulties. Also, I would like to express special thanks to Prof. Che-Ming Ko, Prof. Saskia Mioduszewski, and Prof. Charles M. Folden III, for their valuable time serving as my committee members, and their many suggestions for my research and dissertation.

Also, I would like to thank our group members and my friends: Prof. Min He, Prof. Xingbo Zhao, Prof. Nathan Holt, Dr. Paul Hohler, Dr. Feng Li, Dr. Zhen Zhang, Dr. Zilong Chang, Xiaojian Du, Joseph Atchison, Isaac Sarver, Yifeng Sun, Zhidong Yang. The disscussions with them are always fruitful and enjoyable, and I learned varied and interesting knowledge and insights from them.

At last, I need to thank my wife and my parents. They create a pleasant and harmonious environment, which allows me to stay happy and well motivated. When I am feeling down, they always encourage and support me to regain my strength.

CONTRIBUTORS AND FUNDING SOURCES

Contributors

This work was supported by a dissertation committee consisting of Professor Ralf Rapp, Professor Che-Ming Ko and Professor Saskia Mioduszewski of the Department of Physics & Astronomy and Professor Charles M. Folden III of the Department of Chemistry.

The Langevin simulation data in Chapter 5 was provided by Professor Min He. All other work conducted for the dissertation was completed by the student under the supervision of Professor Ralf Rapp of the Department of Physics & Astronomy.

Funding Sources

This work is supported by the U.S. NSF through grant no. PHY-1614484 and PHY-1306359.

NOMENCLATURE

3D/4D	3 or 4 dimension
BbS	Blankenbecler Sugar Scheme
BCS	Bardeen-Cooper-Schrieffer theory for superconductor
BEC	Bose-Einstein Condensation
BSE	Bethe-Salpeter Equation
CM	Center of Mass
EoS	Equation of State
HF	Heavy Flavor
HICs	Heavy Ion Collisions
HQ	Heavy Quark
lQCD	Lattice QCD
LWB	Luttinger-Ward-Baym
LWF	Luttinger-Ward Functional
pQCD	Perturbative QCD
QCD	Quantum Chromodynamics
QED	Quantum Electrodynamics
QGP	Quark-Gluon Plasma
SCS	Strongly Coupled Solution
URHIC	Ultra Relativistic Heavy Ion Collision
WCS	Weakly Coupled Solution

TABLE OF CONTENTS

Page

LIST OF FIGURES

LIST OF TABLES

TABLE Page

1. INTRODUCTION*

The last few hundred years have been an era of accelerated advancement in physics. As a result, present-day experiments using particle colliders allow us to explore distances many orders of magnitude smaller than the radius of a proton (near 10^{-15} m). This has led to the development of the Standard Model—a theory that describes the fundamental building blocks of nature (quarks, leptons, gauge bosons, Higgs boson) and their interactions. With these building blocks, one of the most important tasks for our generation is to use them to reconstruct the complex phenomena in our universe. However, this has proved to be a highly non-trivial task. As Anderson emphasizes, "The ability to reduce everything to simple fundamental laws does not imply the ability to start from those laws and reconstruct the universe" [9]. Toward this end, we are faced with challenges and difficulties no less than those of discovering new fundamental principles. Research in condensed matter physics works toward these goals, reconstructing the many-body emergent phenomena part of the Standard Model—quantum electrodynamics (QED), resulting in an understanding of the properties of crystals, superconductivity in metals, and many other complex phenomena. Similarly, research in the many-body problem of quantum chromodynamics (QCD), which is QCD matter physics, attempts to understand how phenomena such as chiral symmetry breaking, confinement and deconfinement, and phase structures of QCD matter, are emergent from QCD—another part of the Standard Model. This dissertation is an attempt (in the campaign of reconstructing our universe) to provide insights into how marvelous features of quark-gluon plasma (QGP), as one phase of QCD matter, are emergent from underlying microscopic physics.

In the remainder of this introduction, we briefly introduce the fundamental theory of

*Part of section 1.4 is reprinted with permission from "T-matrix approach to quark-gluon plasma" by Shuai Y. F. Liu and Ralf Rapp, 2018, Phys. Rev. C **97**, 034918, Copyright 2018 by APS.

the strong force (QCD) in Sec. 1.1, the main features of QCD—asymptotic freedom and confinement—in Sec. 1.2, and the QGP—a many-body system governed by QCD—in Sec. 1.3. In Sec. 1.4, we briefly discuss the motivation, objective and the outline of this dissertation.

1.1 QCD as a Fundamental Theory for Strong Force

The fundamental theory describing the strong interactions between quarks is QCD, for which the force carrier is the gluon. These fundamental particles obey SU(3) non-Abelian gauge symmetry and their dynamics are described by the Lagrangian [10]

$$L = -\frac{1}{4}(F^a_{\mu\nu})^2 + \sum_f^{N_f} \bar{\psi}_f (i\gamma^\mu D_\mu - m_i)\psi_f, \tag{1.1}$$

where ψ_f is the field operator for different quark flavors, and N_f is the number of flavors included. Usually, we only consider the 3 light flavors, which are up (u), down (d) and strange (s) quarks. In the studies of heavy quarks, the charm (c), bottom (b) and top (t) quarks are also included. The covariant derivative in Eq. (1.1) is

$$D_\mu = \partial_\mu - igA^a_\mu t^a_r\,, \tag{1.2}$$

where $t^a = \lambda^a/2$ is the group generator in the SU(3) fundamental representation, and λ^a is the 3×3 Gell-Mann matrix that acts on the color index of the quarks. More explicitly, $(t^a)_{ij}(\psi_f)_j$ describes an interaction in which a gluon "a" flips the color vector $\{(\psi_f)_1, (\psi_f)_2, (\psi_f)_3\}$ of a quark to another vector using the matrix $(t^a)_{ij}$. The field strength tensor $F^a_{\mu\nu}$ for gluon "a" is given by

$$F^a_{\mu\nu} = \partial_\mu A^a_\nu - \partial_\nu A^a_\mu + g f^{abc} A^a_\mu A^b_\nu. \tag{1.3}$$

The structure constant f^{abc} is defined by the commutator $[t^a, t^b] = if^{abc}t^c$, which is non-vanishing, and, therefore, defines a non-Abelian group. Defining $(t^b_G)_{ac} = if^{abc}$, the t^b_G obeys the same Lie algebra $[t^a_G, t^b_G] = if^{abc}t^c_G$ as the t^a. Thus, t^a_G is just another representation of the Lie group which is called adjoint representation. The "a" has 8 choices $a \in (1 \ldots 8)$, so that the gluon has 8 colors (combinations). The third term in Eq. (1.3) represents the gluon (force carrier) self-interaction in non-Abelian gauge theory, which generates many new features, when compared to Abelian gauge theory. Gauge invariance requires a universal coupling constant g for quark-gluon and gluon-gluon interactions. However, the matrix structures in t^a and f^{abc} lead to different interactions between color states, fully constrained by these matrices. The QCD Lagrangian Eq. (1.1) may be expressed more explicitly as

$$\begin{aligned} L =& L_0 + gA^a_\lambda \bar{\psi}_i \gamma^\lambda t^a \psi_i - gf^{abc}(\partial_\kappa A^a_\lambda A^{\kappa b} A^{\lambda c}) - g^2 f^{eab} A^a_\kappa A^b_\lambda f^{ecd} A^c_\kappa A^d_\lambda \\ & - f^{abc}\bar{c}^a \partial_\lambda A^{b\lambda} \bar{c}^c, \end{aligned} \tag{1.4}$$

where

$$L_0 = \bar{\psi}_i(i\gamma^\mu \partial_\mu - m_i)\psi_i + \frac{1}{2}A_\mu(\partial^2 g^{\mu\nu} - (1 - \frac{1}{\xi})\partial^\mu \partial^\nu)A_\nu + \bar{c}(-\partial^2)c. \tag{1.5}$$

Two terms in this equation are related with the gauge fixing for non-Abelian gauge theory. The $1/\xi$ is an artificial gauge parameter generated by using a Gaussian to average for the gauge fixing condition where ξ is useful for checking the gauge invariance of the final results. The ghost field c arises when representing the determinant by a Grassmann integral. Thus, the c field is an anti-commuting scalar field. With this gauge fixing procedure, the theory is quantized and provides gauge-invariant amplitudes, even with loop corrections. There are other ways to quantize the theory, but this method is manifestly Lorentz invariant

and is usually referred to as the Faddeev-Popov method. The free term, Eq. (1.5), defines the propagators, and the interaction term in Eq. (1.4) specifies the vertex structures that generate the Feynman rules that are used to investigate many-body processes, including virtual excitations from vacuum or a thermal medium. In the perturbative context, all the physical amplitudes can be generated by Feynman rules with proper treatment of renormalization. The Feynman rules define the color interaction (force) between two particles in different color channels. However, for the two-body case, we usually need only the total amplitude of the sum of 8 colors of gluons, resulting in a much simpler description. This simpler description is used throughout this dissertation and is discussed in more details below.

The matrix coupling with summed "a" proportional to the tensor product $(t^a)_{ij}(t^a)_{kl}$ for quark-quark interactions has a compact form,

$$(t^a)_{ij}(t^a)_{kl} = \frac{1}{2}(\delta_{il}\delta_{kj} - \frac{1}{N}\delta_{ij}\delta_{kl}), \tag{1.6}$$

which specifies color index i to j for particle 1 and color index k to l for particle 2, exchanging all 8 gluons. Here $i, j, k, l \in \{1, 2, 3\}$ for $N_c = 3$. For the quark-antiquark interaction, this tensor product becomes $(t^a)_{ij}(t^a)^*_{kl}$. With the help of $(t^a)^*_{kl} = (t^a)_{lk}$, the expression for $(t^a)_{ij}(t^a)^*_{kl}$ can be obtained by exchanging k and l in Eq. (1.6). For gluons, the representation $(t^a_G)_{eh}$ is real since $(t^a_G)^*_{eh} = -(t^a_G)_{eh}$. Thus, no complex conjugate is needed. For the coupling constant matrix, the gluon-quark interaction is proportional to $(t^a_G)_{cd}(t^a)_{lk}$, and the gluon-gluon interaction is proportional to $(t^a_G)_{cd}(t^a_G)_{eh}$, where $c, d, e, h \in \{1 \ldots 8\}$. For this case, there is no compact formula available to my knowledge. We need to look up the tables for f^{abc} and $(t^a)_{ij}$ in the literature and express every element of the tensor product by definition. However, these tensor products of two generators have a diagonal representation (with eigenvalues shown in Table. 1.1) which

simplifies the calculations in many cases. Since for any Lie Algebra $[t_r^a, t_r^b] = if^{abc}t^c$,

qq	$q\bar{q}$	$(q/\bar{q})g$	gg
(-2/3, 3)	(-4/3, 1)	(-3/2, 3)	(-3, 1)
(1/3, 6)	(1/6, 8)	(-1/2, 6)	(-3/2, 16)
		(1/2, 15)	(1, 27)

Table 1.1: Casimir factors C_a and degeneracy factors for different color channels organized as (Casimir factor, degeneracy) where q, $\bar{q}$, g are quark, antiquark, and gluon. Adapted from [8]

its unitary transformation $U^{-1}t_r^a U$ obeys the same Lie algebra but usually has a different matrix structure. Therefore, the matrix is not unique under the transformation. However, the eigenvalues of the matrix, as shown in Table 1.1, do not change under unitary transformation, which suggests that they contain non-trivial gauge-invariant information of the theory. Regarding the degeneracy, we usually call ($q\bar{q}$) with degeneracy 1 the color-singlet channel and with degeneracy 8 the color-octet channel. The same naming scheme applies to other channels.[1] The scattering amplitude in channel "a" ($q\bar{q}$ singlet, octet, etc.) is proportional to

$$C_a \alpha_s \frac{-1}{q_0^2 - \mathbf{q}^2}, \tag{1.7}$$

which is one use of Table. 1.1. In the singlet channel, it is proportional to $-\frac{4}{3}\alpha_s \frac{-1}{q_0^2 - \mathbf{q}^2}$. Here, $\alpha_s = \frac{g^2}{4\pi}$.

In QCD, each flavor of quarks has 3 colors and 2 spins. Combined with antiquarks, there are $N_f \times 2 \times 3 \times 2$ degrees of freedoms for quarks. The gluon has 8 colors and 2 polarizations, which in total yields 2×8 degrees of freedoms. The gauge invariance informa-

[1] gluon-gluon channel with degeneracy 16 is actually two octet channels with same Casimir factor; also two (10 degeneracy) representations have coupling 0 which are not listed [8].

tion for the interactions between any two color charges is better specified by the Casimir factors in specific channels listed in Table. 1.1, rather than by a full tensor product. A first-principles QCD calculation is usually very challenging in the low-momentum region due to strong coupling. Instead, we need to construct models to study the corresponding physics. However, these essential features of QCD are what we need to incorporate into our effective model for QCD.

1.2 Asymptotic Freedom and Confinement

The non-Abelian gauge theory has several features that are different from the Abelian gauge theory. The electric charge in Abelian gauge theory is always screened at large distance due to the polarization of the medium, so that the bare charge is surrounded by a cloud of charge with opposite sign (screening). On the other hand, at smaller distances, we observe more charge since we penetrate through the "screening cloud". More specifically, this picture is described by a renormalization group technique using the β function, which is **positive** for QED

$$\beta(g) = \frac{e^3}{12\pi^2}. \tag{1.8}$$

Using the renormalization group equation $dg/d\ln(q/u) = \beta(g)$ (u is the renormalization scale), we get the running coupling as

$$\alpha(q) = \frac{\alpha(\mu)}{1 - \frac{\alpha}{3\pi}\ln(q^2/u^2)}. \tag{1.9}$$

As momentum increases, which means probing shorter distance, the coupling constant will increase.

However, QCD is very different due to a **negative** beta function

$$\beta(g) = -\frac{g^3}{4\pi}[\frac{11}{3}C_2(G) - \frac{4}{3}N_f C(r)]. \tag{1.10}$$

Here, the Casimir factors $C(r) = \frac{1}{2}$, and $C_2(G) = 3$. The self-interaction of the force carrier (gluon) changes the sign of the beta function which leads to a strong running coupling constant α_s

$$\alpha_s(q) = \frac{\alpha_s(\mu)}{1 + \frac{a_s}{4\pi}(\frac{11}{3}N_c - \frac{2}{3}N_f)\ln(q^2/u^2)} = \frac{1}{\beta_0 \ln(q^2/\Lambda^2_{\rm QCD})}. \tag{1.11}$$

Here $\beta_0 = [(11/3)N - (2/3)N_f]/(4\pi)$ and $\Lambda_{\rm QCD} = ue^{-1/(2\alpha_s\beta_0)}$. The (strong) $\alpha_s(q)$ is asymptotically free for large momentum transfer, which means the coupling constant decreases as momentum increases (distance decreases). This is the opposite case of QED. On the other hand, at small momentum and large distance, α_s increases, which means the QCD vacuum is anti-screening. Indeed, for leading loop results, using $\alpha_s = 0.17$ at $u = 10\,\text{GeV}$ with $N_c = 3$ and N_f = 2, we can estimate $\Lambda_{\rm QCD} \approx 0.2\,\text{GeV}$. The classical QCD Lagrangian (massless case) is scale invariant, but the cut-off scale introduced here breaks this scale invariance at the quantum level. At the momentum $k = \Lambda_{\rm QCD}$, the coupling constant is infinite (one loop). This large coupling pushes the gauge theory into the strongly coupled region, where non-trivial vacuum effects become important. This introduces another important feature of QCD, confinement of color charge.

One way to picture the confinement[2] is using the Cornell potential in the color singlet channel for a heavy quark-antiquark pair [13, 14, 15, 11]

$$\tilde{V}(r) = -\frac{4}{3}\alpha_s\frac{1}{r} + \sigma r, \tag{1.12}$$

[2]Confinement is a general feature of gauge theory at strong coupling and is even true for abelian gauge, as discussed in Refs. [11, 12].

which is plotted in Figure 1.1. In addition to the color Coulomb term, there is a linearly increasing confining term, also referred to as the string term or linear term. The Cornell

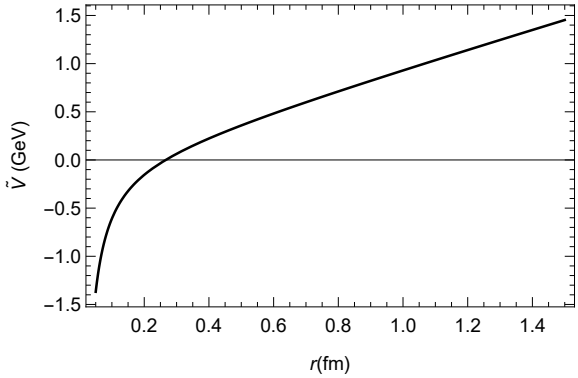

Figure 1.1: Cornell potential with $a_s = 0.27$ and $\sigma = 1\,\text{GeV/fm}$.

potential has been successfully used to calculate the charmonium spectrum [13], serving as one verification of the existence of confining potentials in nature. Similar approaches result in unexpected success for light hadron spectroscopy [16, 17]. Lattice QCD (lQCD) simulations realize Wilson's idea [11] and calculate this potential using the first principles path integral formalism in imaginary time. See Ref. [18] and references therein.

The name confinement implies that it takes infinite energy to separate two static charges to infinite distance in the pure gauge field case without dynamic quarks. In reality, since the energy at large distance is larger than a pair creation threshold, there will be light quark-antiquark pairs emerging from the vacuum to break the "string" and screen the color potential by forming two heavy-light mesons. The topological nontrivial configurations of the gauge field, such as color magnetic monopoles, are suspected to be responsible for this string term. In a dual-superconductor picture, this string term is formed by the dual Meissner effect. For the normal Meissner effect in superconductors with electric charge condensation, the magnetic fields get expelled. In the dual-superconductor picture, the

dual Meissner effect will expel the electric field lines into a flux tube which generates a linearly rising potential (for more details see Ref. [12] and references therein). At high temperature, the condensate of magnetic monopoles starts melting and the excited quarks and gluons will screen the string potential. Therefore, QCD matter at high temperature will enter a deconfined phase, which will be discussed in the next section.

1.3 Quark-Gluon Plasma Observed in Real-Time and Imaginary-Time

The quark-gluon plasma (QGP) is a deconfined phase of ordinary hadronic matter expected to exist at extremely high temperatures where the quarks and gluons are no longer localized/confined in hadrons and become the degrees of freedom that characterize the dynamics of the system. In the real world (real time), it is widely accepted that this high temperature phase exists in the first few microseconds of the Big Bang and in heavy-ion collisions (HICs) at RHIC and the LHC for sizes of the order of $(10\,\mathrm{fm})^3$ and lasting approximately several $10^{-23}\,\mathrm{s}$.[3] Also, with the development of modern computational technology, many properties of QGP can be studied with the lQCD formalism using first principles calculations in imaginary time. These are two important sources for us to study the properties of QGP and starting points to pursue the microscopic physics of the QGP.

In this paragraph, we discuss several important experimental observations for the QGP and their implications that are relevant to the main topic of this dissertation. First, the temperature of the medium can be measured using the dilepton spectra in the intermediate invariant mass region [20, 21]. The QGP created by HICs reaches the temperature around nine order of magnitude higher than the surface temperature of the sun. Second, the color deconfinement was indicated by measuring the suppression of the J/ψ (charm/anti-charm bound state) in the QGP [22, 23, 24]. The original idea [25] is that the screening of the confining force mentioned in Sec 1.2 can lead to deconfinement and dissociation, which

[3] There are QGP-like behaviors found in high-multiplicity events in small systems, see Ref. [19] and references therein.

manifests as J/Ψ suppression that can be observed in experiments. However, comprehensive studies using phenomenological models [26, 27, 28, 29, 30] suggest there are other processes besides screening effects—such as quasi-free [26] and gluon dissociation [31, 32, 33, 34] and their reverse regeneration process—that are important to understand observations in experiments [22, 23, 24]. (These processes are also important in the Bottomonium case [35, 36].) All these models require a deconfinement/screened color potential, so that experimental results still support a deconfinement phase—the QGP is created by HICs. Third, the QGP created in HICs is a liquid-like state, rather than the weakly coupled gas expected by theoretical models in the early days. This is evidenced by the successful description of the flows of light hadrons observed by experiments [37] with hydrodynamic models [38, 39]. Using a viscous hydrodynamics model [40, 41], the viscosity-to-entropy-ratio of QGP is found to be close to the quantum lower bound of $1/(4\pi)$ [42]. Thus, the QGP is believed to be the most perfect liquid ever observed. Lastly, there are heavy-light meson observables [43, 44, 45, 46] that are especially useful for determining the coupling strength of the medium [47]. This is because experimental observables are manifestations of the underlying Brownian motion of the heavy quark [48, 49, 50, 51, 47, 52], which is controlled by a set of transport coefficients that are sensitive to the coupling strength of heavy quarks to the QGP medium.

Besides the experiments, the thermodynamics and imaginary time current-correlator functions in QCD matter are widely studied in lQCD, which carry out the path integral in imaginary time from first principles. These lQCD studies provide valuable information concerning the properties of the QGP. The studies of Equation of State (EoS) and chiral susceptibilities by lQCD reveal that the transition of degrees of freedom (hadronic matter to QGP) is a rapid crossover [53] with a pseudo-critical temperature of approximately 0.155 GeV [54, 5]. Also, this EoS is used in hydrodynamic simulations, resulting in satisfactory phenomenological results. The interaction strength of the medium is also encoded

in lQCD data for the static quark free energy [55, 56], which quantifies the increase of the free energy by adding two static quarks at distance r. In vacuum, this free energy is just the potential between two color charges. In medium, it is closely related to the potential [57]. The screening or "string breaking" of the free energy around the temperature 0.17 GeV suggests the medium becomes deconfined. Moreover, the lQCD data for Euclidean correlator ratio [58, 59, 3] encode information for spectral functions of J/Ψ and other quarkonium states. This is closely related to the dissociation rates of the quarkonium states and provides extra constrains for the in-medium potential [60, 61]. Besides these lQCD results, there are many other lQCD observables, such as various susceptibilities [62] and spatial correlators [63] that provide more information about QGP physics. Presently, however, lQCD can only reliably calculate quantities in imaginary time. Analytic continuation to real time is usually rather challenging due to the loss of information in the imaginary time computation.

1.4 Motivation, Objective and Outline

As discussed in the previous section, many macroscopic properties of the QGP can be inferred from experiments and lQCD studies, raising questions concerning the microscopic physical mechanisms responsible for these unique features. However, the microscopic physics is not readily captured by the widely used perturbative or quasiparticle approaches;, see, *e.g.*, Refs. [64, 65] for reviews. On the other hand, the use of lQCD motivated potentials, specifically the heavy-quark (HQ) internal energy, has led to the idea of a bound-state QGP [8, 66] as a "transition" medium, with essential contributions from nonperturbative interactions, *i.e.*, remnants of the confining force. For heavy quarks these ideas have been implemented within a thermodynamic T-matrix approach [60, 67, 68, 69, 70], thereby connecting the open and hidden heavy flavor (HF) sectors. This framework has met fair success in understanding pertinent low-momentum

HF observables in ultra-relativistic heavy-ion collisions (URHICs), and has reinforced the need for a more rigorous determination of the underlying 2-body interaction, rather than bracketing it by the free and internal energies which roughly correspond to a weakly and strongly coupled scenario, respectively. In a lQCD-based extraction [71], it was found that the static potential is close to the free energy, while the associated imaginary part is near expectations from hard-thermal-loop perturbation theory. In Ref. [57] the HQ free energy was calculated within a T-matrix formalism, where the underlying potential was defined as the driving kernel in the corresponding integral equation. It was found that, in the presence of large imaginary parts of the static quarks, the lQCD data support a solution where the potential rises well above the free energy. Furthermore, implementing this potential in a selfconsistent quantum many-body framework (the Luttinger-Ward-Baym (LWB) formalism) [72, 73, 74], a description of the EoS of the QGP was achieved where parton spectral functions become very broad, losing their quasiparticle nature at low momenta, and the degrees of freedom change to broad hadronic states as the transition temperature is approached from above [75].

In this dissertation, we expand on our previous studies by setting up a unified T-matrix approach to investigate the microscopic properties of light, heavy and static degrees of freedom of the QGP, and firmly root it in information available from thermal lQCD as well as vacuum spectroscopy [16, 17, 76]. Our starting point is an effective Hamiltonian in quark and gluon degrees of freedom with a color interaction of Cornell-type including relativistic corrections. We determine this input by systematically constraining the interaction through the static HQ free energies, Euclidean correlators for charmonia and bottomonia, and the EoS in the light sector with 2 additional effective-mass parameters for light quarks and gluons. As mentioned above, a key feature of this approach is to retain the full off-shell properties of one- and two-body spectral functions (and scattering amplitudes), which renders the emerging micro-structure of the QGP a prediction of

the formalism. Since the latter is directly formulated in real time, transport coefficients (η/s or the HF diffusion coefficients, $\mathcal{D}_s$) and other quantities of experimental interest (*e.g.*, photon and dilepton production rates) can be readily computed. As it turns out, the self-consistent solution to the 3 sets of lQCD data is not unique. We will therefore discuss limiting cases of the underlying force strength and elaborate on the pertinent consequences for QGP structure. Lastly, we apply these solutions to calculate the transport coefficients. Inserting these into a HQ transport approach in HICs, the comparison of resulting heavy meson spectra with experimental results allows us to finally find the "correct" scenario.

The outline of the dissertation is as follows. In Chapter 2, we introduce the T-matrix approach and the basic microscopic setup of the model. In Chapter 3, we introduce the theoretical development of the T-matrix approach in order to compare to various lQCD results. In chapter 4, we compare the T-matrix approach to lQCD data and discuss the real-time microscopic physics extracted from this comparison. In Chapter 5, we apply our results to calculate HQ transport coefficients. Using simulations provided by our collaborator, Min He, we compare our results to experimental data. Chapter 6 contains our conclusions and outlook.

Most contents in Sec. 1.4, Chapter 2-4, Chapter 6, Appendix A are taken from the paper [1]. The results in Sec. 5.4 are partly taken from [77]. Professor Ralf Rapp is the coauthor of these two papers. The simulation results and part of the text in 5.3.3 is contributed by our collaborator Professor Min He.

2. REVIEW OF T-MATRIX FORMALISM*

Bound states are key entities of the nonperturbative physics of a quantum system, especially in QCD where the hadrons encode the phenomena of confinement and mass generation. In diagram language, bound states require an infinite resummation of (ladder) diagrams, represented by an integral equation such as the 4D Bethe-Salpeter (BS) equation (BSE) [78] or a 3D reduced T-matrix equation [79, 80, 81]. Both equations allow for a simultaneous and straightforward treatment of scattering states. As a resummed series, the solution of the integral equation analytically continues to the strongly coupled region.[1] This equation is therefore well suited to study the strongly coupled QGP (sQGP) near T_c where both bound and scattering states are expected to be important and entangled with each other in the presence of strong quantum effects, *i.e.*, large scattering rates. Applications of the T-matrix approach in media has been carried out in various contexts, mostly in non-relativistic many-body systems [84, 85, 86] but also in systems where relativistic effects are relevant [87], *e.g.*, the nuclear many-body problem [88, 89], hot hadronic matter [90] or the QGP [66, 77, 91, 92].

In this chapter, the 4D full relativistic BSE and its reduction to a 3D relativistic T-matrix equation are briefly introduced in Sec. 2.1. In Sec 2.2, we discuss the thermodynamic T-matrix approach used in the rest of this paper. The (center of mass) CM transform used by the approach is elaborated in Sec. 2.3.

*Part of this chapter is reprinted with permission from "T-matrix approach to quark-gluon plasma" by Shuai Y. F. Liu and Ralf Rapp, 2018, Phys. Rev. C **97**, 034918, Copyright 2018 by APS.

[1]The series $1+\alpha+\alpha^2\cdots=1/(1-\alpha)$ is convergent for strong coupling. Divergence at strong coupling is different from the $N!$ divergence of a perturbative series at small coupling [82, 83].

2.1 Bethe-Salpeter Equation and Its 3D Reduction

The BSE is a relativistic two-body integral equation that can be obtained by resumming two-body ladder-like diagrams [78]. It can also be obtained from the infinite tower of the coupled Schwinger-Dyson equations with proper truncation scheme. With the kernel $K(p_1 - p_1')$, the BSE in momentum space is expressed as

$$T(p_1, p_2, p_1', p_2') = K(p_1 - p_1') + \int \frac{d^4k_1}{(2\pi)^4} K(p_1 - k_1) G(k_1) G(p_1 + p_2 - k_1) T(k_1, p_1 + p_2 - k_1, p_1', p_2'), \tag{2.1}$$

where the p and k are 4D energy-momenta. Note that $p_1 + p_2$ is an external (conserved) quantity and is not being integrated over. This may, alternatively, be expressed in terms of explicit 3 momentum and energy,

$$T(E, \omega_1, \omega_1', \mathbf{P}, \mathbf{p}_1, \mathbf{p}_1') = K(\omega_1 - \omega_1', \mathbf{p}_1 - \mathbf{p}_1') + \int \frac{d\nu d^3\mathbf{k}}{(2\pi)^4} K(\omega_1 - \nu, \mathbf{p}_1 - \mathbf{k}) G(\nu, \mathbf{k}) G(E - \nu, \mathbf{P} - \mathbf{k}) T(E, \nu, \omega_1', \mathbf{P}, \mathbf{k}, \mathbf{p}_1'). \tag{2.2}$$

From here on, the 3D notation is used with the replacements: $p_1 \to (\omega_1, \mathbf{p}_1)$, $k_1 \to (\nu, \mathbf{k})$; and $p_1 + p_2 \to (E, \mathbf{P})$, where $E = \omega_1 + \omega_2$ and $\mathbf{P} = \mathbf{p}_1 + \mathbf{p}_2$.

The solution to the 4D BSE is usually difficult, especially in real-time Minkowski space. A straightforward treatment predicts abnormal solutions due to extra relative energy besides the total energy [93]. Also, the poles in the exchange propagator complicate the numerical approach to find a solution in Minkowski space (real time). A more feasible approach to solving the 4D relativistic equation is to use a 3D reduction [79, 80], in which the full 4D effects can be corrected order by order. This 3D relativistic equation is widely used to study nucleon scattering and the associated many-body physics [94, 88]

and hadronic many-body system [95, 96].

The method of 3D reduction is illustrated by expressing the BSE in formal notation,

$$T = K + KGGT. \tag{2.3}$$

This equation can be re-expressed as two coupled integral equations [79],

$$T = W + W\mathcal{E}_{(2)}T \tag{2.4}$$

$$W = K + K[GG - \mathcal{E}_{(2)}]T. \tag{2.5}$$

The key to simplifying the problem is from the freedom to choose a singular two-body propagator $\mathcal{E}_{(2)}$, which can include a delta function for the energy transfer as an example. This results in a trivial integration over energy in Eq. (2.4), thereby completing the 3D reduction. The resulting 3D equation can be solved non-perturbatively and without the difficulties of the 4D problem mentioned before. The full 4D features of the equation can be corrected perturbatively to the kernel W order by order through Eq. (2.5). For most purposes, it is enough to keep only the first-order correction in Eq. (2.5). Different choice for $\mathcal{E}_{(2)}$ result in different reduction schemes, as is illustrated in detail in Ref. [81] and references therein. In the present work, we choose the Thompson scheme [80] as the starting point for our many-body physics. In the remainder of this section, we propose a general scheme that is suitable for the off-shell case which can also extend to the imaginary time BSE at finite temperature with Matsubara frequencies. This may be useful in the future for systematically including dynamical screening effects. It also provides an example for a 3D reduction calculation.

In this scheme, we choose the singular propagator

$$\mathcal{E}_{(2)}(E,\nu,\mathbf{P},\mathbf{k}) = 2\pi[\delta(f)/f']G_{(2)}(E,\mathbf{P},\mathbf{k}), \tag{2.6}$$

where δ is the Dirac-delta function and f is a abbreviation of the function $f(\nu,\mathbf{k},\omega_1,\mathbf{p}_1,\omega_1',\mathbf{p}_1',$ $E,\mathbf{P})$ in general. Different choices for f can lead to different reduction schemes. The $\delta(f)$ results in a trivial integration over energy in Eq. (2.4). The $G_{(2)}(E,\mathbf{P},\mathbf{k})$ is

$$G_{(2)}(E,\mathbf{P},\mathbf{k}) = \int \frac{d\nu}{2\pi} G(\nu,\mathbf{k})G(E-\nu,\nu,\mathbf{P}-\mathbf{k}) = \int \frac{d\nu}{2\pi}\mathcal{E}_{(2)}(E,\nu,\mathbf{P},\mathbf{k}). \tag{2.7}$$

Substituting $\mathcal{E}_{(2)}(E,\nu,\mathbf{P},\mathbf{k})$ into Eq. (2.4) results in

$$\begin{aligned} &T(E,\omega_1,\omega_1',\mathbf{P},\mathbf{p}_1,\mathbf{p}_1') = W(E,\omega_1,\omega_1',\mathbf{P},\mathbf{p}_1,\mathbf{p}_1')+ \\ &\int \frac{d\nu d^3\mathbf{k}}{(2\pi)^4} W(E,\omega_1,\nu,\mathbf{P},\mathbf{p}_1,\mathbf{k})2\pi[\delta(f)/f']G_{(2)}(E,\mathbf{P},\mathbf{k})T(E,\nu,\omega_1',\mathbf{P},\mathbf{k},\mathbf{p}_1'). \end{aligned} \tag{2.8}$$

For an arbitrary f, the result after integration over the δ-function is

$$\begin{aligned} &T(E,\omega_1,\omega_1',\mathbf{P},\mathbf{p}_1,\mathbf{p}_1') = W(E,\omega_1,\omega_1',\mathbf{P},\mathbf{p}_1,\mathbf{p}_1')+ \\ &\int \frac{d^3\mathbf{k}}{(2\pi)^3} W(E,\omega_1,\nu(f),\mathbf{P},\mathbf{p}_1,\mathbf{k})G_{(2)}(E,\mathbf{P},\mathbf{k})T(E,\nu(f),\omega_1',\mathbf{P},\mathbf{k},\mathbf{p}_1') \end{aligned} \tag{2.9}$$

Note that this is a 3D (rather than 4D) integral equation—containing only 3 momenta. $\nu(f)$ is the solution of ν for the equation $f(\nu,\mathbf{k},\omega_1,\mathbf{p}_1,\omega_1',\mathbf{p}_1',E,\mathbf{P}) = 0$. If we choose $f = \omega_1 - \nu$, $W(E,\omega_1,\omega_1',\mathbf{P},\mathbf{p}_1,\mathbf{p}_1') = W(\omega_1-\omega_1',\mathbf{p}_1-\mathbf{p}_1)$ and define $V(\mathbf{p}_1-\mathbf{p}_1') =$

$W(0, \mathbf{p}_1 - \mathbf{p}_1')$, we can get the equation

$$T(E, \omega_1, \omega_1', \mathbf{P}, \mathbf{p}_1, \mathbf{p}_1') = W(\omega_1 - \omega_1', \mathbf{p}_1 - \mathbf{p}_1') + \int \frac{d^3\mathbf{k}}{(2\pi)^3} V(\mathbf{p}_1 - \mathbf{k}) G_{(2)}(E, \mathbf{P}, \mathbf{k}) T(E, \omega_1, \omega_1', \mathbf{P}, \mathbf{k}, \mathbf{p}_1'). \quad (2.10)$$

The integral equation can be understood as a matrix equation after discretization of its momentum variables $\mathbf{p}_1$, $\mathbf{p}_1'$ and $\mathbf{k}$. Suppressing the explicit dependence on conserved variables E, $\mathbf{P}$ and the matrix indices $\mathbf{p}_1$, $\mathbf{p}_1'$ and $\mathbf{k}$, the solution can be expressed as

$$T(\omega_1, \omega_1') = [1 - VG_{(2)}]^{-1} W(\omega_1 - \omega_1'). \quad (2.11)$$

In CM frame for the on-shell case, we have $\omega_1 = \omega_1' = \varepsilon(p_{\text{cm}})$ so that $W(\omega_1 - \omega_1') = V$. Therefore, the solution reduces to the usual T-matrix solution:

$$T = [1 - VG_{(2)}]^{-1} V. \quad (2.12)$$

For the general case, the solution can be formally expressed as

$$T(\omega_1, \omega_1') = W(\omega_1, \omega_1') + W(\omega_1, \nu(f)) V^{-1} \{[1 - VG_{(2)}]^{-1} - 1\} W(\nu(f)', \omega'). \quad (2.13)$$

Here, $W = W(E, \omega_1, \omega_1', \mathbf{P}, \mathbf{p}_1, \mathbf{p}_1')$ and $V = W(E, \nu(f), \nu(f)', \mathbf{P}, \mathbf{k}, \mathbf{k}')$, where $\nu(f)'$ is the solution of ν for the equation $f(\nu, \mathbf{k}', \omega_1, \mathbf{p}_1, \omega_1', \mathbf{p}_1', E, \mathbf{P}) = 0$. Similarly, the abbreviation $W(\omega, \nu(f))$ and $W(\nu(f)', \omega')$ denotes $W(E, \omega_1, \nu(f), \mathbf{P}, \mathbf{p}_1, \mathbf{k})$ and $W(E, \nu(f)', \omega_1', \mathbf{P}, \mathbf{k}', \mathbf{p}_1')$ respectively. Note that the matrix operation over the kernel $VG_{(2)}$ in Eq. (2.13) is 3D, and the matrix operations only act on the indices $\mathbf{k}$ and $\mathbf{k}'$. Thus, the numerical difficulties are significantly less than those in the pure 4D equation. However, the solution can regain relativistic effects through corrections to W and V using Eq. (2.5) (usually

perturbatively). Indeed, with a proper choice of f, the equation to leading order in W and V (usually a potential kernel) already includes several important relativistic effects. Thus, this coupled equation is an example of how to expand a full relativistic solution around its potential solution. The equation after this reduction procedure is usually called 3D relativistic equation that can help us to study the properties of light partons in the QGP. A further discussion for this point can be found in App. A.

2.2 Thermodynamic T-Matrix Approach

In the present work our starting point is a Hamiltonian with relativistic dispersion relations and potential, which maps onto the Thompson scheme [80] for the 3D reduction from the BSE to the T-matrix equation (as employed earlier in the HQ sector [68]). It can be written in the form

$$H = \sum \varepsilon_i(\mathbf{p})\psi_i^\dagger(\mathbf{p})\psi_i(\mathbf{p}) + \frac{1}{2}\psi_i^\dagger(\frac{\mathbf{P}}{2}-\mathbf{p})\psi_j^\dagger(\frac{\mathbf{P}}{2}+\mathbf{p})V_{ij}^a\psi_j(\frac{\mathbf{P}}{2}+\mathbf{p}')\psi_i(\frac{\mathbf{P}}{2}-\mathbf{p}') \quad (2.14)$$

where ψ_i is the field operator of parton i and $\varepsilon_i(\mathbf{p}) = \sqrt{M_i^2+\mathbf{p}^2}$ and $\mathbf{P}$ is the total momentum of the 2-particle state. The summations over i, j include momentum, spin, color, and particle species (3 quark flavors and gluons for the bulk matter description, or charm, bottom, static flavors for pertinent correlation functions). The index "a" specifies the two-body color channels. In this work, we do not account for spin-dependent interactions, which are expected to be subleading but can be included in the future. For the potential, V, we include both color-Coulomb ($V_{\mathcal{C}}$) and (remnants of the) confining ("string") interactions ($V_{\mathcal{S}}$),

$$V_{ij}^a(\mathbf{p},\mathbf{p}') = \mathcal{R}_{ij}^{\mathcal{C}}\mathcal{F}_a^{\mathcal{C}}V_{\mathcal{C}}(\mathbf{p}-\mathbf{p}') + \mathcal{R}_{ij}^{\mathcal{S}}\mathcal{F}_a^{\mathcal{S}}V_{\mathcal{S}}(\mathbf{p}-\mathbf{p}'). \quad (2.15)$$

Relativistic effects in the vertices of the 4D theory are included by introducing relativistic factors $\mathcal{R}$ [97, 68]

$$\mathcal{R}^{\mathcal{C}}_{ij} = \sqrt{1 + \frac{p^2}{\varepsilon_i(p)\varepsilon_j(p)}}\sqrt{1 + \frac{p'^2}{\varepsilon_i(p')\varepsilon_j(p')}} \tag{2.16}$$

$$\mathcal{R}^{\mathcal{S}}_{ij} = \sqrt{\frac{M_i M_j}{\varepsilon_i(p)\varepsilon_j(p)}}\sqrt{\frac{M_i M_j}{\varepsilon_i(p')\varepsilon_j(p')}}\,, \tag{2.17}$$

and $\mathcal{F}^{\mathcal{C},\mathcal{S}}$ are color factors in diagonal representation; specifically, the Coulomb factors, $\mathcal{F}^{\mathcal{C}}$, are the standard Casimir coefficients [8, 68] collected in Table 2.1, while for the string factors, $\mathcal{F}^{\mathcal{S}}$, we take the absolute values of the Casimir coefficients, to ensure a positive definite string tension, which appears to be weaker in colored channels [55]. The precise form of $V_{\mathcal{C}}$, $V_{\mathcal{S}}$ and the parton mass values, M_i, are inputs to the Hamiltonian that need to be constrained by the lQCD data to be discussed in the following sections.

qq	$q\bar{q}$	$(q/\bar{q})g$	gg
(1/2, 3)	(1, 1)	(9/8, 3)	(9/4, 1)
(-1/4, 6)	(-1/8, 8)	(3/8, 6)	(9/8, 16)
		(-3/8, 15)	(-3/4, 27)

Table 2.1: Casimir and degeneracy factors for different color channels quoted as (Casimir factor, degeneracy).

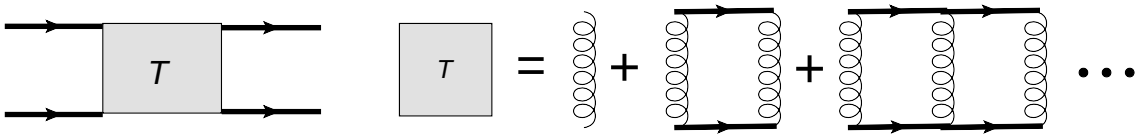

Figure 2.1: T-matrix resummation for ladder diagrams

The finite-temperature calculations are carried out in the Matsubara formalism where the “bare" propagators for both quarks and gluons are taken as

$$G_i^0(i\omega_n, \mathbf{p}) = \frac{1}{i\omega_n - \varepsilon_i(\mathbf{p})} \, . \tag{2.18}$$

We resum the ladder diagrams of the Hamiltonian by the T-matrix equation, pictorially displayed in Fig. 2.1. In the CM frame it can be written as

$$T_{ij}^a(z, \mathbf{p}, \mathbf{p}') = V_{ij}^a(\mathbf{p}, \mathbf{p}') + \int_{-\infty}^{\infty} \frac{d^3\mathbf{k}}{(2\pi)^3} V_{ij}^a(\mathbf{p}, \mathbf{k}) G_{ij}^0(z, \mathbf{k}) T_{ij}^a(z, \mathbf{k}, \mathbf{p}') \tag{2.19}$$

where $z = iE_n$ is the two-body Matsubara frequency (or analytical energy variable $E \pm i\epsilon$), and $\mathbf{p}, \mathbf{p}'$ are the incoming and outgoing 3-momenta, respectively, for each parton in the CM frame, *i.e.*, for total momentum $\mathbf{P} = \vec{0}$; $T_{ij}^a(z, \mathbf{p}, \mathbf{p}')$ denotes the T-matrix between particle type i and j in color channel a. The two-body propagator is defined in Matsubara representation as

$$G_{ij}^0(iE_n, \mathbf{k}) = -\beta^{-1} \sum_{\omega_n} G_i(iE_n - i\omega_n, \mathbf{k}) G_j(i\omega_n, \mathbf{k}) \, , \tag{2.20}$$

and, using a spectral representation, can be written in terms of single-particle spectral functions as

$$G_{ij}^0(z, \mathbf{k}) = \int_{-\infty}^{\infty} d\omega_1 d\omega_2 \frac{(1 \pm n_i(\omega_1) \pm n_j(\omega_2))}{z - \omega_1 - \omega_2} \rho_i(\omega_1, \mathbf{k}) \rho_j(\omega_2, \mathbf{k}) \tag{2.21}$$

with the single-particle propagators

$$G_i(z) = \frac{1}{[G_i^0(z,k)]^{-1} - \Sigma_i(z,k)} = \frac{1}{z - \varepsilon_i(p) - \Sigma_i(z,k)}, \tag{2.22}$$

and pertinent spectral functions,

$$\rho_i(\omega,\mathbf{k}) = -\frac{1}{\pi}\mathrm{Im}G_i(\omega + i\epsilon)\ . \tag{2.23}$$

In Eq. (2.21) the $\pm$ sign refers to bosons (upper) and fermions (lower), and n_i is the Bose or Fermi distribution function for parton i. The in-medium selfenergies, $\Sigma_i(z,k)$, will be self-consistently computed through the 2-body T-matrix, as detailed below.

In vacuum it is sufficient to solve the T-matrix in the CM frame due to Lorentz invariance. However, in medium, Lorentz invariance is in general broken, although usually not by much for the scattering amplitude at total momenta comparable to the thermal scale in non-degenerate media. Thus, a standard approximation is to assume the in-medium T-matrix to be independent of $\mathbf{P}$ [68, 69], which leads to a major simplification of the calculations. We thus write

$$T^a_{ij}(\omega_1+\omega_2,\mathbf{p}_1,\mathbf{p}_2|\ \mathbf{p}'_1,\mathbf{p}'_2) = T^a_{ij}(E_{\rm cm},p_{\rm cm},p'_{\rm cm},x_{\rm cm}), \tag{2.24}$$

where $E_{\rm cm}$, $p_{\rm cm}$, $p'_{\rm cm}$ and $x_{\rm cm}\equiv\cos(\theta_{\rm cm})$ are functions expressed via $\omega_1+\omega_2,\mathbf{p}_1,\mathbf{p}_2,\ \mathbf{p}'_1,\mathbf{p}'_2$ using momentum conservation $\mathbf{p}_1+\mathbf{p}_2=\ \mathbf{p}'_1+\mathbf{p}'_2$ to define the transformation to the CM frame [2]:

$$\begin{aligned}
E_{\rm cm} &= \sqrt{(\omega_1+\omega_2)^2-(\mathbf{p}_1{+}\mathbf{p}_2)^2}\\
s_{\rm on} &= (\varepsilon_1(\mathbf{p}_1)+\varepsilon_2(\mathbf{p}_2))^2-(\mathbf{p}_1{+}\mathbf{p}_2)^2\\
p_{\rm cm} &= \sqrt{\frac{(s_{\rm on}-M_i^2-M_j^2)^2-4M_i^2M_j^2}{4s_{\rm on}}}\\
\cos(\theta_{\rm cm}) &= \frac{\mathbf{p}_{\rm cm}\cdot\mathbf{p}'_{\rm cm}}{p_{\rm cm}p'_{\rm cm}}.
\end{aligned} \tag{2.25}$$

[2] $\mathbf{P}/2\pm\mathbf{p}$ and $\mathbf{P}/2\pm\mathbf{p}'$ in Eq.(2.14) are shorthand notations that should be understood in this context.

For $p'_{\rm cm}$, we simply change $s_{\rm on}(\mathbf{p}_1, \mathbf{p}_2)$ to $s_{\rm on}(\mathbf{p}'_1, \mathbf{p}'_2)$. The reason for using the on-shell s for $p_{\rm cm}$ is to keep the analytical properties of the T-matrix after the transformation. Also, this transformation recovers Galilean invariance in the non-relativistic limit for the off-shell case. The relation for $p_{\rm cm}$ can be derived by solving the equations originating from Lorentz invariants $\varepsilon_1(\mathbf{p}_1)^2 - p_1^2 = M_1^2$, $\varepsilon_2(\mathbf{p}_2)^2 - p_2^2 = M_1^2$ and $(\varepsilon_1(\mathbf{p}_1) + \varepsilon_2(\mathbf{p}_2))^2 - (\mathbf{p}_1{+}\mathbf{p}_2)^2 = (\varepsilon_1(\mathbf{p}_{\rm cm}) + \varepsilon_2(\mathbf{p}_{\rm cm}))^2$ in the CM and the moving frame. We note that this procedure does not work for the CM angle in the off-shell case. The general transformations involving the CM angle are discussed in Sec. 2.3.

Rotational symmetry in the CM frame implies that a partial-wave expansion remains intact, given by

$$X(\mathbf{p}, \mathbf{p}') = 4\pi \sum_l (2l+1) X^l(p, p') P_l(\cos(\theta)), \tag{2.26}$$

where $X = V, T$. The partial-wave expanded scattering equation becomes

$$T_{ij}^{l,a}(z, p, p') = V_{ij}^{l,a}(p, p') + \frac{2}{\pi} \int_{-\infty}^{\infty} k^2 dk V_{ij}^{l,a}(p, k) G_{ij}^0(z, k) T_{ij}^{l,a}(z, k, p') \ , \tag{2.27}$$

where l denotes the angular-momentum quantum number. The set of now 1D integral equations can be solved by discretizing the 3-momenta p, p', k,

$$\mathbb{V}_{mn} \equiv V(k_m, k_n), \quad \hat{\mathbb{G}}^0_{(2)}(z)_{mn} \equiv \frac{2\Delta k}{\pi} k_m^2 G^0_{(2)}(z, k_m) \delta_{mn}, \tag{2.28}$$

and invert the pertinent matrix equation [98],

$$\mathbb{T}(z)_{mn} = T(z, k_m, k_n), \quad \mathbb{T}(z) = [\mathbb{1} - \mathbb{V}\hat{\mathbb{G}}^0_{(2)}(z)]^{-1}\mathbb{V} \ . \tag{2.29}$$

The integral over k in Eq. (2.27) is encoded in a matrix multiplication with measure dk. Here and in the following, we (occasionally) use the subscript "(2)" as an abbreviation for

"ij" to denote two-body quantities.

Once the T-matrices have been computed, we calculate the single-particle selfenergies by summing over all partial waves and the pertinent two-body flavor and color channels in interactions of two light medium partons. Closing the T-matrix with an in-medium single-parton propagator ("$\pm$" for boson/fermion) in the Matsubara formalism,

$$\Sigma(iw_n) = \pm\frac{-1}{\beta}\sum_{\nu_n} T(i\omega_n + i\nu_n)G(i\nu_n), \tag{2.30}$$

one can use spectral representations to carry out the summation over discrete frequencies to obtain

$$\begin{aligned}\Sigma_i(z,\mathbf{p}_1) = \int \frac{d^3\mathbf{p}_2}{(2\pi)^3}\int_{-\infty}^{\infty} d\omega_2 \frac{dE}{\pi}\frac{-1}{z+\omega_2-E}\frac{1}{d_i}\sum_{a,j} d_s^{ij} d_a^{ij} \\ \times \mathrm{Im}T_{ij}^a(E,\mathbf{p}_1,\mathbf{p}_2|\mathbf{p}_1,\mathbf{p}_2)\rho_j(\omega_2,\mathbf{p}_2)[n_j(\omega_2)\mp n_{ij}(E)]\end{aligned} \tag{2.31}$$

which involves the forward-scattering amplitude, *i.e.*, $\mathbf{p}_1' = \mathbf{p}_1$ and $\mathbf{p}_2' = \mathbf{p}_2$ and thus $x_{\rm cm} = x = 1$; n_{ij} refers to the Bose or Fermi distribution appropriate for the two-body state ij, and the "$-/+$" sign refers to the bosonic/fermionic single-parton state i. The $d_{a,s}^{ij}$ are color and spin degeneracy factors of the two-body system, summarized in Table 2.1. Here, we enforce two physical polarizations for the gluons; d_i is the spin-color degeneracy of the single parton i. The z is taken to be retarded, $\omega + i\epsilon$, in this work. Within the CM transformation defined via Eqs. (2.25), the integrations in Eq. (2.31) are restricted to the timelike 2-body phase, *i.e.*, real values for $E_{\rm cm}$ (we have verified that $\mathrm{Im}T_{ij}^a(\sqrt{E^2-P^2})$ is strongly suppressed when approaching the spacelike region).[3] The above selfenergy expression does not include the purely real thermal Fock term [99] which we add explicitly

[3]For $x < 0$ the $n(x)$ is regulated as $n(x) \equiv \mathrm{sign}(x)n(|x|)$ as in Refs. [95, 96]. Also, imaginary part of bosonic T-matrix is enforced to be odd in E. The contributions from $\omega_2 < 0$ or $E < 0$ are small.

by calculating

$$\Sigma_i(\mathbf{p}_1) = \mp \int \frac{d^3\mathbf{p}_2}{(2\pi)^3} \int_{-\infty}^{\infty} d\omega_2 V_{i\bar{i}}^1(\mathbf{p}_1 - \mathbf{p}_2)\rho_i(\omega_2, \mathbf{p}_2)n_i(\omega_2) \ . \tag{2.32}$$

Finally, we recall that Eq. (2.31) can be expressed as a functional equation of Σ,

$$\Sigma = T(\Sigma)G(\Sigma) = T(\Sigma)\frac{1}{(G^0)^{-1} - \Sigma} \ . \tag{2.33}$$

It is equivalent to an integral equation for the full Green function, G, as $\Sigma = (G^0)^{-1} - G^{-1}$. The T-matrix depends on the selfenergy, $T(\Sigma)$, through the two-body propagator, see Eq. (2.21), in which the spectral function depends on the single-parton selfenergy, see Eq. (2.23). Although it is a non-linear functional equation, it usually can be solved self-consistently by numerical iteration. The selfenergy as the solution of Eq. (2.33) satisfies conservation laws for the Green function [73].

2.3 Center of Mass Transformation

In this section, we detail the CM transformation implemented in this work. Firstly, we discuss the CM transformation in a nonrelativistic system. Then we discuss the relativistic version. The nonrelativistic T-matrix can be expressed as

$$\begin{aligned} &T(E, \mathbf{P}, \mathbf{p}_1, \mathbf{p}_1') = V(\mathbf{p}_1 - \mathbf{p}_1') + \\ &\int_{-\infty}^{\infty} \frac{d^3\mathbf{k}_1}{(2\pi)^3} V(\mathbf{p}_1 - \mathbf{k}_1) G_{(0)}^{(2)}(E, \mathbf{k}_1, \mathbf{P} - \mathbf{k}_1) T(E, \mathbf{P}, \mathbf{k}_1, \mathbf{p}_1'). \end{aligned} \tag{2.34}$$

Here $\mathbf{P} = \mathbf{p}_1 + \mathbf{p}_2$, $E = \omega_1 + \omega_2 + i\epsilon$. In a non-relativistic system, the two-body propagator is

$$G^{(2)}_{(0)}(E, \mathbf{k}) = \frac{1}{E - \frac{\mathbf{k}_1^2}{2M_1} - \frac{(\mathbf{P}-\mathbf{k}_1)^2}{2M_2}}. \tag{2.35}$$

The CM transformation can be expressed as

$$\mathbf{v}_{\text{cm}} = \frac{\mathbf{P}}{M_1 + M_2}, \mathbf{px}_{\text{cm}} = \mathbf{px}_1 - M_1\mathbf{v}_{\text{cm}}, \tag{2.36}$$

where the **px** represent $\mathbf{p}_i$, $\mathbf{p}'_i$, etc. Therefore, the transformations for the momenta are $\mathbf{p}_1 = \mathbf{p}_{\text{cm}} + M_1\mathbf{v}_{\text{cm}}, \mathbf{p}'_1 = \mathbf{p}'_{\text{cm}} + M_1\mathbf{v}_{\text{cm}}, \mathbf{k}_1 = \mathbf{k}_{\text{cm}} + M_1\mathbf{v}_{\text{cm}}$. Substituting these into Eq. (2.34) and noting that $V(\mathbf{p}_1 - \mathbf{p}'_1) = V(\mathbf{p}_{\text{cm}} - \mathbf{p}'_{\text{cm}})$, we construct an equivalent equation that only depends on E and $\mathbf{P}$ implicitly through $E_{\text{cm}} = E - \mathbf{P}^2/(2M_t)$,

$$\begin{aligned} T(E_{\text{cm}}, \mathbf{p}_{\text{cm}}, \mathbf{p}'_{\text{cm}}) = V(\mathbf{p}_{\text{cm}} - \mathbf{p}'_{\text{cm}}) + \int_{-\infty}^{\infty} \frac{d^3\mathbf{k}_{\text{cm}}}{(2\pi)^3} \\ V(\mathbf{p}_{\text{cm}} - \mathbf{k}_{\text{cm}}) \frac{1}{E_{\text{cm}} - \frac{(\mathbf{k}_{\text{cm}})^2}{2u}} T(E_{\text{cm}}, \mathbf{k}_{\text{cm}}, \mathbf{p}'_{\text{cm}}), \end{aligned} \tag{2.37}$$

where the total mass is $M_t = M_1 + M_2$, and the reduced mass is $u = M_1M_2/(M_1 + M_2)$. The solution to the original equation, Eq. (2.34), is calculated using the reverse CM transformation,

$$\begin{aligned} \mathbf{p}_{\text{cm}} &= \mathbf{p}_1 - \frac{M_1\mathbf{P}}{M_1 + M_2} = \frac{\mathbf{p}_1 M_2 - \mathbf{p}_1 M_1}{M_1 + M_2} \\ \mathbf{p}'_{\text{cm}} &= \mathbf{p}'_1 - \frac{M_1\mathbf{P}}{M_1 + M_2} = \frac{\mathbf{p}'_1 M_2 - \mathbf{p}'_1 M_1}{M_1 + M_2}. \end{aligned} \tag{2.38}$$

In vacuum, solving the equation in the CM frame and then transforming back to the arbitrary frame (as described above) results in the same solution as that obtained from solving

the original equation—due to Galilean invariance. No approximations are necessary when using this transformation method of solution. In medium, neglecting the blocking factor and using the two-body selfenergy to include medium effects, the T-matrix equation is

$$T(E_{\rm cm}, \mathbf{p}_{\rm cm}, \mathbf{p}'_{\rm cm}) = V(\mathbf{p}_{\rm cm} - \mathbf{p}'_{\rm cm}) + \int_{-\infty}^{\infty} \frac{d^3\mathbf{k}_{\rm cm}}{(2\pi)^3} V(\mathbf{p}_{\rm cm} - \mathbf{k}_{\rm cm}) \\ \frac{1}{E_{\rm cm} - \frac{(\mathbf{k}_{\rm cm})^2}{2u} - \Sigma_{(2)}(E, \mathbf{P}, \mathbf{p}_{\rm cm})} T(E_{\rm cm}, \mathbf{k}_{\rm cm}, \mathbf{p}'_{\rm cm}). \tag{2.39}$$

The CM approximation assumes that the two-body selfenergy only depends on $\mathbf{P}$ and E through $E_{\rm cm}$, so that $\Sigma_{(2)}(E, \mathbf{P}, \mathbf{p}_{\rm cm}) \approx \Sigma_{(2)}(E_{\rm cm}, 0, \mathbf{p}_{\rm cm}) \equiv \Sigma_{(2)}(E_{\rm cm}, \mathbf{p}_{\rm cm})$. However, in both vacuum and medium, the CM transformations have the same form, although it is an approximation for the in-medium case. Thus, the CM transformation can be understood as expressing $\mathbf{p}_{\rm cm}$ as a function of $\{M_1, M_2, \mathbf{p}_1, \mathbf{p}_2\}$ (and $\mathbf{p}'_{\rm cm}$ as a function of $\{M'_1, M'_2, \mathbf{p}'_1, \mathbf{p}'_2\}$). This motivates us to define the relativistic transformation for the in medium off-shell case.

In the relativistic formalism, transformations to an arbitrary frame are achieved using Lorentz transformations (parallel $\|$ and perpendicular $\perp$ to velocity)

$$E'_{\rm px} = \gamma(E_{\rm px} - {\rm v}\,{\rm px}_{\|}), {\rm px}'_{\|} = \gamma({\rm p}_{\|} - {\rm v}E_{\rm px}), \mathbf{px}'_{\perp} = \mathbf{px}_{\perp} \\ {\rm px}_{\|} = \mathbf{px} \cdot \hat{\mathbf{v}}, \mathbf{px}_{\perp} = \mathbf{px} - {\rm px}_{\|}\hat{\mathbf{v}}, \tag{2.40}$$

where the "hat" denotes a unit vector in this context. Relativistic CM transformations, analogous to Eq. (2.38), are realized using the quantities

$$\mathbf{v}_{\rm cm} = \frac{\mathbf{p}_1 + \mathbf{p}_2}{E_{\rm p_1} + E_{\rm p_2}}, \gamma_{\rm v_{cm}} = \frac{E_{\rm p_1} + E_{\rm p_2}}{\sqrt{s}} \\ s = (E_{\rm p_1} + E_{\rm p_2})^2 - (\mathbf{p}_1 + \mathbf{p}_2)^2. \tag{2.41}$$

After obtaining the solution in the CM frame, it is necessary to express $\{E_{\rm cm}, \mathbf{p}_{\rm cm}, \mathbf{p}'_{\rm cm}\}$ in terms of $\{\mathbf{p}_1, \mathbf{p}_2, \mathbf{p}'_1, \mathbf{p}'_2, E\}$ to obtain the solution in the arbitrary frame. The relativistic CM transformation for energy is simply $\sqrt{s} \equiv E_{\rm cm} = \sqrt{E^2 - P^2}$. It is more complicated for $\mathbf{p}_{\rm cm}$ and is expressed in terms of components parallel $\parallel$ and perpendicular $\perp$ to the CM velocity $\mathbf{v}_{\rm cm}$,

$$\begin{aligned} \mathrm{p}_{\parallel \rm cm} &= \gamma_{\mathrm{v}_{\rm cm}}(\mathrm{p}_{\parallel} - \mathrm{v}_{\rm cm} E_p) = \frac{E_{\mathrm{p}_2}\mathrm{p}_{1\parallel} - E_{\mathrm{p}_1}\mathrm{p}_{2\parallel}}{\sqrt{s}} \\ \mathbf{p}_{\perp \rm cm} &= \mathbf{p}_{\perp} = \mathbf{p} - \mathrm{p}_{\parallel}\hat{\mathbf{v}}_{\rm cm} = \frac{\mathbf{p}_1\mathrm{p}_{2\parallel} - \mathbf{p}_2\mathrm{p}_{1\parallel}}{|\mathbf{p}_1 + \mathbf{p}_2|}. \end{aligned} \tag{2.42}$$

Similarly, the transformation for $\mathbf{p}'_{\rm cm}$ is obtained with the replacements $\{\mathbf{p}_1 \to \mathbf{p}'_1, \mathbf{p}_2 \to \mathbf{p}'_2\}$, together with the constraint on total momentum conservation $\mathbf{p}_1 + \mathbf{p}_2 = \mathbf{p}'_1 + \mathbf{p}'_2$. The $\cos(\theta_{\rm cm})$ in Eq. (2.38) can be obtained using Eq. (2.42). The Galilean CM transformations are recovered in the nonrelativistic limit. In the on-shell limit, the relativistic CM transformation used in Ref. [68] is recovered. Also, $\mathbf{p}_{\rm cm}$ does not depend on energy, as in the nonrelativistic case; thus better analyticity properties are achieved, when compared to the scheme used in [95, 69]. In practice, the imaginary part of selfenergies calculated by the new scheme tends to be 10% larger at its peak value.

3. FORMALISM TO CONSTRAIN INPUTS BY LATTICE QCD*

The Hamiltonian given in Eq. (2.14) is the input to our approach that needs to be constrained by independent information. To achieve this, we will make extensive use of first-principles lQCD computations, where we treat the pertinent data as “observables" in imaginary time. Specifically, we will utilize the QGP EoS [54, 5], HQ free energies [55, 56, 2], and Euclidean quarkonium correlators [58, 59, 3, 4]. In this chapter, we elaborate on the concrete procedure to do that, which includes theoretical developments to best take advantage of the comparisons within the T-matrix approach. In Sec. 3.1 we briefly recapitulate the LWB formalism [72, 73, 74] to compute the in-medium single- and two-body interaction contributions to the EoS for the effective Hamiltonian and lay out the corresponding matrix-log technique to resum the pertinent skeleton diagrams [75, 77]. In Sec. 3.2 we recall the formalism to calculate the static-quark free energy from the T-matrix, where large imaginary parts turn out to play a critical role [57]. In Sec. 3.3 we briefly review the formalism to calculate quarkonium correlator ratios based on Refs. [60, 68, 69], thereby introducing an effective way to account for interference effects in the complex potential for quarkonium spectral functions.

3.1 Equation of State

The equation of state (EoS) of a medium usually refers to the pressure as a function energy density, or, alternatively, as a function of temperature and chemical potential, $P(T, \mu)$. It characterizes the macroscopic dynamics of the bulk which are ultimately driven by the relevant microscopic degrees of freedom of the medium. Although the EoS depends on the interactions in the system, it is usually most sensitive to the masses of the prevalent de-

*Part of this chapter is reprinted with permission from “T-matrix approach to quark-gluon plasma” by Shuai Y. F. Liu and Ralf Rapp, 2018, Phys. Rev. C **97**, 034918, Copyright 2018 by APS.

grees of freedom in the medium (which, however, may be generated dynamically through the interactions, *e.g.*, via bound-state formation). Therefore, comparing the calculated EoS with lQCD results is expected to primarily constrain the "bare" parton masses in the Hamiltonian, Eq. (2.14).

For a homogeneous grand canonical ensemble, the EoS is encoded in the grand potential (per unit volume), $\Omega = -P$, which can be calculated using diagrammatic techniques within the LWB formalism [72, 73, 74] (for recent applications to QCD matter, see also Refs. [100, 64, 101]) as spelled out in Sec. 3.1.1. Since the QGP near T_c can be expected to be a mixture of interacting partons and their bound states, a nonperturbative ladder resummation for the two-body amplitudes is in order. Some care needs to be exerted since the ladder resummation to calculate Ω is not the same as for the T-matrix, due to a double-counting when closing the external legs of the latter. This will be carried out using a matrix-logarithm resummation technique [75, 77] detailed in Sec. 3.1.2. In Sec. 3.1.3, we discuss several generalized thermodynamic relations for the LWB formalism when the "bare" masses and potential depend on the temperature and chemical potential.

3.1.1 Properties of the LWB Formalism

The diagram language of the LWB formalism leads to the following expression for grand potential,

$$\Omega = \mp \frac{-1}{\beta} \sum_n \mathrm{Tr}\{\ln(-G^{-1}) + [(G^0)^{-1} - G^{-1}]G\} \pm \Phi \tag{3.1}$$

where we combined spin, color, flavor and momentum summations in the trace operation, "Tr", while explicitly writing the Matsubara frequency sum, $\sum_n$. Here,

$$\Phi = \sum_{\nu=1}^{\infty} \Phi_\nu \tag{3.2}$$

denotes the Luttinger-Ward functional (LWF), and

$$\Phi_\nu = \frac{-1}{\beta}\sum_n \mathrm{Tr}\{\frac{1}{2\nu}(\frac{-1}{\beta})^\nu[(-\beta)^\nu\Sigma_\nu(G)]G\} \tag{3.3}$$

and $\Sigma_\nu(G)$ are the LWF and selfenergy at ν^{th} order of the potential in the "skeleton" expansion [72]. These three quantities should be understood as functionals of the full single-particle propagator, G. The full selfenergy is the sum of all selfenergies of order ν, $\Sigma(G) = \sum_\nu \Sigma_\nu(G)$. The extra factor $1/\nu$ in Eq. (3.3) complicates the resummation of $\Phi(\Sigma_\nu)$ for ladder diagrams, to be discussed in the next section. The factor $(-1/\beta)^\nu(-\beta)^\nu$ aims to separate out the $-1/\beta$ temperature dependence from loop integrals in the self-energy, such as $-1/\beta\sum_n X_1(\omega_n)X_2(z_m - \omega_n)$. At ν^{th} order, there are ν loops, with the pertinent factor $(-1/\beta)^\nu$. After this separation, $[(-\beta)^\nu\Sigma_\nu(G)]$ only has a temperature dependence stemming from G and the interaction kernel, V. This separation procedure is convenient for proving thermodynamic relations involving temperature derivatives, cf. Sec. 3.1.3.

The skeleton diagram expansion for the selfenergy can be obtained via a functional derivative of Φ,

$$\Sigma(G) = \frac{\delta\Phi}{\delta G}\,. \tag{3.4}$$

The functional derivative is equivalent to cut open one G line in a closed loop [72]. Since there are ν equivalent G lines at ν^{th} order, this cancels the factor $1/\nu$ and recovers the full selfenergy. With the help of Eq. (3.4) one finds the thermodynamic potential to reach an extremum,

$$\frac{\delta\Omega}{\delta G} = 0\,, \tag{3.5}$$

when the functional relation

$$\Sigma(G) = (G^0)^{-1} - G^{-1} \tag{3.6}$$

is satisfied. In this sense, G acts like a functional order parameter for the thermodynamic potential to reach an extremum.

In a slight variation of the standard LWB formalism, the “bare" masses (or dispersion relations, $\varepsilon(\mathbf{p})$) and potential of our effective Hamiltonian depend on temperature T and chemical potential μ_q of the medium. These dependences represent a macroscopic average over the micro-physics that we do not treat explicitly (such as remaining gluonic condensates in the QGP that can induce mass terms and the nonperturbative string term in the potential). This leads to modified expressions for several thermodynamic relations, *e.g.*, more complicated relations for energy and entropy to reconstruct the pressure; this is elaborated in Sec. 3.1.3.

3.1.2 Matrix Logarithm Resummation of Skeleton Diagrams

The main challenge in calculating the grand potential, Ω, is to evaluate the LWF, Φ. In our derivation we limit ourselves to the case of a 3D reduced T-matrix, rather than the more general 4D BSE discussed in Ref. [77], expanding on what we indicated earlier in Ref. [75].

Using the notation $\int d\tilde{p} \equiv -\beta^{-1} \sum_n \int d^3\mathbf{p}/(2\pi)^3$ with $\tilde{p} \equiv (i\omega_n, \mathbf{p})$, the ν^{th} order of the selfenergy appearing in Eq. (3.1) in ladder approximation can be formally written as

$$\Sigma_\nu(G) = \int d\tilde{p}\, [V G^0_{(2)} V G^0_{(2)} \cdots V] G \tag{3.7}$$

containing ν factors of V. Thus, the LWF functional Φ can be expressed as

$$\Phi = \frac{1}{2}\sum \mathrm{Tr}\left\{ G\left[V + \frac{1}{2} V G^0_{(2)} V + \ldots + \frac{1}{\nu} V G^0_{(2)} V G^0_{(2)} \ldots . V + \ldots \right] G \right\} \tag{3.8}$$

where "Tr" denotes, as before, a 3-momentum integral and the summation over discrete quantum numbers, while $\sum$ denotes the sum over Matsubara frequencies including β factors. The part in brackets, $[\cdots]$, has a structure very similar to the T-matrix resummation,

$$\begin{aligned} T &= V + V G^0_{(2)} V + \ldots + V G^0_{(2)} V G^0_{(2)} \ldots V + \ldots \\ &= \left[\sum_{\nu=0}^{\infty} \left(V G^0_{(2)} \right)^{\nu} \right] V \\ &= [1 - V G^0_{(2)}]^{-1} V \, , \end{aligned} \tag{3.9}$$

except for the extra coefficients $1/\nu$. However, we can write

$$\begin{aligned} & V + \frac{1}{2} V G^0_{(2)} V + \ldots + \frac{1}{\nu} V G^0_{(2)} V G^0_{(2)} \ldots V + ... \\ &= \left[\sum_{\nu=1}^{\infty} \frac{1}{\nu} \left(V G^0_{(2)} \right)^{\nu} \right] [G^0_{(2)}]^{-1} \\ &= -\ln[1 - V G^0_{(2)}][G^0_{(2)}]^{-1} \\ &\equiv \mathrm{Log}\, T \end{aligned} \tag{3.10}$$

where the (natural-base) logarithm is to be understood as a general matrix operation (in a discrete space of quantum numbers, including spin, color, flavor as well as energy-momentum), defined through its power series.[1] It can also be tested in the case of a separable potential for which the analytical result is known [95].

The similarity between the T-matrix and the $\mathrm{Log}\, T$ operation further allows to migrate

[1] A similar expression is known for the ground-state energy at zero temperature [102] and for cold-atom systems [103].

the partial-wave expansion, Eq. (2.27), and CM approximation, Eq. (2.19), from the T-matrix to the LWF. With the numerical discretization of the 3-momentum integrals as in Eqs. (2.28) and (2.29), we can define $\mathrm{Log}\, T^{l,a}_{ij}$ in a given channel as

$$\begin{aligned} \mathbb{L}\mathrm{og}\mathbb{T}(z)_{mn} &\equiv \mathrm{Log}\, T(z, k_m, k_n) \\ \mathbb{L}\mathrm{og}\mathbb{T}(z) &= -\mathbb{L}\mathrm{og}[\mathbb{1} - \mathbb{V}\hat{\mathbb{G}}^0_{(2)}(z)][\hat{\mathbb{G}}^0_{(2)}(z)]^{-1} \,. \end{aligned} \tag{3.11}$$

Compared to the T-matrix equation (2.29), the only change is replacing the inverse matrix (with an extra factor $\mathbb{V}$) by the "matrix-Log" operation, $\mathbb{L}\mathrm{og}\mathbb{T}$ (with an extra factor $[\hat{\mathbb{G}}^0_{(2)}(z)]^{-1}$). Standard software like Mathematica can compute this matrix function at a speed similar to a matrix inversion. With the result in a given channel, we first sum over partial waves using Eq. (2.26) and then transform back from the CM to an arbitrary frame using Eq. (2.24) with E_{cm}, p_{cm}, p'_{cm}, and x'_{cm} defined in Eq. (2.25),

$$\mathrm{Log}T^a_{ij}(\omega_1 + \omega_2, \mathbf{p}_1, \mathbf{p}_2|\ \mathbf{p}'_1, \mathbf{p}'_2) = \mathrm{Log}T^a_{ij}(E_{\text{cm}}, p_{\text{cm}}, p'_{\text{cm}}, x_{\text{cm}}) \,. \tag{3.12}$$

Upon closing two external lines of this quantity with a thermal single-particle propagator, G, and, in resemblance of Eq. (2.31), defining

$$\mathrm{Log}\,\Sigma \equiv \int d\tilde{p}\, \mathrm{Log}\, T\; G \,, \tag{3.13}$$

we obtain

$$\begin{aligned} \mathrm{Log}\Sigma_i(z, \mathbf{p}_1) = \int \frac{d^3\mathbf{p}_2}{(2\pi)^3} \int_{-\infty}^{\infty} d\omega_2 \frac{dE}{\pi} \frac{-1}{z + \omega_2 - E} \frac{1}{d_i} \sum_{a,j} d^{ij}_s d^{ij}_a \\ \times \mathrm{Im}[\mathrm{Log}T^a_{ij}(E, \mathbf{p}_1, \mathbf{p}_2|\mathbf{p}_1, \mathbf{p}_2)]\rho_j(\omega_2, \mathbf{p}_2)(n_j(\omega_2) \mp n_{ij}(E)) \,. \end{aligned} \tag{3.14}$$

Recalling Eq. (3.8) and the definition of LogΣ and Log$T$, we can express the LWF as

$$\Phi = \frac{1}{2}\int d\tilde{p}\; G\,\mathrm{Log}\Sigma = \frac{1}{2}\sum_j d_j \int d\tilde{p}\; G_j(\tilde{p})\,\mathrm{Log}\Sigma_j(\tilde{p})\;. \tag{3.15}$$

Therefore, the grand potential in Eq. (3.1) can be expressed in closed form as

$$\Omega = \sum_j \mp d_j \int d\tilde{p}\Big\{\ln(-G_j(\tilde{p})^{-1}) + [\Sigma_j(\tilde{p}) - \frac{1}{2}\mathrm{Log}\Sigma_j(\tilde{p})]G_j(\tilde{p})\Big\}. \tag{3.16}$$

The final sum over Matsubara frequencies in Eq. (3.16) can be carried out with usual contour techniques utilizing a spectral representation of the expression in "{ }" as a whole. Through this resummation we include the contributions of the diagrams shown in Fig. 3.1 to the grand potential Ω.

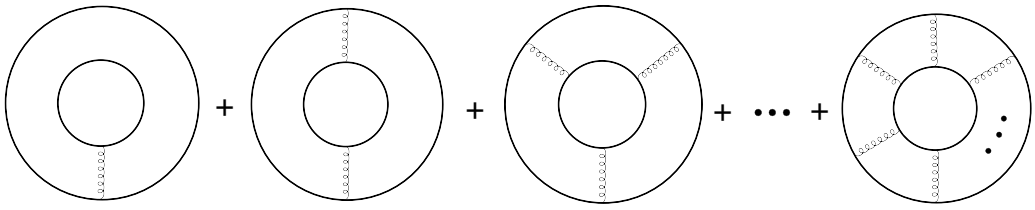

Figure 3.1: Examples of diagrams that are resummed by the generalized T-matrix for EoS.

3.1.3 Generalized Thermodynamic Relations for the LWB Formalism

The LWB formalism implies several thermodynamic relations for particle, energy and entropy densities [72, 74]. However, these relations will be modified when using an effective Hamiltonian whose "bare" single-particle masses (encoded in the dispersion relation $\varepsilon(p)$), and potential, V, depend on temperature (T) and chemical potential (μ). In this section we illustrate these modifications.

The strategy for the derivation is to start from the usual relations without T or μ dependence in the dispersion relation and potential and then generalize them to the case with T and μ dependences. For derivatives with respect to (*w.r.t.*) T or μ any implicit dependence through G will vanish. For ε and V independent of T and μ, one has

$$N = -\frac{\delta\Omega}{\delta\mu} = \pm\frac{-1}{\beta}\sum_n \mathrm{Tr}\{G\}\ , \tag{3.17}$$

since the dependence of μ through $(\delta\Omega/\delta G)(\delta G/\delta\mu)$ will vanish according to Eq. (3.5), and the only μ dependence figures from $G^{-1}_{(0)} = i\omega_n - (\varepsilon - \mu)$.

For the derivation of the energy density from the grand potential one can adopt a method in time space given in Ref. [74]. In frequency space, with a separation of the β dependence arising from the loop as in Eq. (3.1), the entropy contribution can be derived as

$$TS = \beta\frac{\partial\Omega}{\partial\beta} = -\Omega \mp \frac{-1}{\beta}\sum_n \mathrm{Tr}\{(-i\omega_n G) + \frac{1}{2}\Sigma(G)G\}\ . \tag{3.18}$$

Still, the implicit dependence on β through G will vanish. The first term comes from the derivative *w.r.t.* $(-1/\beta)$ in the frequency sum in obtaining Ω and Φ. The second term comes from the derivative *w.r.t.* $(-1/\beta)$ of ω_n in $G^{-1}_{(0)}$. The third term comes from the $(-1/\beta)^\nu$ dependence of the loop integrals in the selfenergy and gives a factor ν that cancels the $1/\nu$ factor in the skeleton expansion. With the entropy contribution, the (internal) energy U is

$$U = \Omega + TS + \mu N = \pm\frac{-1}{\beta}\sum_n \mathrm{Tr}\{[\varepsilon + \frac{1}{2}\Sigma(G)]G\} \tag{3.19}$$

where $G^{-1} = i\omega_n - (\varepsilon - \mu) - \Sigma$ by use of Eq. (3.6). We can derive Eq. (3.19) from Eqs. (3.18) and (3.17) using $GG^{-1} = 1$ and $\frac{-1}{\beta}\sum_n e^{i\omega_n\epsilon}1 = 0$ with an ϵ regulation tech-

nique [99]. This completes the derivation of the standard thermodynamic relations within the LWB formalism.

If the "bare" single-particle dispersion relation ε and the potential V of the Hamiltonian are functions of β and μ, the particle number, N, and internal energy, U, receive extra contributions,

$$N = \pm\frac{-1}{\beta}\sum_n \mathrm{Tr}\{[1 - \frac{\partial\varepsilon}{\partial\mu} - \frac{1}{2}\Sigma(G, \frac{\partial V}{\partial\mu})]G\} \tag{3.20}$$

$$\begin{aligned} U = \pm\,\frac{-1}{\beta}\sum_n \mathrm{Tr}\Big\{[\varepsilon + \beta\frac{\partial\varepsilon}{\partial\beta} - \mu\frac{\partial\varepsilon}{\partial\mu} \\ + \frac{1}{2}\Sigma(G) + \frac{1}{2}\Sigma(G, \beta\frac{\partial V}{\partial\beta}) - \frac{1}{2}\Sigma(G, \mu\frac{\partial V}{\partial\mu})]G\Big\} \end{aligned} \tag{3.21}$$

where $\Sigma(G, X) \equiv \sum_\nu \Sigma_\nu(G, X)$, and $\Sigma_\nu(G, X)$ is defined to replace one of the V's in evaluating $\Sigma_\nu(G)$ by X at each order. It can be shown that, at least for ladder and ring diagrams, it does not matter which V is replaced in the diagram because every V in the connected diagram for Φ_ν is equivalent. Thus, for the T-matrix resummation the selfenergy can be schematically written as

$$\Sigma(G, X) = T(G, X)G,\ T(G, X) = (1 - VGG)^{-1}X \tag{3.22}$$

where X is $\mu\frac{\partial V}{\partial\mu}$ or $\beta\frac{\partial V}{\partial\beta}$. Since $T(G, V) = (1 - VGG)^{-1}V$, the new logarithm can be adapted from the original T-matrix logarithm without increasing the complexity.

3.2 Color Singlet Static $Q\bar{Q}$ Free Energy

The HQ free energy, $F_{Q\bar{Q}}(r, T)$, is commonly defined as the change in free energy of a system when adding to it a static quark and antiquark, separated by a distance r (not

including the (infinite) HQ masses). In the vacuum, this simply corresponds to the potential energy between them. In medium, the free energy and the potential are still related to each other, but no longer identical [8, 104, 57], as the former includes the response of the medium to the static charges, encoded in the generally complex HQ selfenergies. However, one can *calculate* the free energy from an underlying potential within the same T-matrix approach that we discussed for the EoS above, by taking the limit $M_Q \to \infty$ [57]. This opens the possibility to extract (or at least constrain) the driving kernel of the Hamiltonian through a fit to high-precision lQCD data for $F_{Q\bar{Q}}(r,T)$. In particular, since the free energy incorporates the response of the medium to the external source, we need to couple the static quarks with the light partons of the QGP medium consistently. This is achieved by the HQ selfenergy in the QGP which we compute from the in-medium heavy-light T-matrix with the same underlying driving kernel. In the following, we first recall some basic relations for the free energy, in particular how it is related to the driving kernel of the static T-matrix (Sec. 3.2.1). Second, we discuss the selfconsistent extraction of the potential which makes contact with the QGP bulk medium (Sec. 3.2.2). In Sec. 3.2.3 we collect several additional relations implied by the formalism; and in Sec. 3.2.4, we elaborate on the connection between interference effects and the "imaginary part of potential".

3.2.1 Heavy-Quark Free Energy and Potential

In this section, we derive a relation of $F_{Q\bar{Q}}(r,T)$ with the color-singlet potential in the static limit, $V(r,T)$ [57] where we suppress color-flavor indices for simplicity in this section.

The static limit introduces simplifications which renders the relation between free energy and the potential rather straightforward. The source of this simplification is the one-

particle propagator in the infinite-mass limit [105],

$$G_Q\left(z,\mathbf{r}'\right) = \int \frac{d^3\mathbf{p}'}{(2\pi)^3} e^{i\mathbf{p}'\cdot\mathbf{r}'} \frac{1}{z-\varepsilon_{\mathbf{p}'}-\Sigma_Q\left(z,\mathbf{p}'\right)}$$
$$\approx \int \frac{d^3\mathbf{p}'}{(2\pi)^3} e^{i\mathbf{p}'\cdot\mathbf{r}'} \frac{1}{z-M-\Sigma_Q\left(z\right)} = \delta\left(\mathbf{r}'\right) G_Q\left(z\right) \ . \tag{3.23}$$

The δ-function signifies that the particle is static and $G_Q(z) = 1/(z-M-\Sigma_Q(z))$ is simply the propagator in momentum space in the static limit, *i.e.*, it is localized at its position. At vanishing quark chemical potential, $G_Q = G_{\bar{Q}}$. The two-body (4-point) Green's function inherits the δ-function structure [105],

$$G^{>}_{Q\bar{Q}}(-i\tau,\mathbf{r}_1,\mathbf{r}_2|\mathbf{r}'_1,\mathbf{r}'_2) \equiv \delta\left(\mathbf{r}_1-\mathbf{r}'_1\right)\delta\left(\mathbf{r}_2-\mathbf{r}'_2\right) G^{>}_{Q\bar{Q}}(-i\tau,r) \ , \tag{3.24}$$

where $r = |\mathbf{r}_1 - \mathbf{r}_2|$. Here, $G^{>}_{Q\bar{Q}}(-i\tau,r)$ denotes the reduced Green function with the spatial δ-functions factored out. The static $Q\bar{Q}$ free energy, $F_{Q\bar{Q}}$, can be defined in terms of the $Q\bar{Q}$ Green function as [105]

$$F_{Q\bar{Q}}(r,\beta) = -\frac{1}{\beta}\ln\left(G^{>}_{Q\bar{Q}}\left(-i\beta,r\right)\right) \ . \tag{3.25}$$

The remaining task is to calculate the Euclidean time Green function, $G^{>}_{Q\bar{Q}}(-i\tau,r)$, in Eq. (3.24) using the T-matrix, Eq. (2.19), with the propagators $G_Q(z)$ and potential $V(z,\mathbf{p}_1-\mathbf{p}'_1)$, which in coordinate space is denoted as $V(z,r)$. We here keep a dependence of the potential on the total energy, z, of the 2-particle system, which can arise, *e.g.*, from interference effects as illustrated in Sec. 3.2.3.

To proceed, we first use $G_{Q,\bar{Q}}(z)$ to obtain the non-interacting two-body propagator

figuring in the T-matrix,

$$G^0_{Q\bar{Q}}(z) = \int_{-\infty}^{\infty} d\omega_1 d\omega_2 \frac{\rho_Q(\omega_1)\rho_{\bar{Q}}(\omega_2)}{z-\omega_1-\omega_2} \; . \tag{3.26}$$

where $\rho_{Q/\bar{Q}}(\omega_1)$ are the spectral functions of the static quark/antiquark, as before. Inserting this propagator together with $V(z, \mathbf{p}_1 - \mathbf{p}'_1)$ into Eq. (2.19), one has

$$T_{Q\bar{Q}}(z, \mathbf{p}, \mathbf{p}') = V(z, \mathbf{p}-\mathbf{p}') + \int \frac{d^3\mathbf{k}}{(2\pi)^3} V(z, \mathbf{p}-\mathbf{k})\; G^0_{Q\bar{Q}}(z)\; T_{Q\bar{Q}}(z, \mathbf{k}, \mathbf{p}') \; . \tag{3.27}$$

Since $G^0_{Q\bar{Q}}(z)$ is independent of momentum, Fourier transforming the above equation from $\mathbf{p} \to \mathbf{r}$ and $\mathbf{p}' \to \mathbf{r}'$ where $\mathbf{r} = \mathbf{r}_1 - \mathbf{r}_2$, and $\mathbf{r}' = \mathbf{r}'_1 - \mathbf{r}'_2$, one arrives at

$$T_{Q\bar{Q}}(z, \mathbf{r}, \mathbf{r}') = V(z,r)\delta(\mathbf{r}-\mathbf{r}') + V(z,r) G^0_{Q\bar{Q}}(z) T_{Q\bar{Q}}(z, \mathbf{r}, \mathbf{r}') \; . \tag{3.28}$$

This is an algebraic equation with a solution $T_{Q\bar{Q}}(z, \mathbf{r}, \mathbf{r}') = T_{Q\bar{Q}}(z,r)\delta(\mathbf{r}-\mathbf{r}')$ explicitly given by

$$T_{Q\bar{Q}}(z,r) = \frac{V(z,r)}{1 - V(z,r) G^0_{Q\bar{Q}}(z)} \; . \tag{3.29}$$

We have factored out the δ function as was done in Eq. (3.24).[2] The Green function in frequency space in the static limit can be expressed as

$$G_{Q\bar{Q}}\,(z,r) = G^0_{Q\bar{Q}}(z) + G^0_{Q\bar{Q}}(z) T_{Q\bar{Q}}(z,r) G^0_{Q\bar{Q}}(z). \tag{3.30}$$

While in the non-static case, additional convolution integrals in coordinate space appear, the simple form in the static limit is due to the "$\delta(r)$" functions that can been integrated out

[2] Only one δ-function here is related to stripping off $\delta(\mathbf{p}_1 + \mathbf{p}_2 - \mathbf{p}'_1 - \mathbf{p}'_2)$. Note that $X(\mathbf{p}_1 - \mathbf{p}_2)\delta(\mathbf{p}_1 + \mathbf{p}_2 - \mathbf{p}'_1 - \mathbf{p}'_2)$ Fourier-transforms into the form $X(\mathbf{r}_1 - \mathbf{r}_2)\delta(\mathbf{r}_1 - \mathbf{r}'_1)\delta(\mathbf{r}_2 - \mathbf{r}'_2)$.

(or stripped off). Upon inserting Eq. (3.29) into Eq. (3.30) we arrive at our final expression for $G_{Q\bar{Q}}$ in energy-coordinate space,

$$G_{Q\bar{Q}}(z,r) = \frac{1}{[G^0_{Q\bar{Q}}(z)]^{-1} - V(z,r)} \,. \tag{3.31}$$

To obtain $G^{>}\left(-i\tau,r\right)$, we need to transform back to imaginary time using $(-\beta)^{-1}\sum_n G_{Q\bar{Q}}(iE_n,r)e^{-\tau(iE_n)}$; employing a spectral representation and contour technique the Matsubara sum can be carried out yielding

$$G^{>}_{Q\bar{Q}}\left(-i\tau,r\right) = \int\limits_{-\infty}^{\infty} dE' \rho_{Q\bar{Q}}\left(E',r\right) \frac{e^{E'(\beta-\tau)}}{e^{\beta E'}-1} \,. \tag{3.32}$$

Since the strength of the two-particle spectral function, $\rho_{Q\bar{Q}}\left(E',r\right)$, is located in the vicinity of the large-mass two-particle threshold, $2M_Q$, we can approximate $e^{\beta E'} \gg 1$ and $e^{E'(\beta-\tau)}/(e^{\beta E'}-1) = e^{-E'\tau}$, to obtain

$$G^{>}_{Q\bar{Q}}\left(-i\tau,r\right) = \int\limits_{-\infty}^{\infty} dE' \rho_{Q\bar{Q}}\left(E',r\right) e^{-E'\tau} \,. \tag{3.33}$$

The quantity $G^{>}\left(-i\tau,r\right)$ still depends on the infinitely large mass, M_Q (numerically taken as $2\cdot 10^4$ GeV), which needs to be "renormalized". This can be done by multiplying $G^{>}\left(-i\tau,r\right)$ with a factor $e^{2M_Q\beta}$ and redefining the energy arguments of the propagators and spectral functions by a shift of $2M_Q$. For simplicity, we will keep the same notation, *i.e.*, from here on, unless otherwise noted, the static limits of $G^{>}_{Q\bar{Q}}\left(-i\tau,r\right)$, $G_Q(z)$, $G_{Q\bar{Q}}(z)$ and $\rho_{Q\bar{Q}}(z)$ will refer to the original ones shifted as $G^{>}_{Q\bar{Q}}\left(-i\tau,r\right)e^{2\beta M_Q}$, $G_Q(z+M_Q)$, $G_{Q\bar{Q}}(z+2M_Q)$, and $\rho_{Q\bar{Q}}(z+2M_Q)$. Inserting Eqs. (3.31) and (3.33) into Eq. (3.25) with $\tau=\beta$ establishes our basic relation between the HQ potential and the free energy within the T-matrix formalism.

To be more explicit, we specify $[G^0_{Q\bar{Q}}(z)]^{-1}$ as

$$[G^0_{Q\bar{Q}}(z)]^{-1} = z - 2\Delta M_Q - \Sigma_{Q\bar{Q}}(z) \tag{3.34}$$

with medium-induced Fock mass term ΔM_Q (for each quark) determined by $V(r)$ as further discussed in Sec. 3.4, and an analytic selfenergy part, $\Sigma_{Q\bar{Q}}(z)$, labeled as a two-body selfenergy in this work. In practice, we can use $\text{Im}[[G^0_{Q\bar{Q}}(E+i\epsilon)]^{-1}] = -\text{Im}\Sigma_{Q\bar{Q}}(E+i\epsilon)$ to find the imaginary part and reconstruct $\text{Re}\Sigma_{Q\bar{Q}}(E+i\epsilon)$ by a dispersion relation. The energy dependent potential, $V(z,r)$, can also be decomposed into a static non-analytic part, $V(r)$, and an analytic part, $V_A(z,r)$, so that $V(z,r) = V(r) + V_A(z,r)$. As elaborated in Sec. 3.2.4, $V(r)$ is the input potential and $V_A(z,r)$ is related to interference effects induced by many-body physics, similar to $\Sigma_{Q\bar{Q}}(z)$. Therefore, we separate the input static potential $V(r)$ and regroup $V_A(z,r)$ into an "interfering" two-body selfenergy as $\Sigma_{Q\bar{Q}}(z,r) \equiv \Sigma_{Q\bar{Q}}(z) + V_A(z,r)$ (note that $\Sigma_{Q\bar{Q}}(z,\infty) \equiv \Sigma_{Q\bar{Q}}(z)$ since $V_A(z,\infty) = 0$), *i.e.*,

$$V(z,r) = V(r) + [\Sigma_{Q\bar{Q}}(z,r) - \Sigma_{Q\bar{Q}}(z)] \,. \tag{3.35}$$

Equation (3.31) can then be recast as

$$G_{Q\bar{Q}}(z,r) = \frac{1}{z - 2\Delta M_Q - V(r) - \Sigma_{Q\bar{Q}}(z,r)} \,. \tag{3.36}$$

With this expression, $\Sigma_{Q\bar{Q}}(z,r)$ is analytic and $2\Delta M_Q + V(r)$ is a non-analytic static part. In this scheme, the final compact form for the free energy reads

$$F_{Q\bar{Q}}(r,\beta) = \frac{-1}{\beta} \ln \left[\int_{-\infty}^{\infty} dE \, e^{-\beta E} \, \frac{-1}{\pi} \text{Im}[\frac{1}{E + i\epsilon - \tilde{V}(r) - \Sigma_{Q\bar{Q}}(E+i\epsilon, r)}] \right] \tag{3.37}$$

where $\tilde{V}(r) \equiv 2\Delta M_Q + V(r)$ is introduced for brevity.

3.2.2 Self-Consistent Extraction of the Potential

In order to use Eq. (3.37) to extract the potential, $V(r)$, we need to evaluate $\Sigma_{Q\bar{Q}}(z,r)$. Toward this end, we first calculate the one-body selfenergy, $\Sigma_Q(z)$. Taking the heavy-light T-matrix in Eq. (2.31) in the "half-static" limit where the $\mathbf{p}_1$ dependence in Eq. (2.24) is suppressed due to an infinite mass of particle-1, we obtain

$$\Sigma_Q(z) = \int \frac{d^3\mathbf{p}_2}{(2\pi)^3} \int_{-\infty}^{\infty} d\omega_2 \frac{dE}{\pi} \frac{-1}{z+\omega_2-E} \frac{1}{d_Q} \sum_{a,j} d_s^{Qj} d_a^{Qj} \times T^a_{Qj}(E, \mathbf{p}_2|\mathbf{p}_2)\rho_j(\nu, \mathbf{p}_2) n_j(\nu) \; . \tag{3.38}$$

The CM transformation in the static limit, $\omega_1 + \omega_2 \gg |\mathbf{p}_1 + \mathbf{p}_2|$, can be derived as

$$E_{\text{cm}} = \omega_1 + \omega_2, p_{\text{cm}} = p_2, \cos(\theta_{\text{cm}}) = \cos(\theta) \; . \tag{3.39}$$

The n_{ij} in Eq. (2.31) is suppressed due to infinite mass of two-body states. The selfconsistent Eq. (2.33) also applies in the static limit. For the two-body selfenergy, $\Sigma_{Q\bar{Q}}(z)$, we first use Eq. (3.26) to obtain the two-body propagator, $G^0_{Q\bar{Q}}(z)$, and then use the procedure laid out after Eq. (3.34) to arrive at $\Sigma_{Q\bar{Q}}(z)$.

In the Brueckner type setup of our approach, the r-dependent part of the two-body "interfering" selfenergy, $\Sigma_{Q\bar{Q}}(z,r)$, is not selfconsistently generated, as this would require to include 3-body interactions [3] For now, we model $\Sigma_{Q\bar{Q}}(z,r)$ with a factorizable ansatz,

$$\Sigma_{Q\bar{Q}}(z,r) = \Sigma_{Q\bar{Q}}(z,\infty)\phi(x_e r) \equiv \Sigma_{Q\bar{Q}}(z)\phi(x_e r) \tag{3.40}$$

which preserves the analyticity of $\Sigma_{Q\bar{Q}}(z,r)$. The function $\phi(x_e r)$ is motivated by the

[3] Ideas to selfconsistently generate this part are presented in Sec. 3.3.2.

imaginary part of the potential in a perturbative approximation [106, 105] and will be constrained in our context by a functional fit (within its short- and long-distance limits of one and zero, respectively). Here, x_e is a dimensionless parameter acting as a screening mass that shrinks the range of $\phi(x_e r)$ as temperature increase (our pivot point at the lowest temperature considered here is set to $x_e = 1$). Inserting Eq. (3.40) into Eq. (3.37) gives

$$F_{Q\bar{Q}}(r,\beta) = \frac{-1}{\beta}\ln\Bigg[\int_{-\infty}^{\infty} dE\, e^{-\beta E}\times \\ \frac{-1}{\pi}\mathrm{Im}\Bigg[\frac{1}{E+i\epsilon-\tilde{V}(r)-\Sigma_{Q\bar{Q}}(E+i\epsilon)\phi(x_e r)}]\Bigg] \tag{3.41}$$

where the input functions $V(r)$ and $\phi(x_e r)$ are to be tuned to reproduce lQCD data. In our initial work [57] $\Sigma_{Q\bar{Q}}(E+i\epsilon)$ was modeled by a functional ansatz with few parameters and as such was the major source of the uncertainties in the approach. Here, $\Sigma_{Q\bar{Q}}(E+i\epsilon)$ is controlled selfconsistently by the single heavy-quark/antiquark selfenergy, Σ_Q/$\Sigma_{\bar{Q}}$, as outlined above.

3.2.3 Additional Relations for the Static HQ Free Energy

Based on the setup in Sec. 3.2, we discuss additional useful relations that follow from this formalism.

First, we prove that a relation $F_{Q\bar{Q}}(\infty,\beta) = 2F_Q(\beta)$ is implicit in our formalism for the Polyakov loop defined as

$$F_Q(\beta) = \frac{-1}{\beta}\ln[\frac{-1}{\beta}\sum_{\nu_n} G_{\bar{Q}}(i\nu_n)e^{-i\nu_n\beta}]\,. \tag{3.42}$$

If we express Eq. (3.25) in frequency space,

$$F_{Q\bar{Q}}(r,\beta) = \frac{-1}{\beta}\ln\left[\frac{-1}{\beta}\sum_{E_n} G_{Q\bar{Q}}(iE_n,r)e^{-iE_n\beta}\right]\,, \tag{3.43}$$

use the fact that $\tilde{G}_{Q\bar{Q}}(iE_n,\infty) = G^0_{Q\bar{Q}}(iE_n) = -\beta^{-1}\sum_{\nu_n} G_Q(iE_n - i\nu_n)G_{\bar{Q}}(i\nu_n)$ and $iE_n = i\omega_n + i\nu_n$ with the identity

$$\begin{aligned}
&\frac{-1}{\beta}\sum_{E_n}\frac{-1}{\beta}\sum_{\nu_n} G_Q(iE_n - i\nu_n)G_{\bar{Q}}(i\nu_n)e^{-iE_n\beta} \\
&= \left(\frac{-1}{\beta}\sum_{\omega_n} G_Q(i\omega_n)e^{-i\omega_n\beta}\right)\left(\frac{-1}{\beta}\sum_{\omega_n} G_{\bar{Q}}(i\nu_n)e^{-i\nu_n\beta}\right) ,
\end{aligned} \tag{3.44}$$

and plug this into Eq. (3.43), one indeed finds $F_{Q\bar{Q}}(\infty,\beta) = 2F_Q(\beta)$, which is also satisfied in our numerical implementations.

Second, we found the following identity,

$$\tilde{V}(r) = \int dE(E\rho_{Q\bar{Q}}(E,r)) = \lim_{t\to 0} i\frac{\partial}{\partial t}G^{>}(t,r) , \tag{3.45}$$

which can be proved using a contour integral (over the large upper half circle) and the fact that $\Sigma_{Q\bar{Q}}(z,r)$ is analytic (reaching 0 at large z) for

$$\tilde{V}(r) = \frac{-1}{\pi}\mathrm{Im}\left[\int dz \frac{z}{z - \tilde{V}(r) - \Sigma_{Q\bar{Q}}(z,r)}\right] . \tag{3.46}$$

We note that $\tilde{V}(r)$ is different from the definition in Ref. [104], where it is for the long-time limit. In our approach, $V(r) = \tilde{V}(r) - 2\Delta M_Q$ is the fundamental potential figuring in the Hamiltonian which does not contain an imaginary part and reaches 0 for $r \to \infty$.

Third, we propose a possible way to obtain further constraints on the potential from lQCD data for the Wilson line, $G_{Q\bar{Q}}(\tau,r)$ [104, 71, 107], which in our context is given by

$$G_{Q\bar{Q}}(-i\tau,r) = \int_{-\infty}^{\infty} dE\, \rho_{Q\bar{Q}}(E,r)\, e^{-\tau E} . \tag{3.47}$$

These data sets can in principle provide information beyond the free-energy data. Ideally,

$\rho_{Q\bar{Q}}(E,r)$ can be obtained by inverting the $e^{-\tau E}$ kernel. This leads to

$$G^0_{Q\bar{Q}}(z) = \int dE \frac{\rho_{Q\bar{Q}}(E,\infty)}{z-E}$$
$$V(z,r) = [G^0_{Q\bar{Q}}(z)]^{-1} - [\int dE \frac{\rho_{Q\bar{Q}}(E,r)}{z-E}]^{-1} . \tag{3.48}$$

From $V(z,r)$, we can separate the input static potential $V(r)$. However, a direct inversion of the kernel $e^{-\tau E}$ in Eq. (3.47) is challenging. In our approach, we can instead calculate the spectral function $\rho_{Q\bar{Q}}$ based on quantum many-body physics with a potential ansatz just as in Sec. 3.2.1 and Sec. 3.2.2. This extra information may help to further constrain the uncertainties. However, since currently the lQCD data on $G_{Q\bar{Q}}(\tau,r)$ is not available, we only fit to lQCD free energy data as explained in Sec. 3.2.1 and Sec. 3.2.2.

3.2.4 Interference Effects and Im V

In this section, we illustrate the origin of the r-dependent imaginary part of the potential in terms of interference effects at the 3-body level and discuss future directions to define $\Sigma_{Q\bar{Q}}(z,r)$ selfconsistently embedded in the T-matrix approach. We illustrate potential conceptual problems for "Im V" and outline how they may be handled within the T-matrix framework.

The interference effects are diagrammatically illustrated in the first row of Fig. 3.2. A medium parton (top line) can scatter with either of the heavy quarks (lower two lines) interacting with each other. Therefore, the diagram equation can be schematically represented by $(\mathcal{M}_Q + \mathcal{M}_{\bar{Q}})(\mathcal{M}^\dagger_Q + \mathcal{M}^\dagger_{\bar{Q}})$. In analogy to squaring the usual coherent supposition of two quantum amplitudes, it can be separated into a non-interfering term, $|\mathcal{M}_Q|^2 + |\mathcal{M}^\dagger_{\bar{Q}}|^2$, and an interfering term, $\mathcal{M}_Q\mathcal{M}^\dagger_{\bar{Q}} + \mathcal{M}_{\bar{Q}}\mathcal{M}^\dagger_Q$. Moreover, the amplitude squared of the three-body diagram corresponds to the imaginary part of the two-body diagram by cutting the internal loops, which is the optical theorem. Thus, in the second row of Fig. 3.2 we can

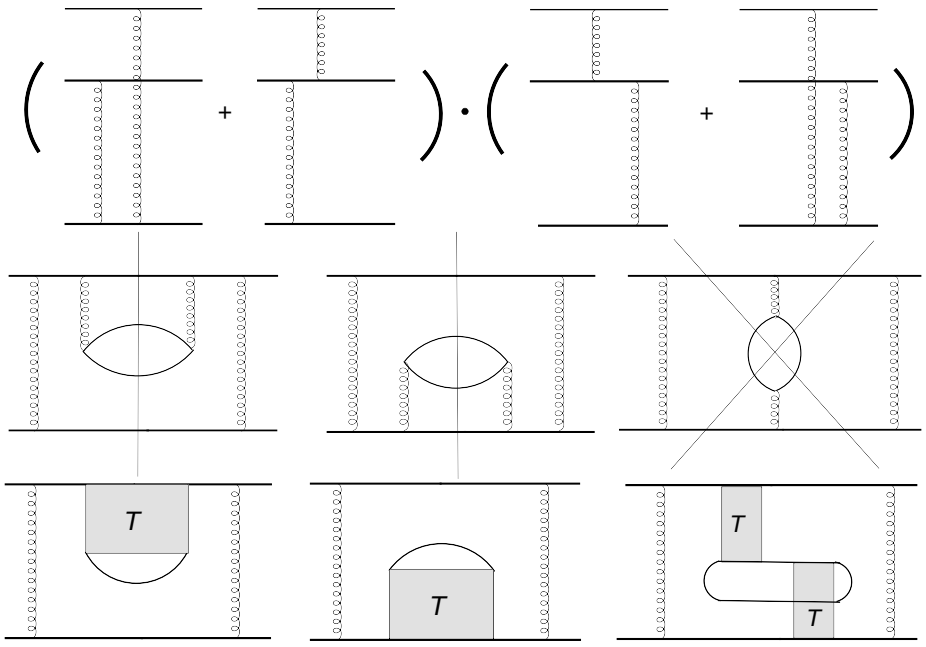

Figure 3.2: The first row depicts $\mathcal{M} \cdot \mathcal{M}^\dagger$ including interference effects that can be obtained by cutting the diagrams as shown in the second row. The third row is the T-matrix generalization of the diagrams in the second row.

identify the first two cuts in the selfenergy diagram corresponding to the non-interfering term and the two cuts in the screening diagram corresponding to the interference term. The r-independent "Im V" is the imaginary part of selfenergy while the r-dependent "Im V" (proposed by in Ref. [106]) is the interference term.

The originally proposed "Im V" is based on perturbative diagrams. Motivated by the correspondence between the diagrams in the first two rows of Fig. 3.2, and calculating the selfenergies from the T-matrix by the first two diagrams in the third row of Fig. 3.2, the interference term should correspond to the third diagram in the third row. The T-matrix configuration, $TGGT$, in the HQ t-channel interaction form a BSE (*i.e.*, energy-transfer dependent) kernel

$$K(\tilde{p}-\tilde{p}') = \int d\tilde{k}\, T_{Qq}(\tilde{k}, \tilde{k}+\tilde{p}-\tilde{p}') G_q(\tilde{k}+\tilde{p}-\tilde{p}') T_{Qq}(\tilde{k}+\tilde{p}-\tilde{p}', \tilde{k}) G_q(\tilde{k}) \ , \quad (3.49)$$

where $\tilde{p} - \tilde{p}'$ denotes the 4-momentum exchange which introduces complications in the implementation. Taking advantage of the static quarks, we can formulate it in a practically usable form. Transforming the kernel $K(\tilde{p} - \tilde{p}')$ to frequency and coordinate space as $K(\omega_n - \omega'_n, r)$, the BSE decouples in coordinate space due to the static limit and forms a matrix equation in frequency space,

$$T(iE_n, i\omega_n, i\omega'_n, r) = K(i\omega_n - i\omega'_n, r) - \frac{1}{\beta}\sum_{\lambda_n} K(i\omega_n - i\lambda_n, r)$$
$$\times G(iE_n - i\lambda_n)G(i\lambda_n)T(iE_n, i\lambda_n, i\omega'_n, r)\ . \tag{3.50}$$

Its solution can be obtained using matrix inversion in analogy to Eq. (2.29). The continuation to real time is involved due to the complicated analytical structure of the T-matrix, $T(iE_n, i\omega_n, i\omega'_n, r)$, and will not be discussed here. Instead, working in imaginary time is enough for our purpose. The BSE solves the equation for an interfering two-body *propagator* with r dependence:

$$G^{(0)}_{Q\bar{Q}}(iE_n, r) = G^0_{Q\bar{Q}}(iE_n) + (\frac{-1}{\beta})^2 \sum_{\omega_n, \omega'_n} G_Q(i\omega_n)G_{\bar{Q}}(iE_n - i\omega_n)$$
$$\times T(iE_n, i\omega_n, i\omega'_n, r)G_Q(i\omega'_n)G_{\bar{Q}}(iE_n - i\omega'_n). \tag{3.51}$$

The full four-point Green's function is solved by a T-matrix using this propagator with a bare $V(r)$ as kernel:

$$G_{Q\bar{Q}}(iE_n, r) = \frac{1}{[G^0_{Q\bar{Q}}(iE_n, r)]^{-1} - V(r)}$$
$$= \frac{1}{iE_n - 2\Delta M_Q - V(r) - \Sigma_{Q\bar{Q}}(iE_n, r)}\ . \tag{3.52}$$

Therefore, $\Sigma_{Q\bar{Q}}(z, r)$ in Eq. (3.36) is defined and calculated by the above setup in terms of $V(r)$, too. With this setup, the evaluation of $F_{Q\bar{Q}}(r, \beta)$ only depends on $V(r)$. Everything

else will be generated through the selfconsistent many-body field theory framework. With Eq. (3.43), the theoretical formalism for the potential is in a closed form, where the only input is the potential $V(r)$, defining a fully constrained functional equation for $V(r)$. This is the example that was referred to after Eq. (3.31), showing how to start from the bare $V(r)$ to obtain a dispersive $V(z,r)$ or, equivalently, $\Sigma_{Q\bar{Q}}(z,r)$.

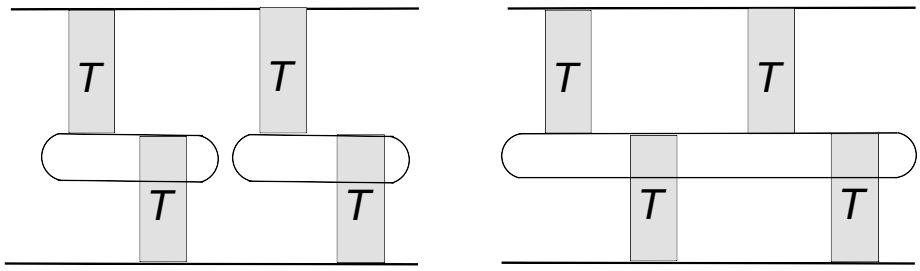

Figure 3.3: The left panel shows the diagram corresponding to the BSE implementation of loop effects in the potential, while the right panel is based on a Faddeev equation for the $Q\bar{Q}$+light-parton interaction with the thermal light-parton line being closed off.

The incorporation of loop effects in the t-channel exchange “potential" via a selfconsistent evaluation of the selfenergy is more rigorous than just forming a closed two-body equation as discussed in this section. The proper procedure should be based on a conserving approximation [73, 74] formed by the Φ derivative. This is not guaranteed for the kernel K, and this is why in the main part of this paper we have only used it to investigate the four-point Green's function, not to implement it to calculate the selfenergy. As we have illustrated in Fig. 3.2, interference effects are inherently three-body processes. Therefore, the selfconsistent treatment of interference effects requires a three-body equation, *e.g.*, a Faddeev equation [108]. However, the loop corrections to the in-medium potential are in general different when generating them through a BSE kernel compared to starting from a 3-body Faddeev approach and then contracting the in-medium light-parton line, which is

illustrated in Fig. 3.3. However, one can prove that in the Faddeev-based approach, there is an approximate 4-point Green's function that can be cast into a 2-body propagator of the form of Eq. (3.36) or (3.52). The more rigorous treatment of the 3-body equation is computationally involved and provides an interesting topic for future investigations.

3.3 Quarkonium Correlator Ratios

The Euclidean correlator can be understood as a "Fourier transform" of the spectral function to imaginary-time space, where it is computable in lattice QCD. Usually, its ratio to a correlator with a vacuum reference function is utilized to highlight the medium modifications in the spectral functions, and it also has the advantage of reducing systematic lattice uncertainties. Since the quarkonium correlator is defined by a local operator, the two-body Green function/spectral function is proportional to the wave function overlap at the origin, $G_{ij}(E) = \sum_n |\phi_{E_n}(0)|^2/(E - E_n)$. Thus, the correlator is quite sensitive to short-range physics, which is useful to, *e.g.*, constrain the strong coupling constant α_s in the Coulomb term. The spectral function and the correlator can be readily calculated in the T-matrix approach with heavy quarks. There are several previous studies of these quantities in this approach [60, 68, 69] which we will briefly review. Here, we are now able to significantly go beyond those by consistently coupling the heavy quarks to an off-shell light-parton plasma.

3.3.1 Review of Established Formalism

The correlator in Euclidean time that can be computed in lQCD [58, 59, 3] is defined by

$$G^{>}(-i\tau, \mathbf{P}) = \int d^3\mathbf{r}\, e^{i\mathbf{P}\cdot\mathbf{r}} \langle J_M(-i\tau, \mathbf{r}), J_M^{\dagger}(0,0)\rangle \tag{3.53}$$

and usually evaluated at vanishing total 3-momentum, $\mathbf{P}$, of the $Q\bar{Q}$ pair,

$$G^{>}(-i\tau) \equiv G^{>}(-i\tau, \mathbf{P})|_{P=0} \, . \tag{3.54}$$

The mesonic states are created by the local operator

$$J_M(-i\tau, \mathbf{r}) = \bar{\psi}(t, \mathbf{r}) \Gamma_M \psi(t, \mathbf{r}) \, , \tag{3.55}$$

where ψ ($\bar{\psi}$) denotes the (conjugate) Dirac spinor field operator. The Dirac matrix $\Gamma_M \in \{1, \gamma_\mu, \gamma_5, \gamma_\mu\gamma_5\}$ projects the operators into scalar, vector, pseudoscalar and pseudovector channels, respectively. In a fully relativistic treatment, ψ can create an anti-particle or annihilate a particle. However, in the context of this work, we separately treat particle annihilation and antiparticle creation (and vice versa) by two field operators ψ_Q and $\psi^\dagger_{\bar{Q}}$, respectively, schematically written as $\psi = \psi_Q + \psi^\dagger_{\bar{Q}}$ (here and in the following, we also use Q to denote c and b quarks). Inserting this into Eqs. (3.55) and (3.53) (suppressing the Γ_M structure and pertinent relativistic corrections), a leading term of the 16 possibilities for this correlator is the 4-point Green function

$$\begin{aligned} G^{>}_{Q\bar{Q}}(-i\tau, \mathbf{P}) &= \int d^3\mathbf{r} \, e^{i\mathbf{P}\cdot\mathbf{r}} G^{>}_{Q\bar{Q}}(-i\tau, \mathbf{r}, \mathbf{r}|0, 0) \\ &= \int d^3\mathbf{r} \, e^{i\mathbf{p}\cdot\mathbf{r}} \langle \psi_{\bar{Q}}(-i\tau, \mathbf{r}) \psi_Q(-i\tau, \mathbf{r}) \psi^\dagger_Q(0,0) \psi^\dagger_{\bar{Q}}(0,0) \rangle \, , \end{aligned} \tag{3.56}$$

which characterizes the propagation of a two-body state and can be solved by the T-matrix as shown in the previous section. Another important term for the same correlator is the density-density correlation function,

$$\langle n_Q(-i\tau, \mathbf{r}) n_Q(0,0) \rangle = \langle \psi^\dagger_Q(-i\tau, \mathbf{r}) \psi_Q(-i\tau, \mathbf{r}) \psi^\dagger_Q(0,0) \psi_Q(0,0) \rangle, \tag{3.57}$$

which is usually referred to as the zero-mode contribution (or Landau cut) and closely related to the transport properties of the medium [69]. Other terms are either included automatically through the Matsubara formalism as hole excitations, or they are suppressed in the HQ limit. For the purpose of this work, we choose the simplest quantity to be compared with lQCD data, *i.e.*, the pseudoscalar channel, $\Gamma_M = \gamma_5$, which does not develop a zero mode. It corresponds to the mesonic η_c and η_b channels (including, of course, their full excitation spectrum).

Since we focus on the Euclidean time correlator at total momentum $\mathbf{P} = 0$, it simply corresponds to the T-matrix in the CM frame. The additional locality in the relative coordinate leads to one integration over 3-momentum[4]. Thus, the 4-point Green function in frequency space for the pseudoscalar channel takes the form

$$G_{Q\bar{Q}}(z) = d_Q \int \frac{d^3p}{(2\pi^3)} G^0_{Q\bar{Q}}(z,p) + \\ d_Q \int \frac{dpdp'}{\pi^3} \mathcal{R}^{\mathcal{S}}_{Q\bar{Q}}\, G^0_{Q\bar{Q}}(z,p)\, T^l_{Q\bar{Q}}(z,p,p')\, G^0_{Q\bar{Q}}(z,p') \,. \tag{3.58}$$

It includes the relativistic effects due to the projector Γ_M, encoded in the $\mathcal{R}^{\mathcal{S}}_{ij}$ defined in Eqs. (2.15), (2.16) and (2.17), cf. Refs. [60, 68, 69] for more details (in those works the $\mathcal{R}$ factor is part of the propagator, but the expressions are equivalent to the ones used here); $d_Q = 6$ denotes the spin-color degeneracy of a heavy quark. The spectral function for this Green function is defined as

$$\rho_{Q\bar{Q}}(E,T) = -\frac{1}{\pi} \mathrm{Im} G_{Q\bar{Q}}(E + i\epsilon) \,, \tag{3.59}$$

[4] $f(\mathbf{r}_1 - \mathbf{r}_2) = \int \frac{d^3\mathbf{p}}{(2\pi)^3} e^{i\mathbf{p}\cdot(\mathbf{r}_1-\mathbf{r}_2)} f(p) \to f(0) = \int \frac{d^3\mathbf{p}}{(2\pi)^3} f(p)$.

and the pertinent correlator is given by

$$G^{>}_{Q\bar{Q}}(-i\tau, T_{\text{ref}}, T) = \int_0^\infty dE \rho_{Q\bar{Q}}(E, T_{\text{ref}}) \mathcal{K}(\tau, E, T) \ , \tag{3.60}$$

with the kernel

$$\mathcal{K}(\tau, E, T) = \frac{\cosh[E(\tau - \beta/2)]}{\sinh[E(\beta/2)]} \ , \tag{3.61}$$

which can be obtained using the contour techniques with proper treatment of the retarded symmetry for the spectral function at negative E. Finally, the correlator ratio is defined as

$$R_{Q\bar{Q}}(\tau, T_{\text{ref}}, T) = \frac{G^{>}_{Q\bar{Q}}(-i\tau, T, T)}{G^{>}_{Q\bar{Q}}(-i\tau, T_{\text{ref}}, T)} \ . \tag{3.62}$$

In this ratio the denominator and the numerator carry the exact same kernel, $\mathcal{K}(\tau, E, T)$ so that the only difference is the spectral function, thus exhibiting the medium effects relative to a reference spectral function (usually taken as one at small temperature).

3.3.2 Interference Effect for Two-Body Spectral Function

As discussed in Sec. 3.2.4, the r-dependent imaginary part of the potential is a manifestation of interference effects between the two quarks when interacting with the medium; *e.g.*, in the color-singlet channel a small size $Q\bar{Q}$ state will effectively become colorless thus suppressing any interaction with the colored medium partons. Therefore, this effect is expected to become significant for deeply bound heavy quarkonia with a tight wave function. Although a full many-body treatment will require nontrivial 3-body diagrams, we will suggest a way to include the effects in the T-matrix approach which seems viable for the case of two-body spectral functions and correlators. However, we will only include the interference effects for heavy-heavy and static-static channels.

We start from the non-relativistic Schrödinger equation,

$$(-\frac{\partial_r^2}{M} + \tilde{V}_{\rm clx}(r))\varphi(r) = E\varphi(r)\ . \tag{3.63}$$

In previous works [106, 109], an energy-independent complex "potential" has been introduced; in our context we write it as $\tilde{V}_{\rm clx}(r) = V(r) + i\Sigma^I_{Q\bar{Q}}\phi(x_e r)$, where we introduced the generic notation $\Sigma^I \equiv {\rm Im}\Sigma$. Transforming it to momentum space leads to

$$\tilde{V}_{\rm clx}(\mathbf{p}-\mathbf{p}') = i\Sigma^I_{Q\bar{Q}}(2\pi)^3\delta(\mathbf{p}-\mathbf{p}') + i\Sigma^I_{Q\bar{Q}}\phi_N(\mathbf{p}-\mathbf{p}') + V(\mathbf{p}-\mathbf{p}') \tag{3.64}$$

where $\phi_N(\mathbf{p}-\mathbf{p}')$ is the Fourier transform of $\phi(x_e r) - 1$,

$$\phi_N(p) = \int d^3\mathbf{r}\, e^{i\mathbf{p}\cdot\mathbf{r}}(\phi(x_e r) - 1)\ . \tag{3.65}$$

The Schrödinger equation in momentum space then reads

$$\int \frac{d^3\mathbf{p}'}{(2\pi)^3}\Big\{\big[\frac{p^2}{M} + i\Sigma^I_{Q\bar{Q}}\big](2\pi)^3\delta(\mathbf{p}-\mathbf{p}') + i\Sigma^I_{Q\bar{Q}}\phi_N(\mathbf{p}-\mathbf{p}') + V(\mathbf{p}-\mathbf{p}')\Big\}\varphi(\mathbf{p}') = E\varphi(\mathbf{p})\ . \tag{3.66}$$

One can now follow the standard track to derive the Lippmann-Schwinger equation (LSE). The terms in the brackets "[ ]" figure in H_0, which is combined with E on the right-hand side as $(E - H_0)\varphi = V\varphi$. Then, inverting the left-hand side and adding a free solution, we obtain the general solution as $\varphi = \varphi_0 + (E - H_0 + i\epsilon)^{-1}V\varphi$. Multiplying it by V, we arrive at the T-matrix equation $T = V + (E - H_0 + i\epsilon)^{-1}VT$ using $V\phi = T\phi_0$. The part local in momentum with a δ-function in Eq. (3.64) enters the free propagator, while the part nonlocal in momentum space becomes the true potential.

To generalize the Schrödinger framework to be compatible with the T-matrix approach

discussed in previous sections (in particular in Sec. 3.2.1), a few extensions are required. Specifically, the energy-momentum dependence and analytic properties of the uncorrelated in-medium two-particle propagator need to be accounted for. Toward this end, motivated by the relation (3.34) in the static limit, we augment the constant imaginary part to an energy-dependent complex quantity, $\Sigma_{Q\bar{Q}}(z,p)$, whose local part (with a 3-momentum δ-function) encodes the dynamical single-quark selfenergies, while its non-local part accounts for interference effects (as a coefficient to the "interference" function, ϕ),

$$\begin{aligned}\tilde{V}_{\rm clx}(z,\mathbf{p}-\mathbf{p}') =&(2\pi)^3\delta(\mathbf{p}-\mathbf{p}')\Sigma_{Q\bar{Q}}(z,p)+\\ &\Sigma_{Q\bar{Q}}(z,p')\phi_N(\mathbf{p}-\mathbf{p}')+V(\mathbf{p}-\mathbf{p}')\;. \end{aligned} \tag{3.67}$$

Thus, the modified potential figuring as a kernel in the T-matrix equation takes the form

$$V_{\rm clx}(\mathbf{p}-\mathbf{p}')=\Sigma_{Q\bar{Q}}(z,p')\phi_N(\mathbf{p}-\mathbf{p}')+V(\mathbf{p}-\mathbf{p}')\;, \tag{3.68}$$

which is then subjected to a standard partial-wave expansion. The resulting spectral function does not depend on using $\Sigma_{Q\bar{Q}}(z,p)$ or $\Sigma_{Q\bar{Q}}(z,p')$ in the above equation since ϕ_N is symmetric under the exchange of $\mathbf{p}$ and $\mathbf{p}'$. With this setup, the T-matrix is still analytic but no longer positive-definite. The latter feature causes complications when utilized in many-body calculations of single-particle selfenergies. It is indicative of a non-conserving approximation [73]. However, when restricted to the calculation of the quarkonium spectral functions and correlators, the former remains strictly positive definite. In addition, this scheme precisely recovers the implementation of V_I in the static limit. In Sec. 4.2.2, we will elaborate on the interference effects for the spectral functions obtained from this implementation.

3.4 Potential Ansatz and Numerical Procedure

3.4.1 Screened Cornell Potential and Bare Parton Masses

For the Hamiltonian introduced in Eq. (2.14), the inputs are the 2-body potential and bare particle masses which both depend on temperature. As an ansatz for the potential, we employ a generalized in-medium Cornell potential [110, 111]:

$$V(r) = V_{\mathcal{C}} + V_{\mathcal{S}} = -\frac{4}{3}\alpha_s \frac{e^{-m_d r}}{r} - \frac{\sigma e^{-m_s r - (c_b m_s r)^2}}{m_s} \,, \tag{3.69}$$

which recovers the well-established vacuum form while implementing in-medium screening of both the short-range Coulomb and long-range confining interaction ("string term") in a transparent and economic way. The respective screening masses are denoted by m_d and m_s. An additional quadratic term, $-(c_b m_s r)^2$, in the exponential factor of the string term accelerates the suppression of the long-range part, mimicking a string breaking feature. It can also be considered as the next term in a power expansion in r.

Since the screening originates from the coupling of the bare interaction to medium partons, both m_s and m_d are functions of the parton density, and thus they are not totally independent. The $1/r$ and r dependence of the potential leads to static propagators in momentum space, $D_c(q) = 1/q^2$ and $D_s = 1/q^4$, respectively, which, upon multiplication with the respective coupling constants, $-4/3\alpha_s$ and $-8\pi\sigma$ in the color-singlet channel, constitutes the bare potential in the Hamiltonian. The screening effects at leading order can therefore be expected to be of a generic form,

$$D_c(r) = \frac{1}{p^2 + A\alpha_s \Pi} \tag{3.70}$$

$$D_s(r) = \frac{1}{p^4 + B\sigma \Pi} \,, \tag{3.71}$$

with a medium-induced polarization tensor Π representing light-parton loops[5] which are only related to medium properties. Thus, they are the same for Coulomb and string terms. However, the same Π can lead to different screening behavior since Coulomb and string potentials couple to Π differently. Here, we simply assume that this difference can be represented by temperature-independent parameters A and B related to spin/color and relativistic structures which are not precisely known in our context. From dimensional analysis a "propagator" of the form $1/(p^n + m_x^n) = m_x^{-n}/[(p/m_x)^n + 1]$ has a screening mass proportional to m_x. Thus, we have $m_d \propto (A\alpha_s\Pi)^{1/2}$ and $m_s \propto (B\sigma\Pi)^{1/4}$. This yields the constraint $m_s = (c_s m_d^2\sigma/\alpha_s)^{1/4}$ where c_s is depending on A and B and other temperature-independent constants. In a Debye-Hückel approach [109] one obtains the same temperature scaling relation for string and Debye masses except for the coefficient c_s. However, the resulting screening behavior of the above model and the Debye-Hückel approach can be different. Thus, we do not directly use the above propagators or the Debye-Hückel approach as our ansatz but simply use scaling rules with c_s as a parameter for the Coulomb or string screening masses, which show indications of model independence. The above potential is in the quark-antiquark color-singlet channel, while the potentials in other channels will be modified according to Eqs. (2.16) and (2.17) and Table. 2.1.

In our fit procedure, we first constrain the infinite-distance limit of the input potential $\tilde{V}(r)$ by using $F_{Q\bar{Q}}(\infty,\beta)$ ($\tilde{V}(\infty)$ and $F_{Q\bar{Q}}(\infty,\beta)$ are not the same). Then, the "interference function", $\phi(x_e r)$ defined in Eq. (3.40), is constrained via Eq. (3.41), which is a functional fit. The solution for $\phi(x_e r)$ is unique once $V(r)$ is fixed (it will turn out to have a shape similar to the perturbative limit in Ref. [106], as will be shown in Figs. 4.2 and 4.13 in Secs. 4.1.1 and 4.2.1).

For the in-medium quark mass correction, we have previously defined $\tilde{V}(r)$ by adding

[5]The leading order polarization is just a particle-hole loop.

twice the Fock term, $\Delta M_Q = \tilde{V}(\infty)/2$, to the genuine interaction part of $V(r)$, *i.e.*,

$$\tilde{V}(r) = V_{\mathcal{C}}(r) + V_{\mathcal{S}}(r) + 2\Delta M_Q \tag{3.72}$$

where

$$\Delta M_Q = -\frac{1}{2}\int dr\rho(r)V(r) = \frac{1}{2}(-\frac{4}{3}\alpha m_d + \sigma m_s) \tag{3.73}$$

is the classical static in-medium selfenergy of a point charge, $\rho(r) = \delta(r)$, in its own field, subtracting the divergent vacuum term. The minus sign can be verified using the perturbative calculation. Similar physics is discussed in Ref. [112] in the perturbative context. Using Eq. (3.73) in momentum space with explicit indices, the Fock mass can be obtained by the selfenergy from a potential including the relativistic and color factors, Eqs.(2.16) and (2.17),

$$\begin{aligned} M_q &= -\frac{1}{2}\int \frac{d^3\mathbf{p}}{(2\pi)^3} V^1_{q\bar{q}}(\mathbf{p}) + M_{\text{fit}} \\ M_g &= -\frac{1}{2}\int \frac{d^3\mathbf{p}}{(2\pi)^3} V^1_{gg}(\mathbf{p}) + \frac{3}{2}M_{\text{fit}} \end{aligned} \tag{3.74}$$

where M_{fit} is a residual mass (utilized as a fit parameter to the lQCD data for the EoS), which encodes physics that we do not treat explicitly here (*e.g.*, perturbative selfenergies or gluon condensate effects)[6]. The non-perturbative gluon-quark mass ratio in the static limit is $M_g/M_q = C_A/C_F = 9/4$, while in the perturbative limit at high T one has $M_g/M_q = 3/2$. The above implementation gives a smooth transition from the non-perturbative to the perturbative regime. However, the mass dependence in the relativistic factor still requires a selfconsistent procedure. We have checked that our default mass fitting scheme, using Eq. (3.74), and enforcing only the perturbative limit (described in the footnote. (6)) give

[6]Neglecting the relativistic factor in Eq. (3.74), the relation is $M_q = \frac{\tilde{V}(\infty)}{2} + M_{\text{fit}}$, $M_g = \frac{9}{4}\frac{\tilde{V}(\infty)}{2} + \frac{3}{2}M_{\text{fit}}$.

very similar results, with a maximum difference of 1% for the resulting quark masses, up to 15% for the gluon masses, 10% for the selfenergy near $T \approx 0.2$ GeV, and at the 5% level for gluon masses and selfenergies at $T \approx 0.3$ GeV. In either case the influence on the emerging spectral properties is not significant. Preliminary results show that the quark-number susceptibilities are rather sensitive to the masses and can provide additional constraints; this will be elaborated in future work.

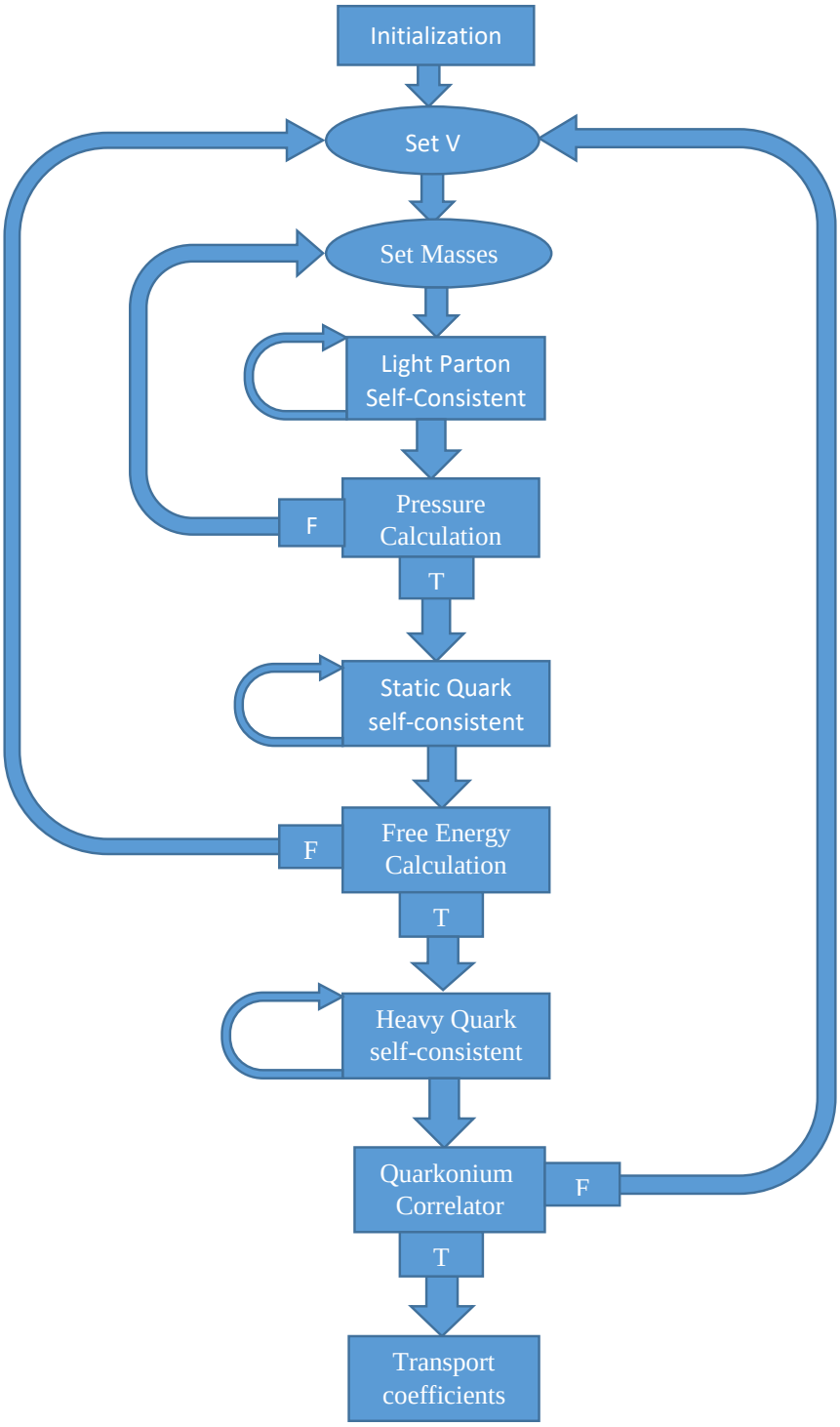

Figure 3.4: Flow chart of the procedure. “T” means the result agrees with the corresponding lQCD data and “F” means it fails to describe the lQCD data.

3.4.2 Numerical Fit Procedure for lQCD Data

Let us briefly lay out the numerical procedure we use to search for solutions of our approach that are compatible with the lQCD data for the QGP EoS, quarkonium correlators and static $Q\bar{Q}$ free energies. The flow chart of the procedure is shown in Fig .3.4. At each temperature, we start with trial values for the potential and two light parton masses, and use them to calculate the non-perturbative off-shell scattering matrices (T-matrices) for light partons. Within the formalism laid out in Sec. 2.2, we keep 6 partial waves to include two-body channels with angular momentum up to l=5 (which is more than sufficient for convergence); with four color channels in the qq and $q\bar{q}$, three in the qg and three in the gg sector [8], a total of 6×10=60 different light-parton T-matrices are computed. These T-matrices are then used to calculate the selfenergies and spectral functions for single partons. Next, the parton propagators are reinserted back into the T-matrices, forming a selfconsistency problem (recall Eq. (2.33)) which is solved by numerical iteration; this forms the "inner" light-parton selfconsistency loop of the overall procedure. In this procedure, we exit the "inner" loop after 5 iterations where a convergent solution is usually found within a few percent accuracy. The pertinent outputs are then used to compute the EoS and LWF as discussed in Sec. 3.1. If the resulting pressure disagrees with the lQCD value at the given temperature, the light-parton masses ($M_{\rm fit}$) are retuned, the inner selfconsistency loop carried out, and repeated until the pressure agrees with lQCD data within 2%, constituting the "intermediate" mass fitting loop of the overall procedure. After obtaining the masses to reproduce the lQCD EoS, we proceed to the selfconsistent calculation of the selfenergy of a static quark (again a selfconsistency loop), which involves another 42 static-light T-matrices (6 partial waves and a total of seven color channels for Qq, $Q\bar{q}$ and Qg). These are input to the formalism laid out in Sec. 3.2 to compute the static-quark free energy, $F_{Q\bar{Q}}$, and compare it to pertinent lQCD data. If the calculated free energy dis-

agrees with the lQCD data, we retune the potential (most notably m_d), recalculate the EoS with retuned light-parton masses, and recompute the free energy, which corresponds the "outer" potential fitting loop of the procedure. The criterion to end this "outer" loop is that the calculated $F_{Q\bar{Q}}(\infty)$ agrees with lQCD data within 5%. These loops involve automated (numerical) adjustments of M_{fit} and m_d to best reproduce the EoS and free-energy data while other parameters are tuned manually. After obtaining a solution, we proceed to the selfconsistent calculations of charm- and bottom-quark properties which involve another 42 heavy-light T matrices each. With the full off-shell HQ spectral functions, we proceed to evaluate two more T-matrices to compute charmonium and bottomonium spectral functions and correlator ratios in the pseudoscalar color-singlet S-wave channel, and compare the latter to lQCD data as discussed in Sec. 3.3. If they do not match, i.e., if the maximum deviation is significantly larger than 10%, we manually retune the potential (mostly the Coulomb term) and redo the whole process until a satisfactory result is obtained. Usually, the fits to the correlator ratio is automatically "satisfactory" with the assumption that α_s does not strongly depend on temperature. The numerical machinery is carried out with *Mathematica* software and typically takes several hundreds of CPU hours to arrive at a solution for four temperatures.

4. NUMERICAL RESULTS AND UNDERLYING PHYSICS*

In this chapter, we discuss the results and insights from the formalism described in the previous chapters. For each solution at a given temperature, all quantities in both HQ and light-parton sectors, *i.e.*, the QGP EoS, HQ free energy, one- and two-body spectral functions and T-matrices, are calculated from a single Hamiltonian, Eq. (2.14), with the potential ansatz described in Sec. 3.4, and then using the T-matrix approach with one set of parameters. The interference effect discussed in Sec. 3.3.2 is only included when evaluating static-static and heavy-heavy spectral functions and correlators/free energies.

As it turns out, the constraints provided by the currently used set of lQCD data (free energies, quarkonium correlators and EoS) does not yet allow for a unique solution. To explore this feature, we will focus on two putatively limiting cases, which we denote by a weakly coupled solution (WCS) where the potential is close to the free energy (Sec. 4.1) and which has already been discussed in the literature in perturbatively inspired frameworks [105, 71], and a strongly coupled solution (SCS) which is characterized by a long-range potential which "maximally" rises above the free energy (Sec. 4.2), first pointed out in Ref. [57]. Although both solutions can explain the chosen set of lQCD data, they predict, as we will see, a rather different microscopic structure of the QGP at moderate temperatures.

A similar discussion has been presented before in phenomenological applications heavy-flavor observables, both for HQ diffusion [68, 113] and quarkonium transport [114, 115, 116, 117, 29, 30]. In these instances the internal and free energies have been employed as potential proxies for strongly and weakly coupled scenarios of the in-medium QCD force. A general tendency for preferring the internal energy was found. Such studies can,

*Part of this chapter is reprinted with permission from "T-matrix approach to quark-gluon plasma" by Shuai Y. F. Liu and Ralf Rapp, 2018, Phys. Rev. C **97**, 034918, Copyright 2018 by APS.

of course be repeated with our more rigorously deduced potential solutions.

One of the virtues of our approach is that it is carried out in real-time, allowing us to retain and keep track of the microscopic quantum many-body information of the system in a direct way while being intimately connected to the macroscopic properties of the QGP. This includes the predicted spectral functions of all involved partons (static, heavy and light quarks as well as gluons) and the more than one-hundred in-medium two-body T-matrices, fully off-shell. This information readily allows to calculate transport coefficients, Wigner functions for one- or two-body states, etc., in a nonperturbative framework, and to make contact with experimental observables. Thus, the approach is not only rooted in lQCD data, but also unravels real-time microscopic physics which leads to a wide variety of phenomena that can be tested by experiments in a transparent, quantitative and interpretable way.

4.1 Weakly Coupled Solution

In this section we first report and discuss the results of our fits for a weakly coupled solution (WCS), starting from the HQ free energy and the extraction of the underlying potential, which is the key quantity determining the interaction strength in the QGP (Sec. 4.1.1) and pivotal for calculating essentially all other quantities. In Sec. 4.1.2 we elucidate the extra information that can be gained by the fits of Euclidean quarkonium correlators, and discuss the resulting charmonium and bottomonium spectral functions. We then proceed to our fit to the QGP EoS which involves the two light-parton masses as additional fit parameters (Sec. 4.1.3). We finally give a comprehensive overview of the emerging light and heavy-parton spectral functions and their two-body T matrices (Sec. 4.1.4) and a discussion of the pertinent QGP structure, including its degrees of freedom.

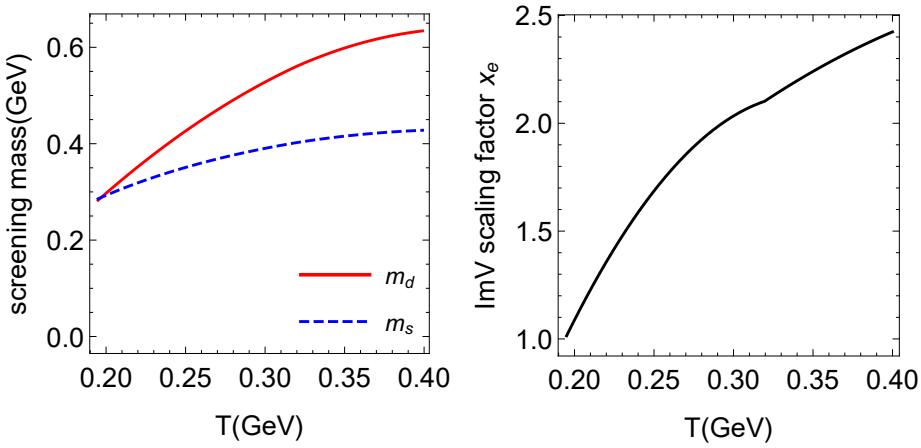

Figure 4.1: Results of a *weakly* coupled solution for the temperature dependence of the fitted screening masses (left panel) and the scale factor, x_e (right panel), figuring in the interference function. Reprinted from [1].

4.1.1 Free Energy, Potential and Static Selfenergies

When searching for a WCS, we start by using the free energy as potential. The strength of the potential slightly increases in the iteration procedure, mostly due to relatively small imaginary parts that develop and figure in the static $Q\bar{Q}$ spectral function, Eq. (3.41). Thus, the solution found in this way can be regarded as a lower limit of the potential. The parameters of the potential for the converged solution are given by $\alpha_s = 0.27$, $\sigma = 0.21\,\text{GeV}^2$, $c_b = 1.3$ and a temperature dependent Coulomb Debye mass, m_d, as shown in the left panel of Fig. 4.1. With $c_s = 0.1$ the screening mass of the string term, $m_s = (c_s m_d^2 \sigma/\alpha_s)^{1/4}$, also follows as shown in the Fig. 4.1. The fit of the interference function, shown in the lowest row of Fig. 4.2 and Fig. 4.3 is quite similar to the perturbative function found in Ref. [106]; it shrinks in range as a result of the increase in screening with temperature. The resulting potential is displayed in the third row of Fig. 4.2 and indeed found to exceed the free energy, by up to 0.07 GeV at $T = 0.194$ GeV and 0.16 GeV at $T = 0.4$ GeV. The calculated free energy fits the lQCD data well.

With this potential, the selfconsistent selfenergy and spectral function of a static quark follow from T-matrix approach as shown in the first two rows of Fig. 4.2, respectively. In practice, the static limit has been calculated with a numerically large bare HQ mass ($2 \cdot 10^4$ GeV), and the energy scales for the one- (and two-) body quantities have been plotted relative to (twice) that bare mass. At low $T = 0.194$ GeV, the peak value of Im$\Sigma_Q \approx -0.05$ GeV coresponds to a width of the spectral function which is around 0.1 GeV. For comparison, the hard-thermal-loop (HTL) perturbative width [106, 105, 112] is $\frac{4}{3}\alpha_s T \approx 0.07$ GeV. For the $Q\bar{Q}$ quantities, the peak value of ImΣ_{QQ} as defined in Eq. (3.34) and (3.40) is approximately 2 times of the peak value of ImΣ_Q, and the width of the two-body spectral function is around 2 times that of the single static-quark spectral function. The peak value of ImΣ_Q and the width of the static quark spectral functions increase with temperature at an approximately linear rate.

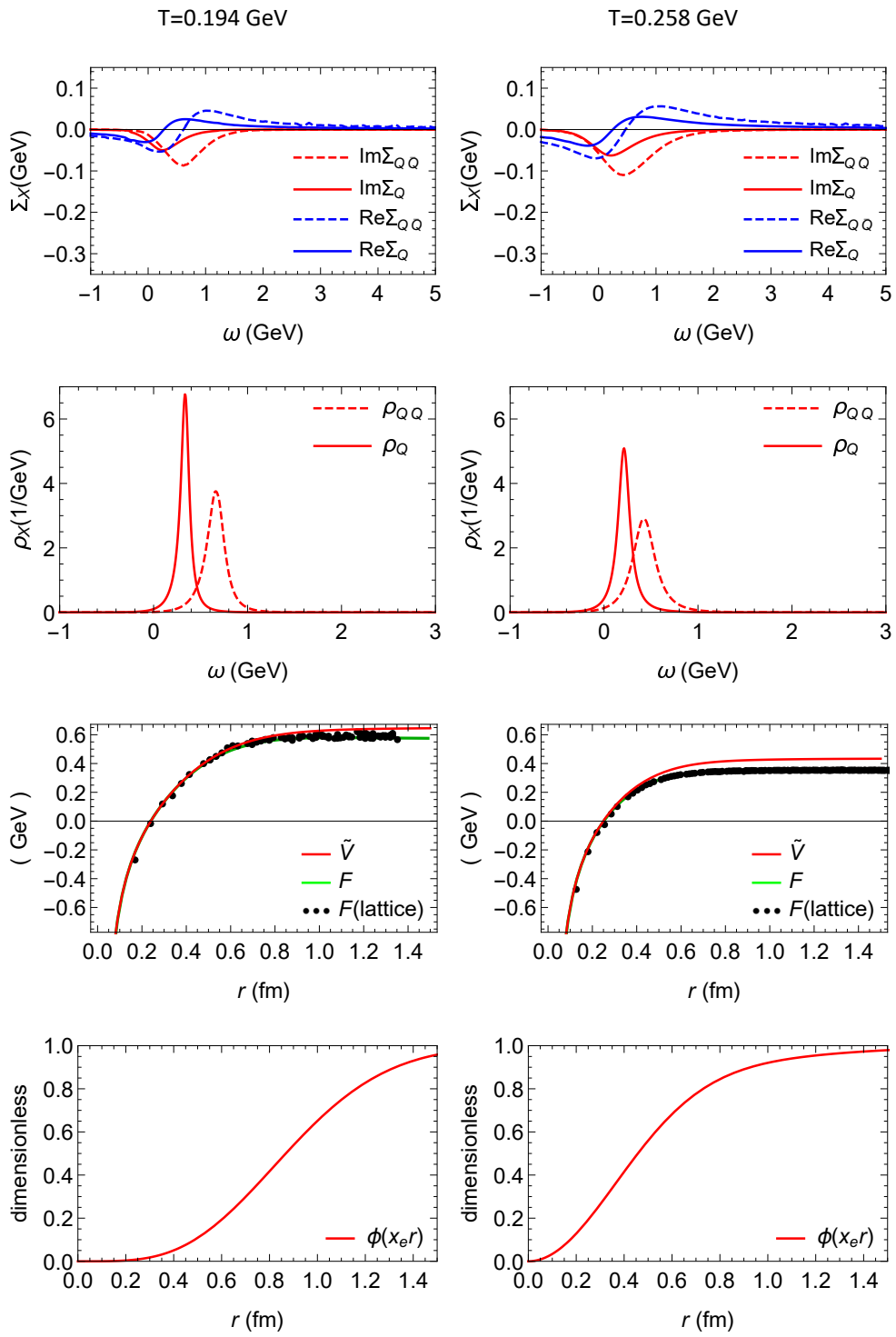

Figure 4.2: Results of a *weakly* coupled solution for the self-consistent fit to extract the static HQ potential: single-quark and $Q\bar{Q}$ selfenergies, $\Sigma_X(\omega, \infty)$ (first row), and spectral functions, $\rho_X(z, \infty)$ (second row), potential $\tilde{V}(r)$ and free energies (third row), and interference function, $\phi(x_e r)$ (fourth row). Reprinted from [1]. The free-energy lQCD data are from Ref. [2].

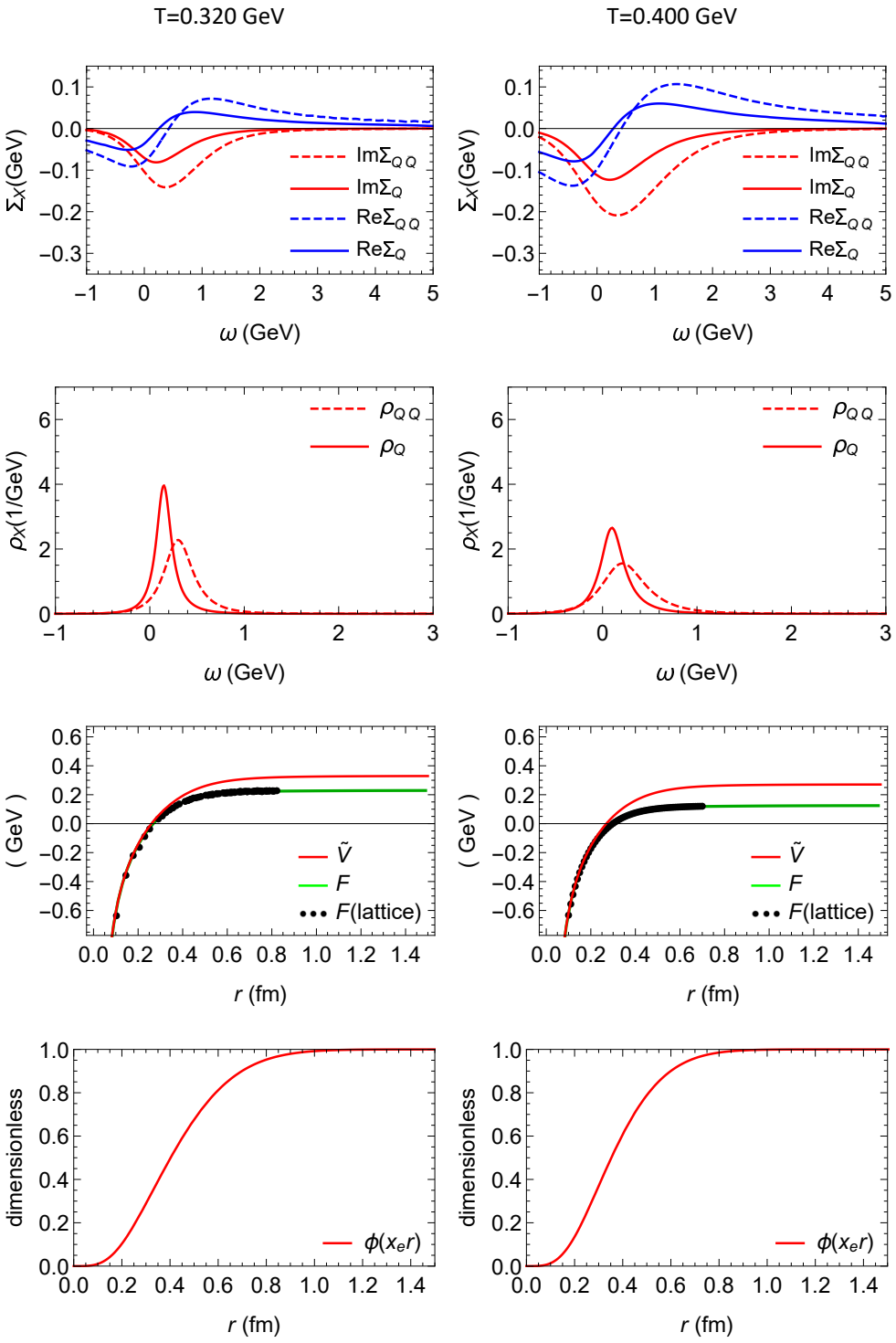

Figure 4.3: Same as Fig 4.2 for different temperature. Reprinted from [1].

4.1.2 Quarkonium Correlators and Spectral Functions

Next we turn to the Euclidean quarkonium correlators for realistic bottom- and charm-quark masses, concentrating on the pseudoscalar channel where extra complications due to zero modes do not figure. The bare masses of charm and bottom quarks (Q=c, b) are determined as in Ref. [68], by fitting the vacuum charmonium and bottomonium ground-state masses using $m_Q = m_Q^{\rm bare} + \tilde{V}(\infty)/2$ with the vacuum value of $\tilde{V}$ at a typical string breaking scale of r=1-1.1 fm, resulting in $m_{c,b}^{\rm bare}$=1.264, 4.662 GeV. The results for this section are collected in Fig. 4.4 and Fig. 4.5.

The widths of the quarkonium spectral functions are caused by collisions of individual heavy quarks within the bound state with medium partons (the so-called quasifree process [26]), as encoded in the HQ selfenergies. Since the potential is relatively weak, these selfenergies are small, and so is the width of quarkonium. The η_c is still a well-defined state at T=200 MeV, but is essentially dissolved at T=260 MeV. The $\eta_b(1S)$ survives to significantly higher temperatures, beyond 260 MeV, and even to 400 MeV when interference effects are included (as described in Sec. 3.3.2). The latter generally reduce the quarkonium widths, more so the tighter the states are bound (by up to 75%). The width reduction is consistent with simple estimates using the $\phi(x_e r)$ function (Fig. 4.2) with pertinent size estimates. Even for the case without interference, the width of the $Q\bar{Q}$ states is smaller than 2 times the HQ width at vanishing momentum, due to the energy-momentum dependence of the HQ selfenergies as obtained from the heavy-light T-matrices. As usual, the dissolution of the quarkonia is due to a combination of the increasing screening and collision widths.

The correlator ratios are generated by using the reference (or "reconstructed") correlator at the lowest temperature considered (T=194 MeV), as was done in the lQCD calculations that we compare to [3, 4]. Without interference effects the calculated correlator

ratios deviate from the lQCD data by up to $\sim$10%. Despite the melting of the bound states, the increase in width effects (over-) compensates the loss of low-energy strength in the spectral functions and leads to a 5-10% increase in the correlators ratios with increasing Euclidean time, τ. This increase is tamed by the inclusion of interference effects, which, as discussed above, reduce the bound-state widths; the resulting correlator ratios agree within $\sim$5% with the lQCD data. This deviation could be further reduced by implementing an α_s which decreases with temperature (in our fits we did not explore such a dependence). However, due to other uncertainties that can affect the correlator ratios at a few-percent level (*e.g.*, spin-dependent interactions), we do not further pursue this option here.

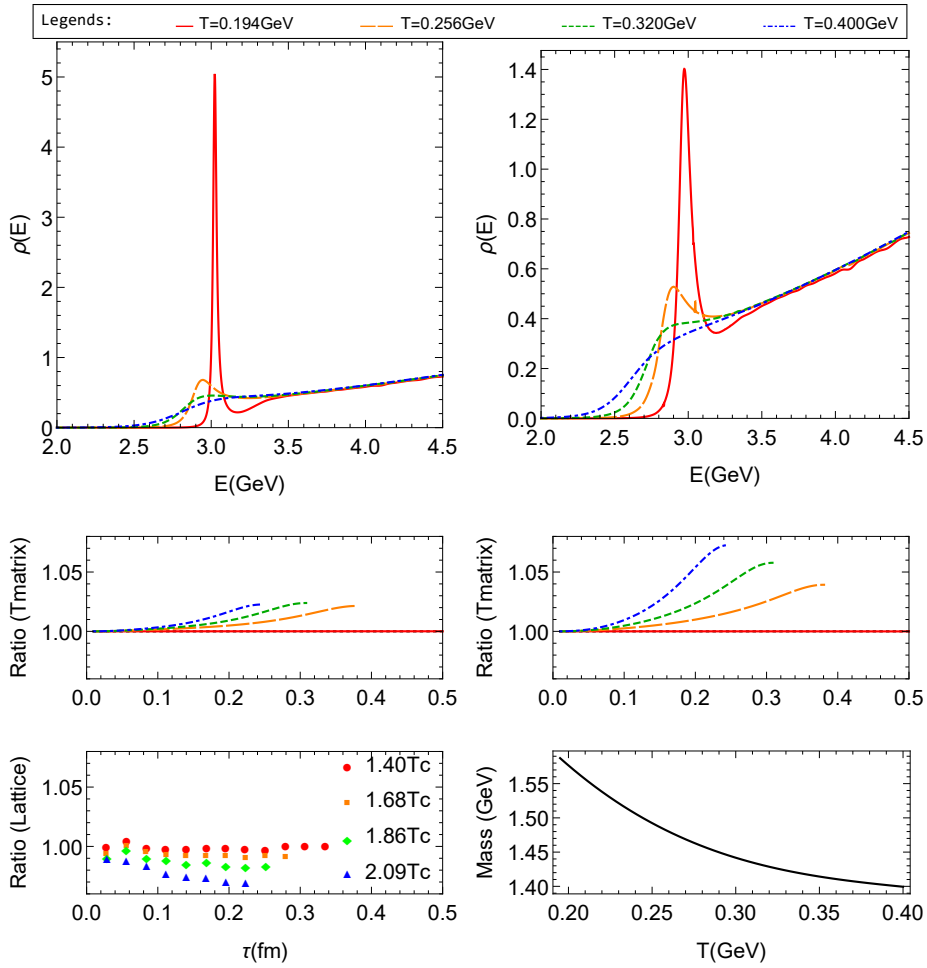

Figure 4.4: Weakly coupled solution for charmonium (η_c) spectral functions (upper panels) and correlators ratios (middle panels) with (first column) and without (second column) interference effects in the imaginary part of the potential. The lQCD data for η_c correlator ratios [3] are shown in the first bottom panel, while the second bottom panel displays the temperature dependence of the charm-quark mass. Reprinted from [1].

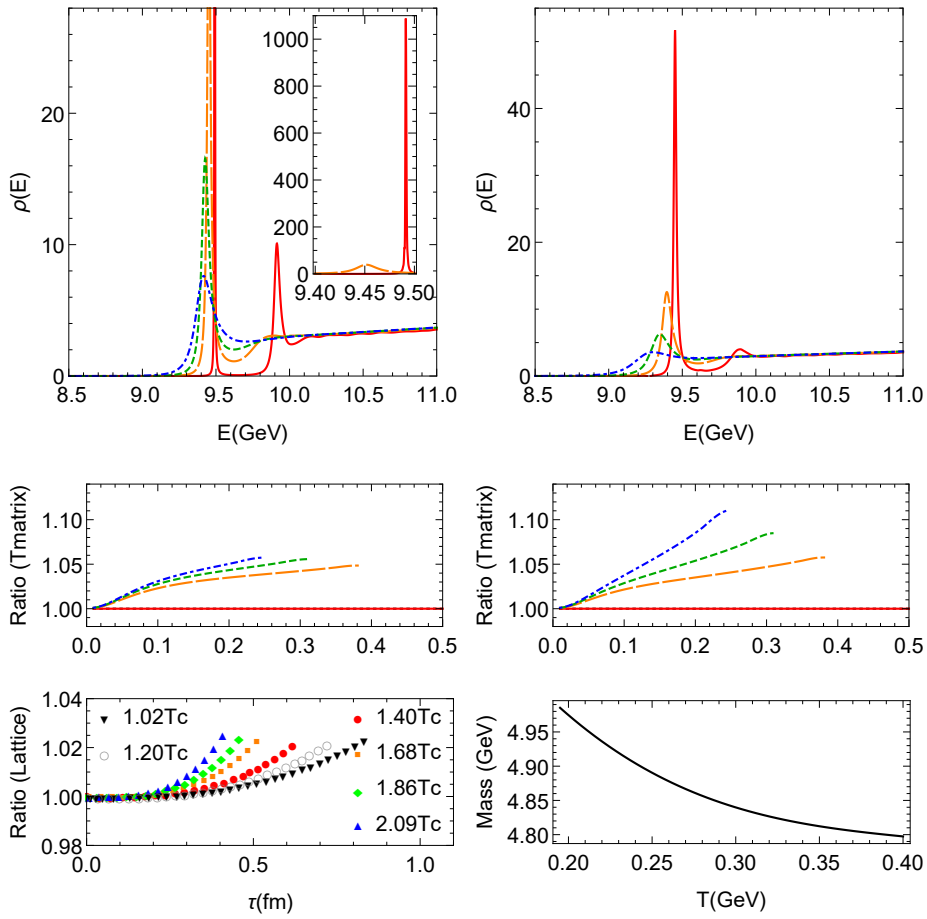

Figure 4.5: Same as Fig. 4.4 for bottomonium (η_b) with lQCD data [4]. Reprinted from [1].

4.1.3 QGP Equation of State

Next, we turn to the selfconsistent results for the QGP bulk properties, *i.e.*, our fit to the lQCD data for the pressure. Here, the two main fit parameters are the bare light-parton masses in the Hamiltonian (including the Fock term, recall Eq. (3.74)), which are shown in the left panel of Fig. 4.6. The resulting masses are rather stable with temperature, with a slight increase toward $T_{\rm pc}$ dictated by the decreasing pressure (not unlike in quasiparticle models, but less pronounced, especially for quarks). The quark-to-gluon mass ratio is different from the perturbative thermal mass ratio due to the nonperturbative ingredients

of the interaction as discussed in Sec. 3.4. The fitted mass parameter, $M_{\rm fit}$, starts to exceed M_q for temperatures above 300 MeV due the negative Coulomb contribution to the Fock term (which is also enhanced by relativistic corrections); the string term gives a strictly positive contribution (which is, however, suppressed by relativistic corrections).

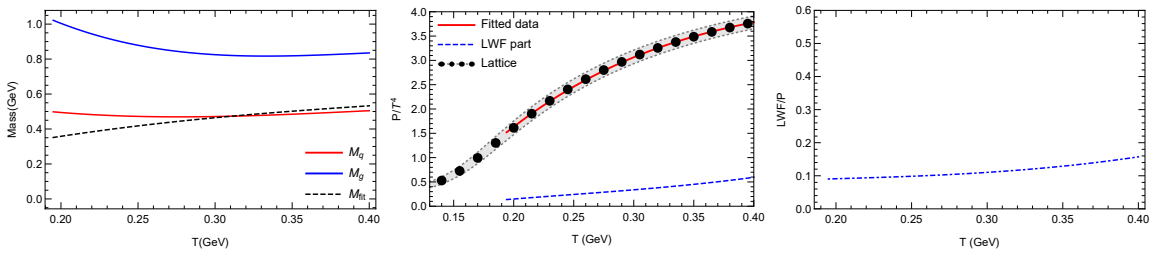

Figure 4.6: Weakly coupled solution for the QGP bulk medium: we show the fit results of the input masses for quarks and gluons (left panel), the resulting fit to the QGP pressure in comparison to lQCD data [5] (middle panel; solid line: total, dashed line: LWF contribution), and the ratio of LWF contribution to total pressure (right panel). Reprinted from [1].

The lQCD data for the pressure can be well reproduced; see the middle panel of Fig. 4.6. It is interesting to decompose the pressure into contributions from quasiparticles ($\Omega_{\rm qp} \propto \ln(-G^{-1}) + \Sigma G$) [95] and the two-body interaction characterized by the resummed LWF ($\Phi \propto 1/2\log(1 - VGG)$). The latter turns out to be generally small, no more than 15% of the total and slightly increasing with the temperature; cf. right panel of Fig. 4.6. This suggests that there are no marked changes in the interaction strength or degrees of freedom in the WCS for the QGP in the considered temperature range.

4.1.4 Spectral Structure of the QGP

Finally, let us inspect the spectral structure of the QGP within the WCS. The spectral properties of single partons are summarized in Fig. 4.7, Fig. 4.8, Fig. 4.9 and Fig. 4.10 in terms of their selfenergies (real and imaginary parts) and spectral functions. The widths (or scattering rates) of the partons, $\Gamma = -2\mathrm{Im}\Sigma$, are significantly smaller than their masses, implying that they remain well-defined quasiparticles at all momenta and over the full temperature range. At the lowest temperature, T=194 MeV, the light-parton width is around 0.11 GeV which is larger than the perturbative expectation, $\frac{4}{3}\alpha_s T \approx 0.07$ GeV, but lower than, *e.g.*, the most recent dynamical quasiparticle model results [118] which are around 0.2 GeV. Similar to the static case, the width rises slightly stronger than linear with temperature, which is closer to the perturbative than the dynamical quasiparticle approach. The 3-momentum dependence of the width is quite strong at low temperature and quite weak at high temperature. This is probably so because partons at different thermal momenta will probe different regimes of the potential, in particular since at high temperature the string term (which is responsible for an appreciable long-range force) is heavily screened. In the infrared region, the confining interaction behaves as $1/m_s^4$ while the Coulomb one as $1/m_d^2$. Thus, the increase of m_s implies a larger decrease of the strength of the string relative to the Coulomb force (the latter is also augmented by the relativistic Breit correction that reduces the momentum dependence). The width of the different quark species are quite similar whereas the gluon width is almost twice larger due to the color Casimir factor. The quark width first increases with mass and then decreases again. Usually a larger mass has a stronger scattering amplitude in the CM frame (cf. Fig. 4.11), but the CM transformation, Eq. (2.25), effectively shrinks the phase space. This competition leads to the non-monotonic behavior.

The underlying two-body correlations are illustrated by the (imaginary part of the)

pertinent T-matrices, used to calculate the single-parton selfenergy, in Fig. 4.11. They exhibit a sequential dissociation according to the reduced mass of the bound state. If we use a vanishing binding energy (relative to the constituent 2-body mass threshold) to distinguish bound and scattering states (for total momentum P=0), light mesons are melted at $T = 0.194\,\mathrm{GeV}$ while the heavy-light meson, glueball, and quarkonium still survive. The D-meson and first-excited bottomonium state (Υ_{2S}) melt near $T = 0.258\,\mathrm{GeV}$, the charmonium around $T = 0.320\,\mathrm{GeV}$ and the ground-state bottomonium Υ_{1S} at $T = 0.400\,\mathrm{GeV}$. Even after melting, a resonance structure can still survive to somewhat higher temperatures, albeit with typically much reduced strength in the T matrix. As an alternative way to characterize the resonance correlation one can inspect their robustness with increasing single-parton CM momentum (essentially going off-shell), the light, heavy-light and first-excited bottomonium states disintegrate for $p_{\mathrm{cm}} \geq 1\,\mathrm{GeV}$. We finally note that the $q\bar{q}$ bound-state mass at the lowest temperature, $M_{q\bar{q}} \simeq 1\,\mathrm{GeV}$, is significantly larger than the vacuum mass of the light vector mesons, $m_{\rho,\omega} \simeq 780\,\mathrm{MeV}$ (we recall that we do not include spin-spin or topologically induced interactions, *e.g.*, instanton-induced ones, which are believed to play a key role for dynamical chiral symmetry breaking and its associated Goldstone bosons).

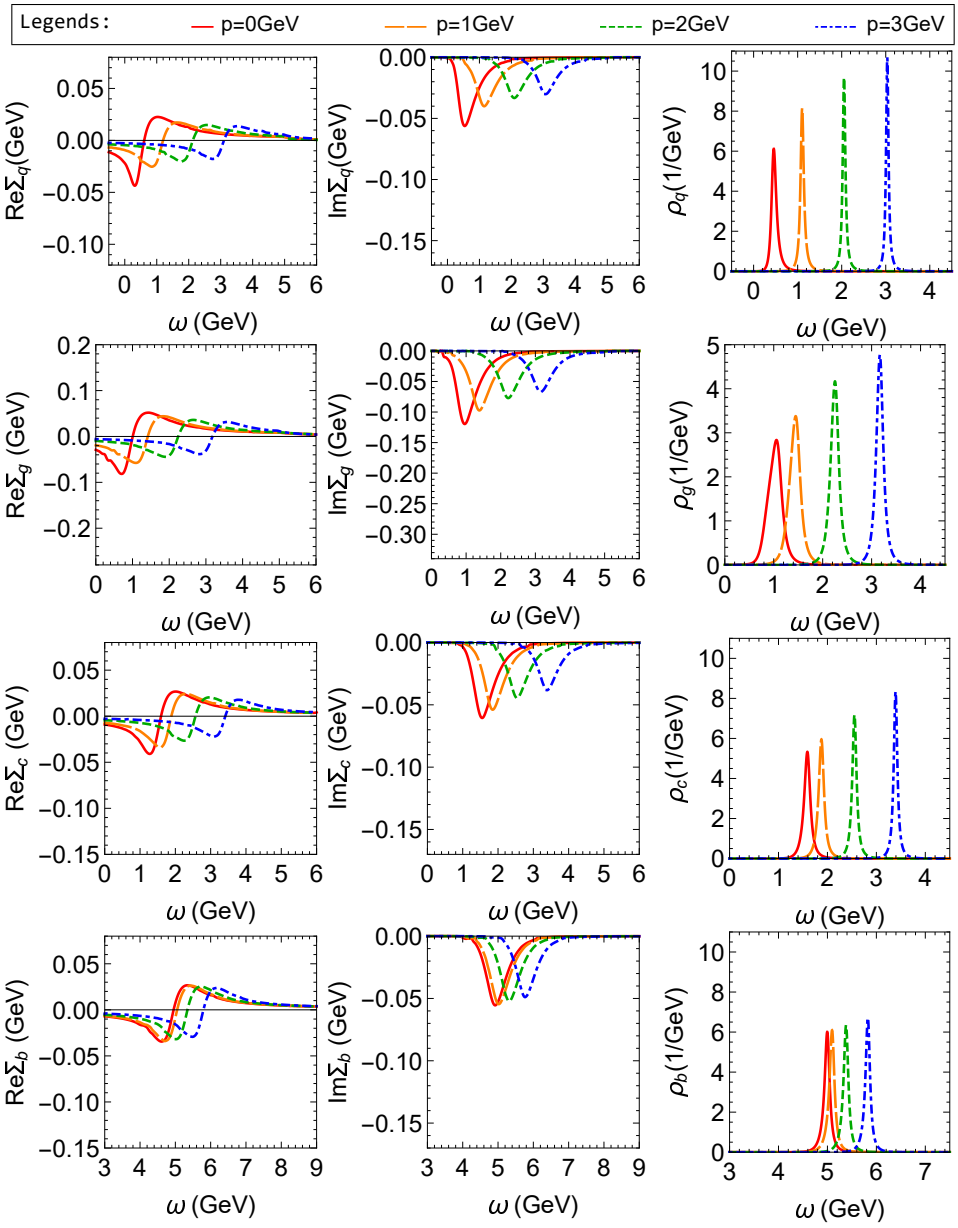

Figure 4.7: Weakly coupled solution for parton spectral properties of the QGP at $T = 0.194\,\text{GeV}$. 4 rows corresponding to different parton species (light quarks (q), gluons (g), charm quarks (c) and bottom quarks (b) in the first, second, third and fourth row of each panel, respectively). Each row contains 3 panels showing (from left to right) the energy dependence of the pertinent real and imaginary part of the selfenergy and the resulting spectral functions, for 4 different values of the parton's 3-momentum (p). Reprinted from [1].

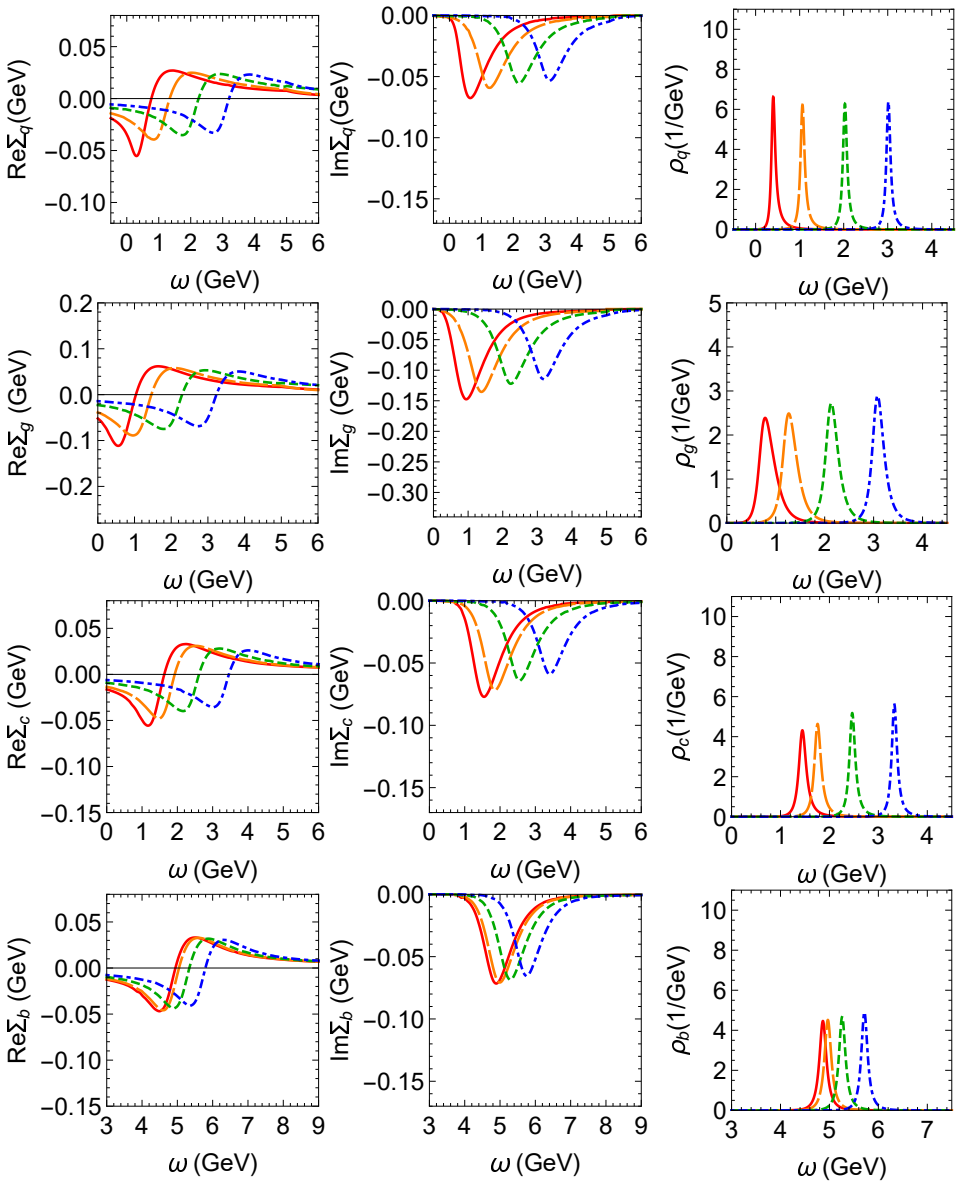

Figure 4.8: Same as Fig. 4.7 at T=0.258 GeV. Reprinted from [1].

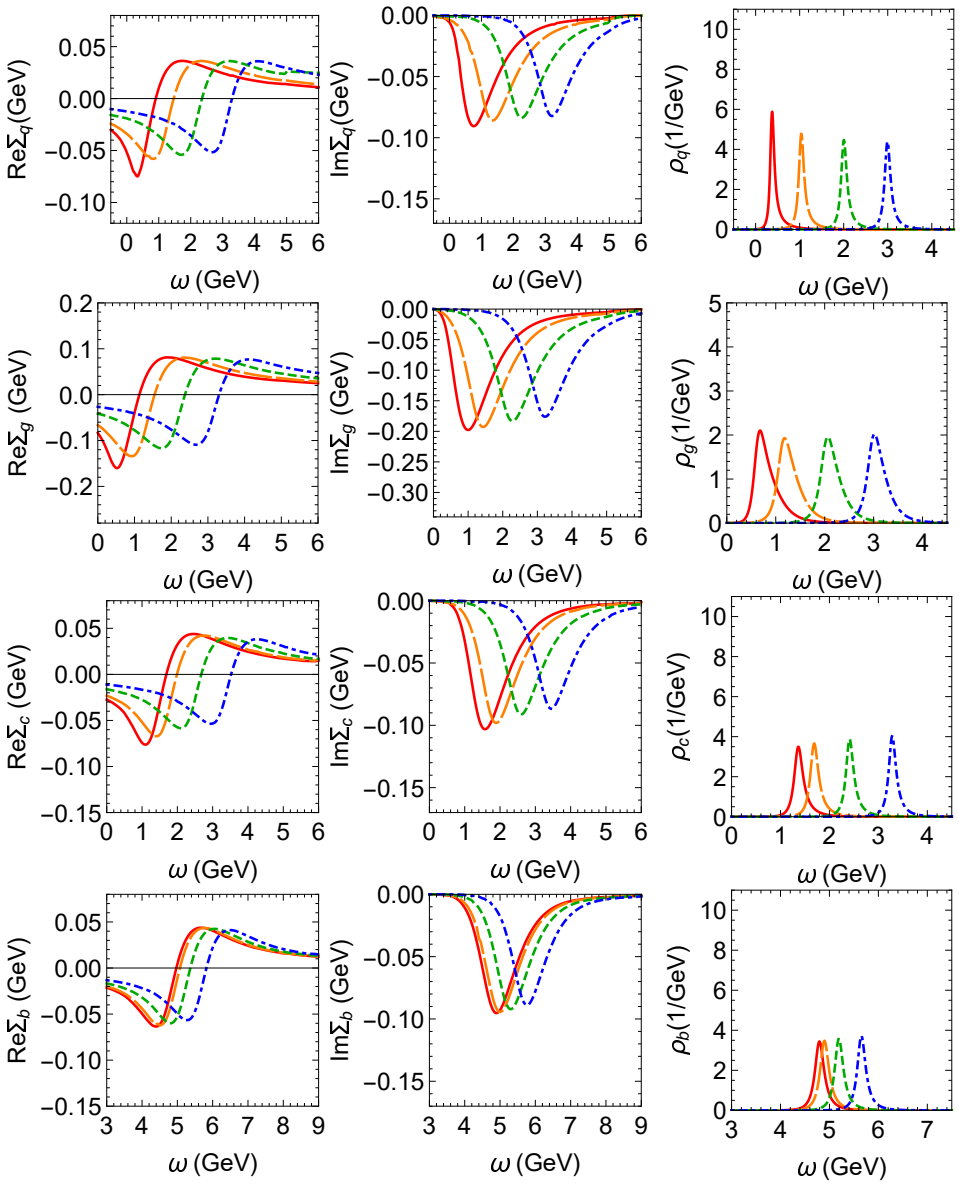

Figure 4.9: Same as Fig. 4.7 at T=0.320 GeV. Reprinted from [1].

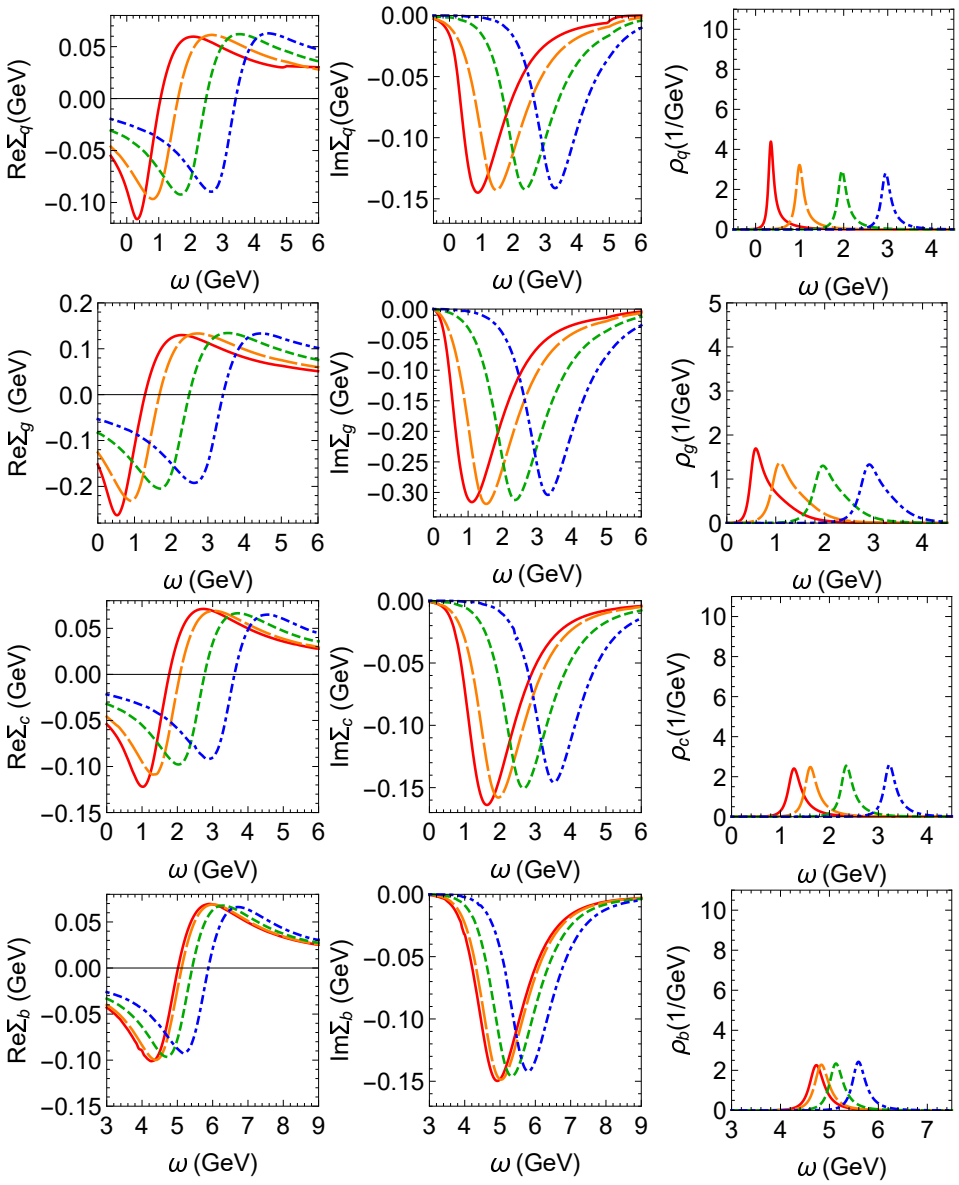

Figure 4.10: Same as Fig. 4.7 at T=0.400 GeV. Reprinted from [1].

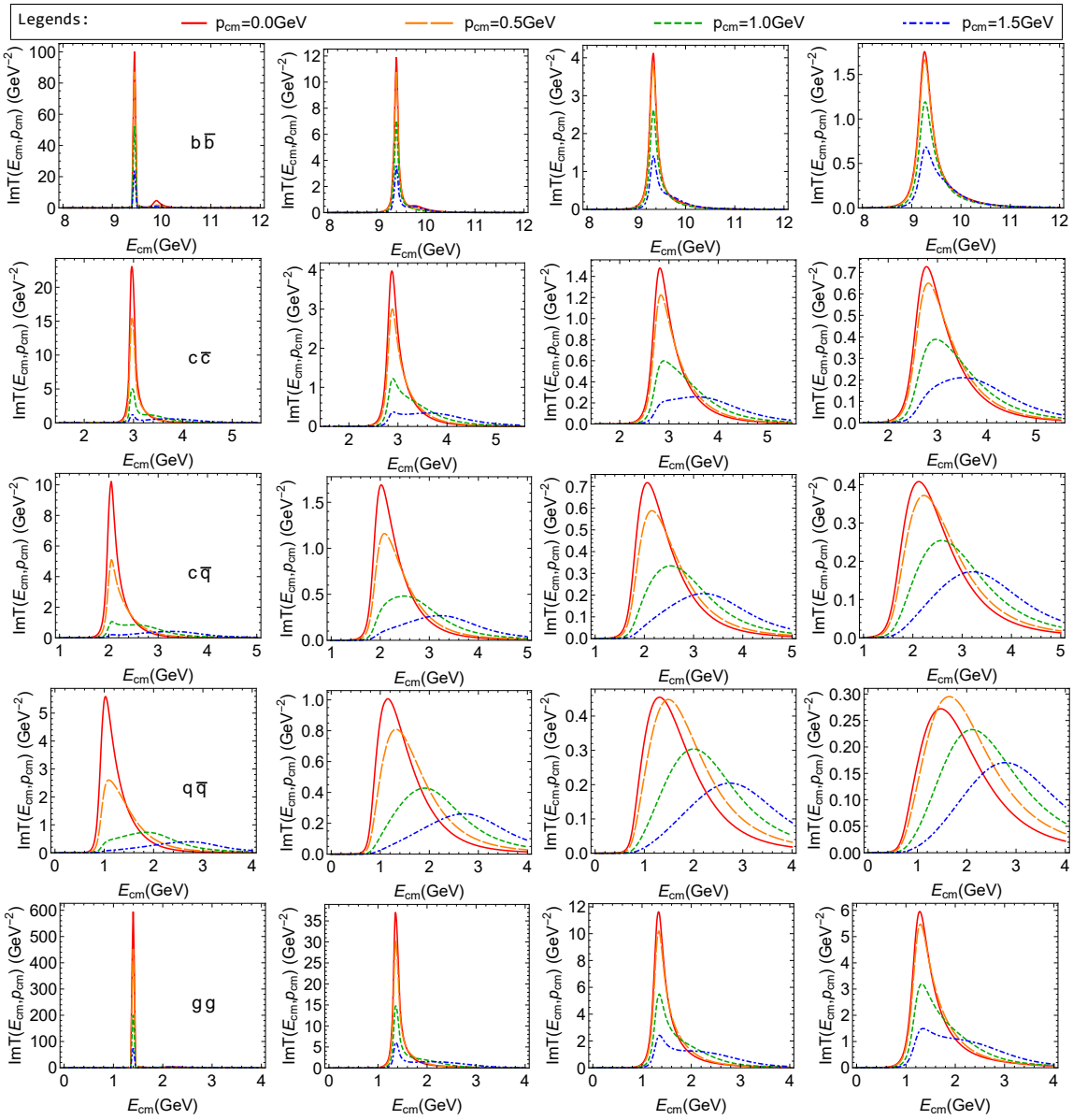

Figure 4.11: Weakly coupled solution for the imaginary part of the color-singlet S-wave T-matrices (without interference effects) in the bottomonium ($b\bar{b}$; first row), charmonium ($c\bar{c}$; second row), D-meson ($c\bar{q}$; third row), light-quark ($q\bar{q}$; fourth row), and glueball (gg, last row) channels. The 4 columns correspond to different temperatures, $T = 0.194$ GeV, $T = 0.258$ GeV, $T = 0.320$ GeV and $T = 0.400$ GeV from top down; in each panel, the T-matrix is displayed for 4 different values of the single-parton 3-momentum (p_{cm}) in the two-body CM frame. Reprinted from [1].

4.2 Strongly Coupled Solution

In this section we discuss our selfconsistent set of results for a strongly coupled solution (SCS). The section structure parallels the one of the WCS, namely starting from the determination of the underlying potential through fits of lQCD results for the static $Q\bar{Q}$ free energy (Sec. 4.2.1), followed by the quarkonium correlator analysis (Sec. 4.2.2), the fit to the QGP EoS (Sec. 4.2.3) and a discussion of the one- and two-body spectral properties (Sec. 4.2.4).

4.2.1 Free Energy, Potential and Static Selfenergies

When searching for a SCS within our framework, we start from a trial potential significantly larger than the free energy, together with large imaginary parts in the static-quark selfenergies. The converged selfconsistent parameters take the values $\alpha_s = 0.27$, $\sigma = 0.225\,\text{GeV}^2$, $c_b = 1.3$ and $c_s = 0.01$. The strong coupling constant and the "string-breaking" coefficient, c_b, are essentially the same as for the WCS, and the string tension

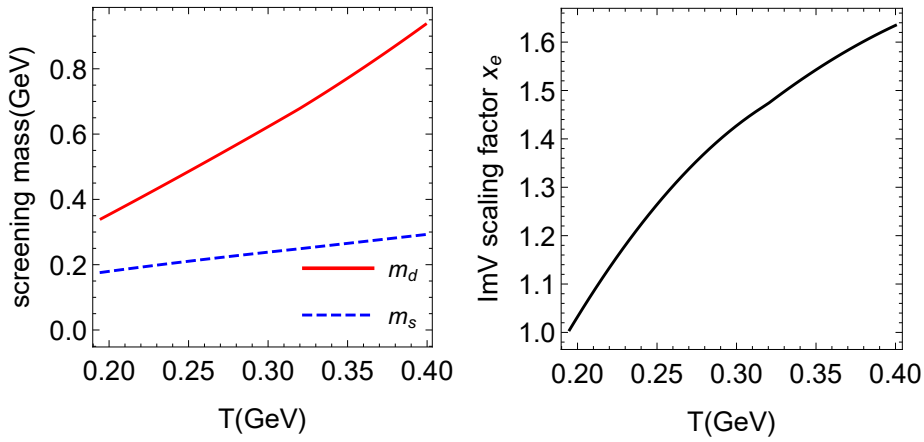

Figure 4.12: Results of a *strongly* coupled solution for the temperature dependence of the fitted screening masses (left panel) and the scale factor, x_e (right panel), figuring in the interference function. Reprinted from [1].

is only about $\sim$5% larger. The key difference lies in the coefficient, c_s, for the screening mass of the string term, which is a factor of $\sim$10 smaller. Consequently, the temperature dependent screening mass, $m_s = (c_s m_d^2 \sigma/\alpha_s)^{1/4}$, turns out to be smaller than in the WCS, mostly at low temperatures, by up to about 1/3, cf. left panel of Fig. 4.12. At the same time, the Coulomb Debye mass, m_d, for the SCS is comparable to the one in the WCS at low temperature, but increases more strongly (and essentially linear) with temperature. The key feature of the SCS in-medium potential is thus a rather long-range remnant of the confining force, as shown by the red lines in the third row of Fig. 4.13 and Fig. 4.14. In particular, at intermediate and large distances, the potential rises markedly over the free energy (green lines), by up to 0.6 GeV at the lowest temperature (T=0.194 GeV) and by up to 0.3 GeV at T=0.400 GeV. The latter is not far anymore from the WCS. The fit to the lQCD data (black dots) is of the same quality as for the WCS. The scale factor of the interference function shown in the right panel of Fig. 4.12 is also very similar to the WCS, although its magnitude is smaller at higher temperatures.

With the extracted potential, the selfenergies and spectral functions of the static quark generated from the static-light T-matrices are shown in the first two rows of Fig. 4.13 and Fig. 4.14. At low $T = 0.194$ GeV, the peak value of Im$\Sigma_Q \approx -0.26$ GeV implies a width of the spectral function in excess of 0.5 GeV. In fact, the full-width of half-maximum of the pertinent spectral function amounts to about 0.7 GeV, due to additional effects from the real part of the static-quark selfenergy. This is almost an order of magnitude larger than the leading order HTL result [106, 105, 112], $(\frac{4}{3}\alpha_s T) \approx 0.07$ GeV. In addition, the peak value of the single-quark width, -2ImΣ_Q, increases only slightly with T at lower temperatures, and even decreases between 0.320 and 0.400 GeV. This remarkable feature is due to the marked loss of long-range interaction strength which can over-compensate the increase in parton density with temperature. For the two-body quantities, the peak value of Im$\Sigma_{Q\bar{Q}}$ defined in Eqs. (3.34) and (3.40) is less than twice the peak value of ImΣ_Q, and the width

of the two-body spectral function is less than twice that of the single static-quark spectral function. This is different from the WCS case and caused by large off-shell effects.

Let us also comment on a comparison of the SCS to our previous work in Ref. [57]. The general shape and temperature behavior of the SCS potential are quite similar to the result with our previous fit ansatz [57]. However, the SCS potential shown in Fig. 4.13 has a significantly smaller force at large distances compared to the earlier result. Due to the increasing shell volume, $\propto r^2$, a long-range force interacts with increasingly more medium particles, which in principle can generate (very) large scattering widths. However, the selfconsistency requirement ties the width to the potential as the latter generates the selfenergies through the T-matrix. Large widths generated by long-distance forces can therefore easily lead to free energies which fall below the lQCD data. In this way, the selfconsistency much augments the control over the properties of the force which are especially effective in generating large widths (in particular its large-distance behavior).

We cannot prove that our SCS constitutes an upper limit for the coupling strength of the QGP, given the lQCD data that we incorporate in our fit. However, there are several limiting factors (in addition to the one described above) which prevent us from constructing more strongly coupled solutions. In particular, we limited ourselves to scenarios where the string tension does not significantly exceed the vacuum value. We also refrained from using “unnaturally" small Coulomb Debye masses which could provide a long-range force but would be in conflict with the expected approach toward perturbative behavior at high temperatures. Within these constraints the presented SCS is the “strongest" solution we could find upon varying our input and ansätze for the initial potential. As one would expect from a selfconsistent quantum framework, we have evidence that our calculations respect lower quantum bounds for transport coefficients, as has been conjectured, *e.g.*, for the ratio of shear viscosity to entropy density. For example, if we attempt to push for an extremely long-range force ansatz (which, as explained above, leads to very large scat-

tering widths), the selfconsistent iteration procedure in fitting the free energy will push back toward a more weakly coupled solution. When neglecting the requirements to agree with lQCD data and deliberately increasing the interaction strength in the calculation of the EoS, the selfconsistent T-matrix iteration ultimately leads to a zero-mass color-singlet glueball, which signals condensation and at that point goes beyond our current setup (recall that our parton fit masses encode possible condensate gaps). Quantum selfconsistency clearly plays a key role as a limiting mechanism.

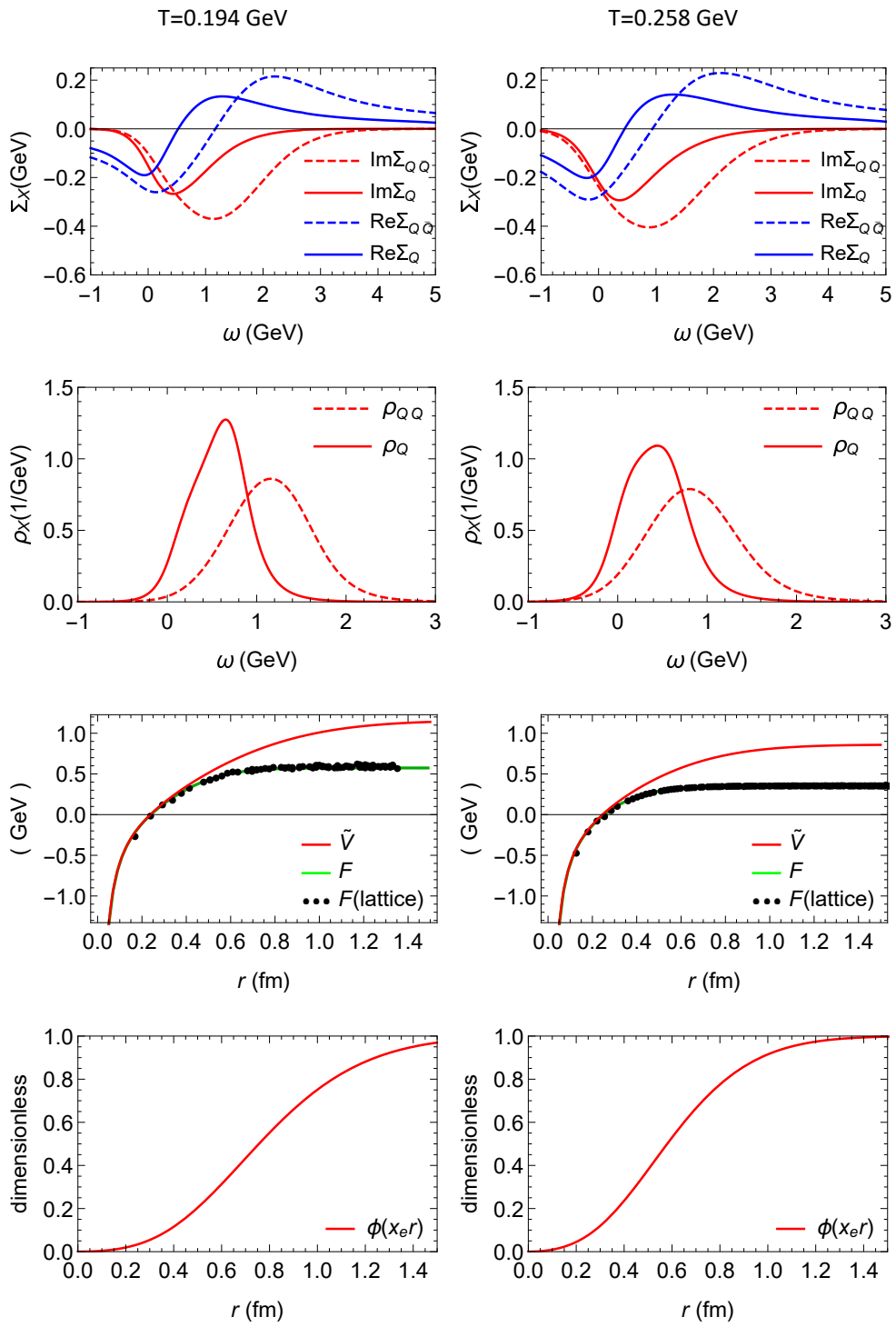

Figure 4.13: Results of a *strongly* coupled solution for the self-consistent fit to extract the static HQ potential: single-quark and $Q\bar{Q}$ selfenergies, $\Sigma_X(\omega,\infty)$ (first row), and spectral functions, $\rho_X(z,\infty)$ (second row), potential $\tilde{V}(r)$ and free energies (third row), and interference function, $\phi(x_e r)$ (fourth row). The free-energy lQCD data are from Ref. [2]. Reprinted from [1].

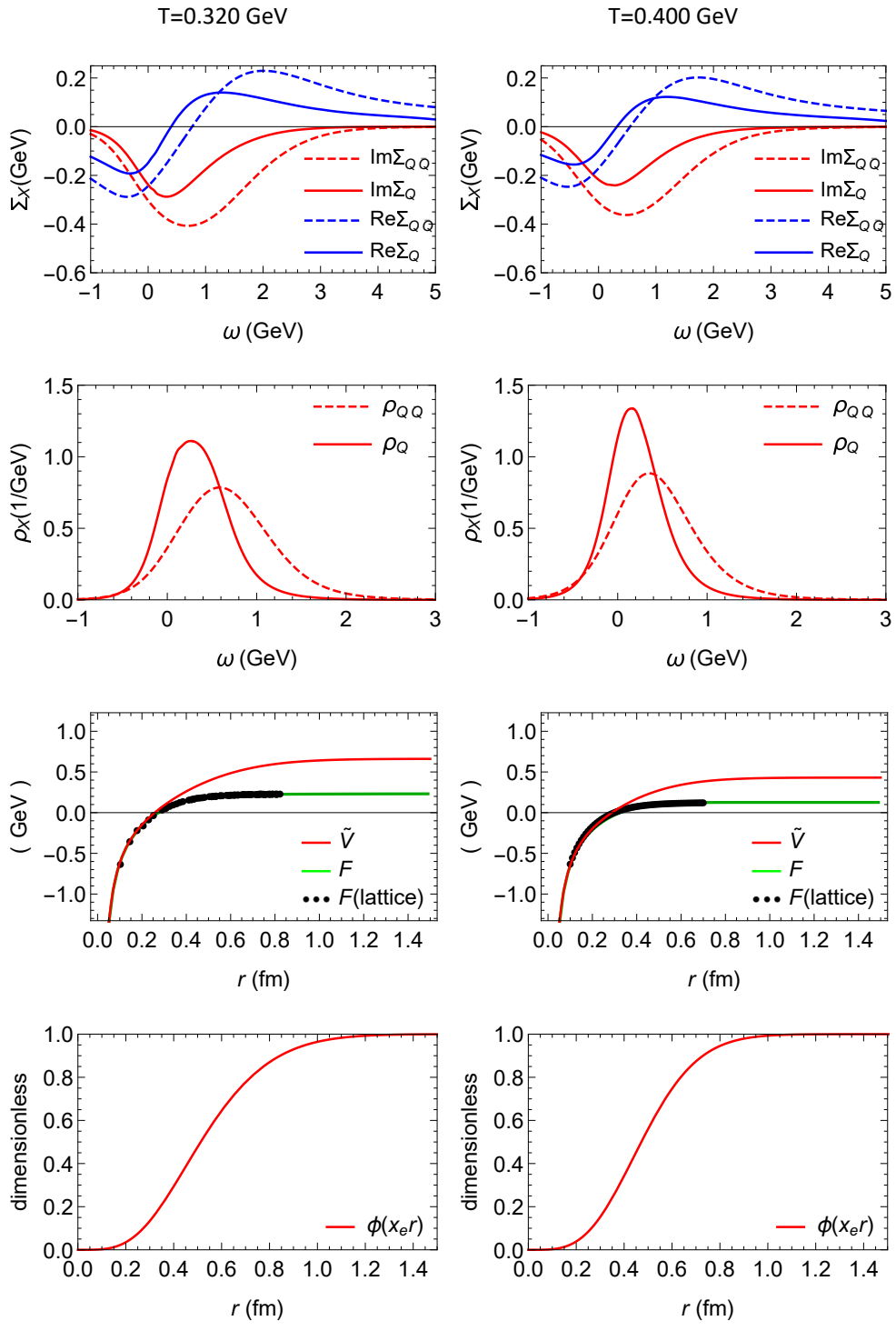

Figure 4.14: Same as Fig. 4.13 for two higher temperatures. Reprinted from [1].

4.2.2 Quarkonium Correlators and Spectral Function

The selfconsistent charmonium and bottomonium spectral functions and pertinent Euclidean correlators ratios (normalized to the lowest-temperature one) are collected in Fig. 4.15 and Fig. 4.16 together with lQCD data for the latter and the temperature dependence of the effective charm- and bottom-quark masses.

The large scattering rates of charm and bottom quarks in the SCS induce significantly larger widths of the quarkonium states than in the WCS. As before, interference effects lead to a marked reduction of the bound-state widths. The stronger binding compared to the WCS is counteracted by the significantly larger heavy-quark masses in medium as to generate an η_c mass that is remarkably stable with temperature. This leads to Euclidean correlator ratios which are within 2% of unity, which agrees even better with the lQCD data than in the WCS (although this is not necessarily significant, as we argued in the context of the WCS results). The correlator ratios without interference effects deviate somewhat more from the lQCD data, possibly indicating that a moderately broadened charmonium ground state that survives to higher temperatures (here about T=0.320 GeV when including interference) may be favored by lQCD data.[1] For example, the inelastic width of the η_c at T=0.194 GeV is around 0.1 GeV for the SCS and 0.02 GeV for the WCS (including interference). Appreciable charmonium reaction rates with the ground state surviving over an extended interval in temperature are favored by the phenomenology of transport models in describing J/ψ production at RHIC and the LHC [30], in particular to regenerate a sufficient number of J/ψ's at the LHC.

In the Υ sector, the first excited state still survives at the lowest temperature; even without interference effects, a pertinent maximum structure in the spectral function is visible

[1] There is a small overall shift of the ground states' peak position to higher masses when including interference effects as compared to neglecting them; this may depend on our specific implementation of the interference effects which requires further investigation. On the other hand, the reduction of the width by interference is a robust mechanism independent of the implementation.

below the nominal $b\bar{b}$ threshold of $2m_b$, but its width is comparable or even larger than the binding energy so that it appears as being dissolved. The ground-state $\Upsilon(1S)$ clearly survives up to the highest temperature, T=0.400 GeV (it is smeared out at much lower temperature without interference effects). The pertinent correlator ratio is in line with lQCD data within a few percent, which again is the closest agreement between all four scenarios considered in this work (SCS and WCS with and without interference effects). The slight increase of the calculated ratio is in part caused by the lowering of the bound-state mass, implying that the decrease in the constituent bottom-quark masses is more relevant than the decrease in binding energy.

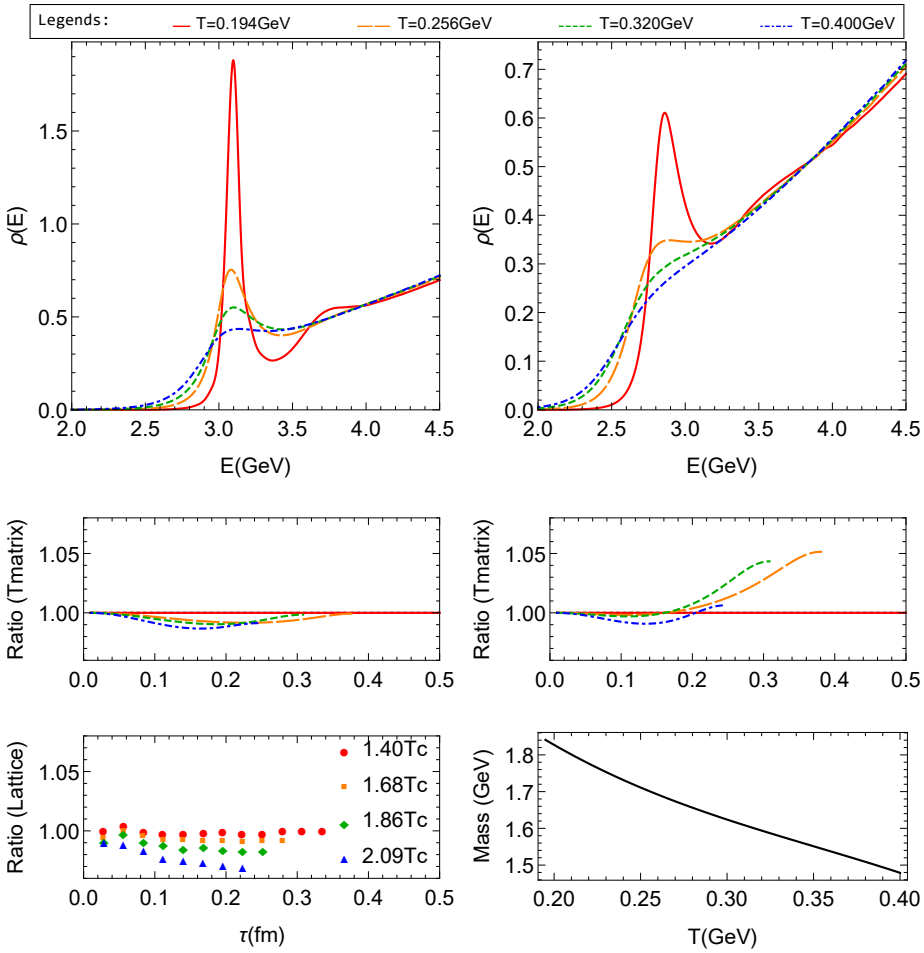

Figure 4.15: Strongly coupled solution for charmonium (η_c) spectral functions (upper panels) and correlators ratios (middle panels) with (first column) and without (second column) interference effects in the imaginary part of the potential. The lQCD data for η_c correlator [3] ratios are shown in the first bottom panel, respectively, while the second bottom panel display the temperature dependence of the charm-quark mass. Reprinted from [1].

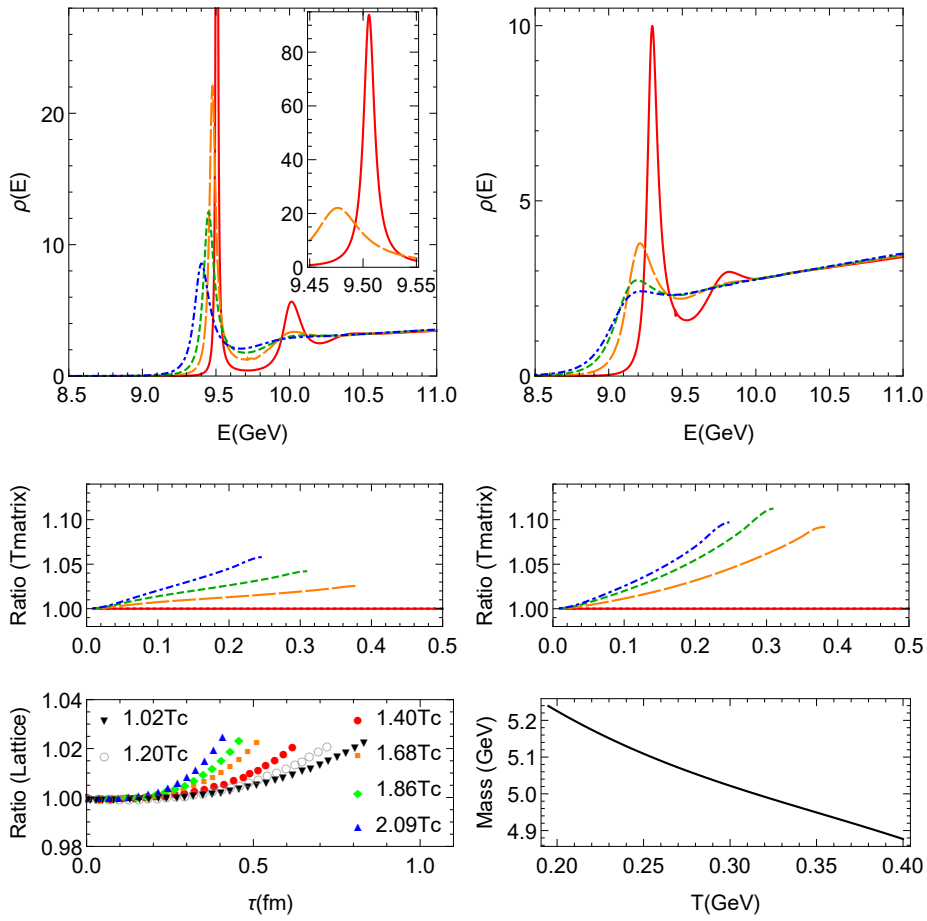

Figure 4.16: Same as Fig. 4.15 for bottomonium (η_b) with lQCD data [4]. Reprinted from [1].

4.2.3 QGP Equation of State

Next, we turn to the SCS for QGP bulk properties. The fitted light-parton masses are qualitatively similar to the WCS, cf. left panel of Fig. 4.17. Most notably, the gluon mass is quite a bit larger due to the larger string-induced Fock term contribution, recall Eq. (3.74), implying a much increased infinite-distance limit relative to the WCS. This contribution is also active for the effective quark mass. The underlying fit mass, $M_{\rm fit}$, is actually appreciably smaller than in the WCS, with values of 0.16 GeV and 0.49 GeV at

$T = 0.194\,\text{GeV}$ and $T = 0.400\,\text{GeV}$, respectively. These values are not far from what one expects from the perturbative (Coulomb) thermal masses, $\sqrt{1/3}gT = 0.2\,\text{GeV}$ and $\sqrt{1/3}gT = 0.42\,\text{GeV}$, respectively.

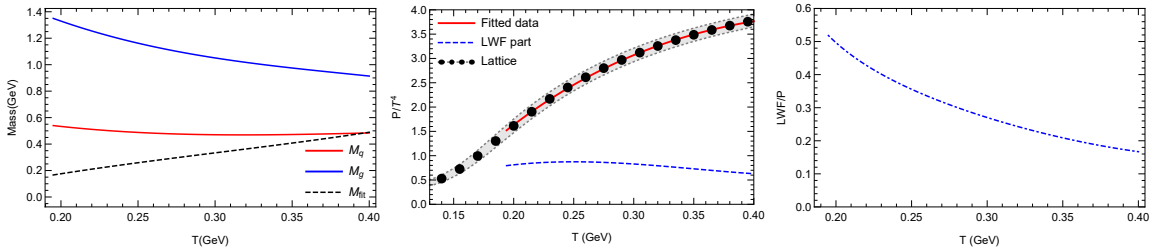

Figure 4.17: Strongly coupled solution for the QGP bulk medium: we show the fit results of the input masses for quarks and gluons (left panel), the resulting fit to the QGP pressure in comparison to lQCD data [5] (middle panel; solid line: total, dashed line: LWF contribution), and the ratio of LWF contribution to total pressure (right panel). Reprinted from [1].

The resulting EoS fits lQCD data well, and encodes the most important difference between SCS and WCS, namely that the two-body contribution to the pressure is much more prominent at low temperatures, reaching more than 50% at $T = 0.194$ GeV, compared to $\sim$10% in the WCS. Also, the LWF contribution shows a more intuitive temperature behavior, in that its fraction relative to the total appreciably decreases with increasing T (cf. right panel of Fig. 4.17); here, the decrease in interaction strength surpasses the increase in parton density, which can be interpreted as a gradual melting of the light-parton bound states with T (this interpretation will become even clearer upon inspection of the spectral functions in the next section). However, at T=0.400 GeV, the interaction contri-

bution still amounts to $\sim$20%, indicating that even at this temperature the QGP contains a significant nonperturbative component (possibly driven by the gluonic sector through glueball contributions). As before, the gluon sector largely decouples at small temperatures due to the large gluon masses.

4.2.4 Spectral Structure of QGP

We finally turn to the examination of the single-parton spectral functions (shown in Fig. 4.18, Fig. 4.19, Fig. 4.20, Fig. 4.21) and their in-medium scattering amplitudes in the SCS (shown in Fig. 4.22). The width of the partons, $\Gamma = -2\text{Im}\Sigma$, is large, especially at low temperatures and small 3-momenta, $p \lesssim T$, see the 4 plots in the second column of Fig. 4.18, Fig. 4.19. The quark (gluon) width reaches up to 0.6 (1.1) GeV right around its on-shell energy, which is larger than its effective mass and thus implies the loss of a well-defined quasiparticle excitation. Inspection of the pertinent $p = 0$ light-parton spectral functions (third column of Fig. 4.18 and Fig. 4.19) confirms this notion, as the quark's (gluon's) spectral strength is spread over an energy range of about 1(2) GeV. In fact, the rather large and attractive real part of the selfenergy at small (off-shell) energies (first column of Fig. 4.18 and Fig. 4.19) also plays an important part in the quark (gluon) spectral distribution, as it generates a rather prominent collective mode at $\omega \simeq 0.15(0.7)$ GeV, sitting on top of the broad distribution associated with the dissolved quasiparticle mode. The low-temperature widths are almost an order of magnitude larger than the HTL value of $\frac{4}{3}\alpha_s T \approx 0.07$ GeV, and much larger than the most recent dynamical quasiparticle model result which is around 0.2 GeV [118]. Interestingly, the temperature dependence of the parton widths is non-monotonic with increasing temperature (as was found for static quarks discussed in Sec. 4.2.1), which has important consequences for the temperature dependence of transport coefficients [77]. This is qualitatively different from both perturbative and dynamical quasiparticle approaches. The 3-momentum dependence of the width

is quite strong especially at low temperatures (less so at high temperature), being substantially reduced with increasing p. This implies that at higher momenta well-defined quasiparticle excitations re-emerge at any temperature, as to be expected from a generic transition to a weak coupling. However, since the string term at high temperature is not screened as much as in the WCS, the momentum dependence of selfenergy at high temperature differs from the WCS. The widths of the charm and bottom quarks are quite similar to the light quarks, implying that bottom quarks remain well-defined quasiparticles at all momenta and temperatures, while the situation is borderline for low-momentum charm quarks close to T_c.

Selfconsistent T-matrices are compiled in Fig. 4.22. At low temperatures appreciably bound quark-antiquark states emerge in all channels (glueballs, light mesons, heavy-light mesons, charmonia and bottomonia). The light $q\bar{q}$ resonance mass is close to the vacuum mass of light vector mesons, reflecting a realistic vacuum limit as encoded in the potential model (instanton effects are subleading in the vector channel). This is, however, nontrivial given its embedding in the QGP EoS (in particular through the fitted light-quark mass). Note that the off-shell behavior of the parton widths, *i.e.*, their decrease away from the on-shell peak (recall 2. column in Fig. 4.18), plays an important role in the formation of bound states; *e.g.*, the light-meson width of $\sim$0.6 GeV at the lowest temperature is well below twice the light-quark width, mostly because of the $\sim$0.3 GeV binding relative to the nominal $q\bar{q}$ threshold of 1.1 GeV. Compared to the WCS (recall Fig. 4.11), the strength of the T-matrices in the SCS is much increased (*e.g.*, the peak value in the $p_{\rm cm}$=0 light-meson channel is $\sim$25/GeV^2 in the latter compared to $\sim$6 /GeV^2 in the former; also, the mass of the $q\bar{q}$ bound state is smaller, $\sim$0.8 GeV vs. $\sim$1 GeV). This, in particular, makes a large difference in their contributions to the EoS (recall Fig. 4.17 vs. Fig. 4.6). At the same time, the much larger widths in the spectral functions of light partons in the SCS relative to the WCS causes their thermodynamic weight to be much suppressed in the former relative to

the latter. In this sense, the SCS predicts a transition from broad parton quasiparticles to broad hadronic states in the thermodynamics of the QGP as T_c is approached from above. The re-emergence of parton quasiparticles and suppression of their bound states not only occurs with increasing temperature (note the reduction in the y-axis scale when going down in temperature column by column in Fig. 4.22), but also with increasing parton CM momentum within the bound-state (not to be confused with the total momentum, P, of the bound state in the heat bath, which is zero throughout this work) and delayed with increasing constituent parton mass.

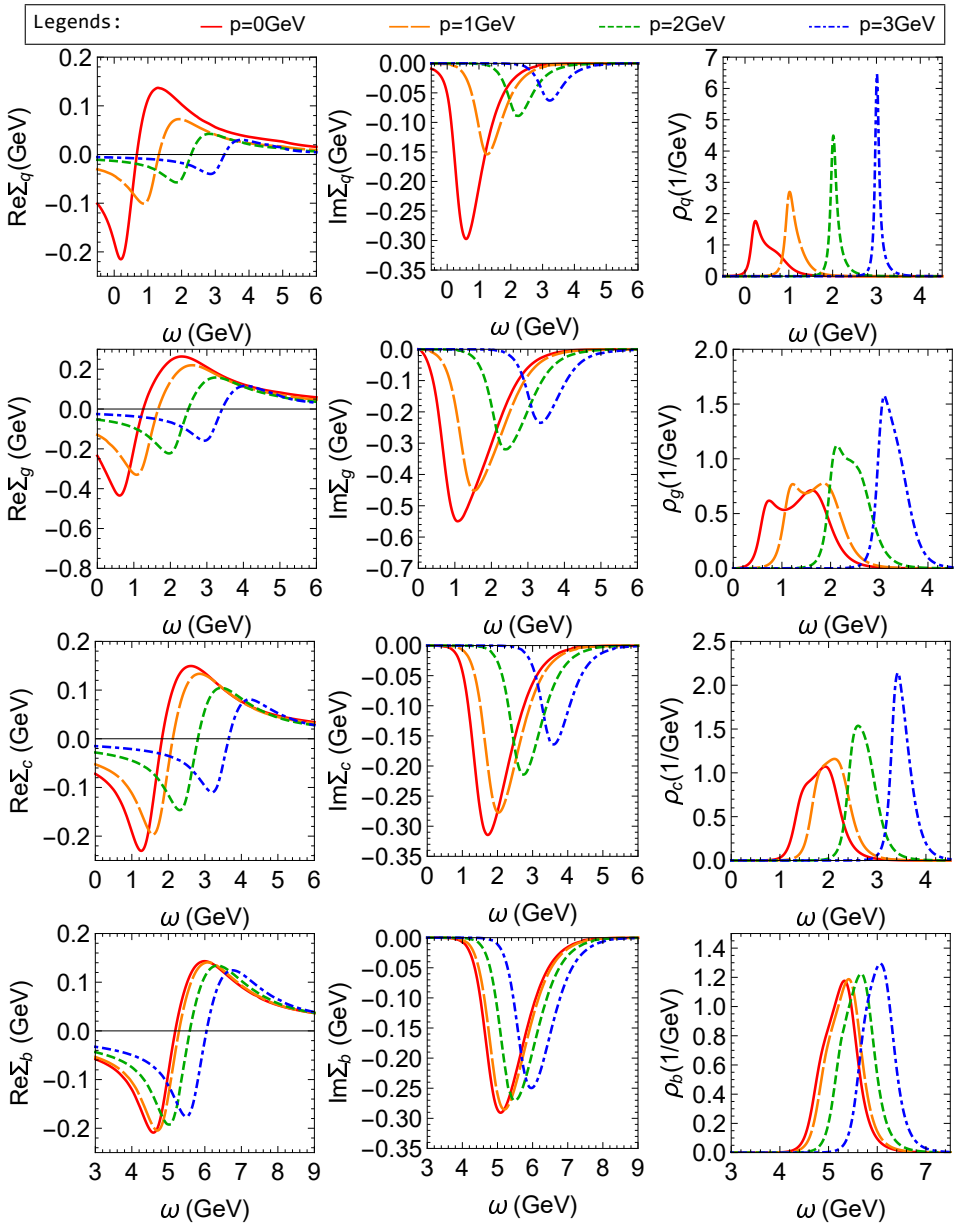

Figure 4.18: Strongly coupled solution for parton spectral properties of the QGP at T=0.194 GeV. 4 rows corresponding to different parton species (light quarks (q), gluons (g), charm quarks (c) and bottom quarks (b) in the first, second, third and fourth row of each panel, respectively). Each row contains 3 panels showing (from left to right) the energy dependence of the pertinent real and imaginary part of the selfenergy and the resulting spectral functions, for 4 different values of the parton's 3-momentum (p). Reprinted from [1].

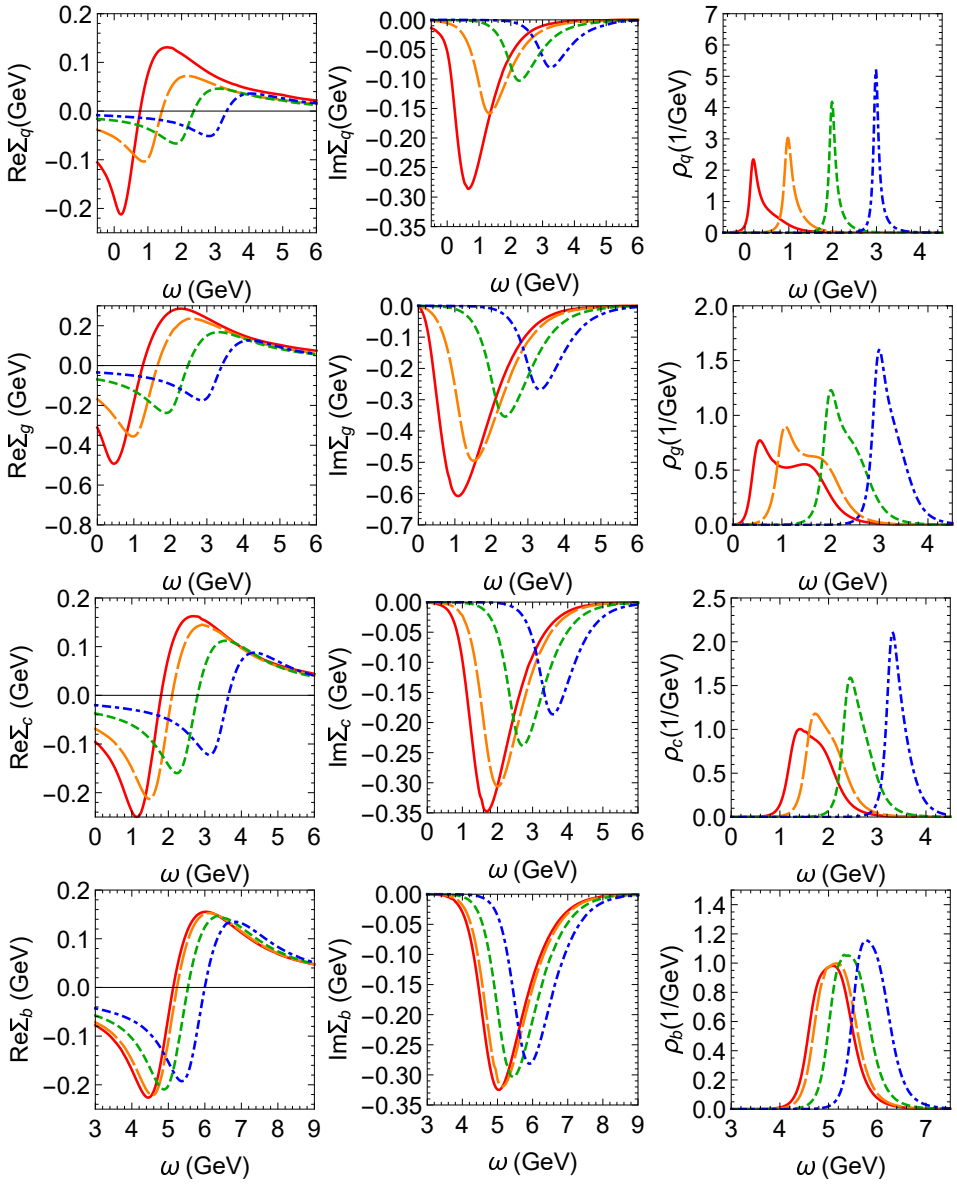

Figure 4.19: Same as Fig. 4.18 at T=0.258 GeV. Reprinted from [1].

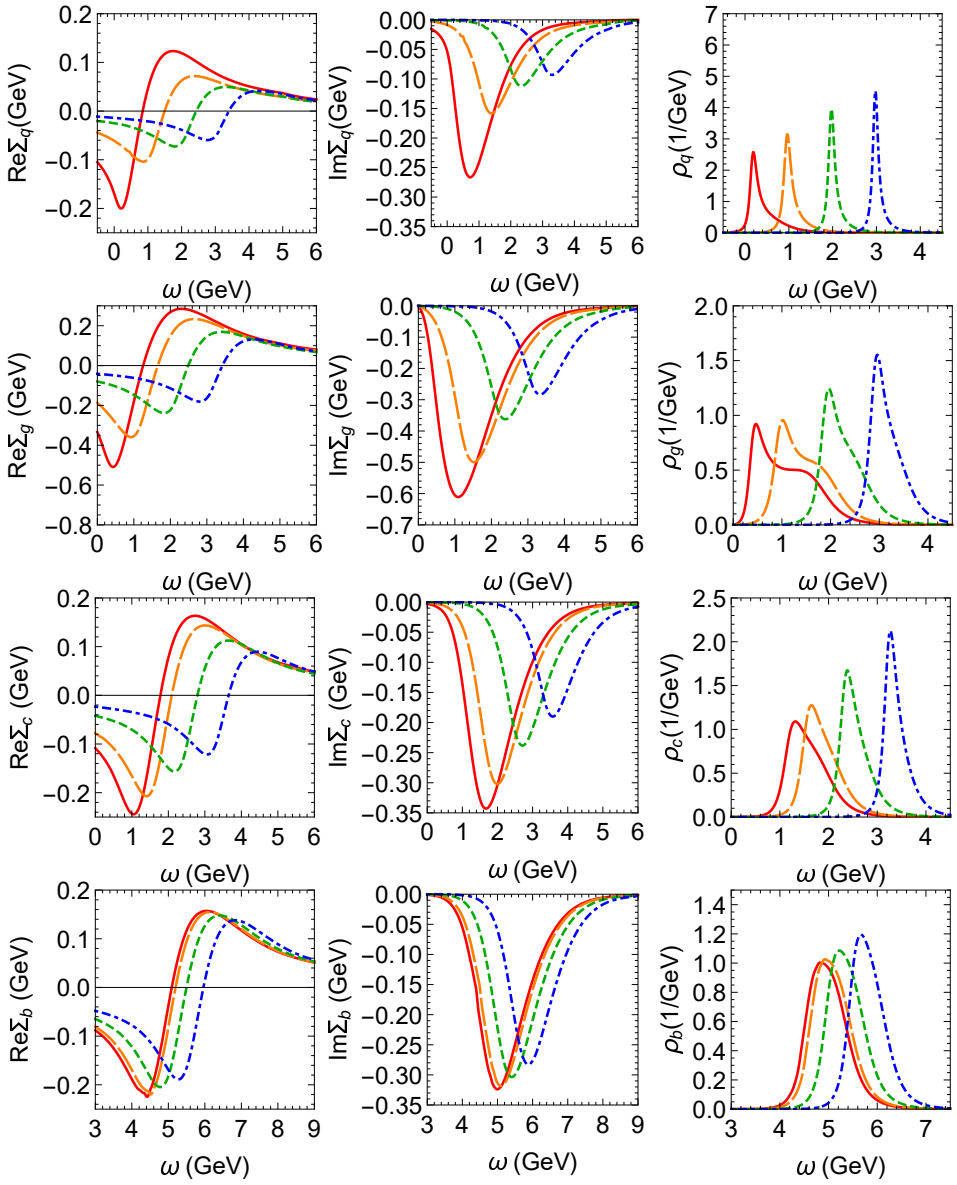

Figure 4.20: Same as Fig. 4.18 at T=0.320 GeV. Reprinted from [1].

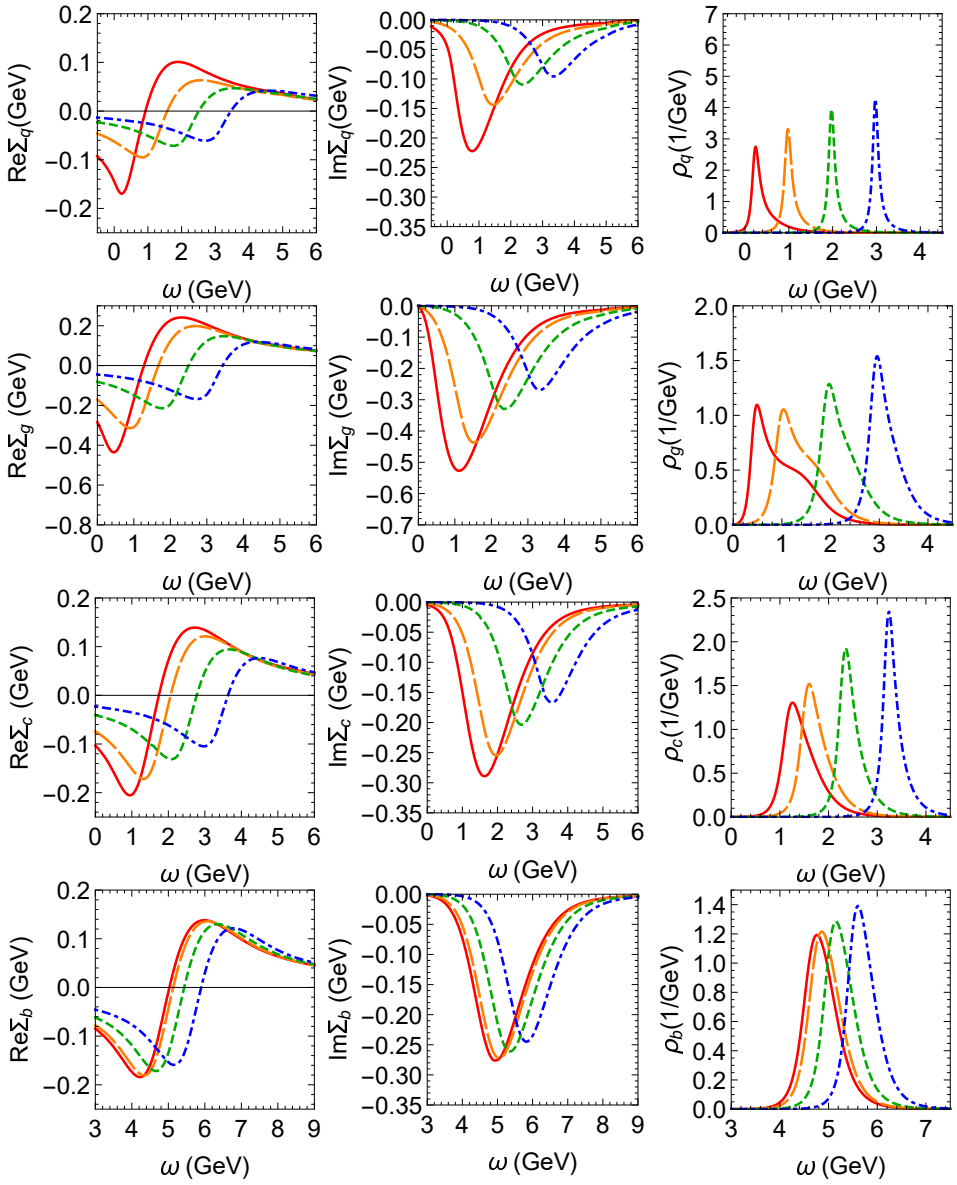

Figure 4.21: Same as Fig. 4.18 at T=0.400 GeV. Reprinted from [1].

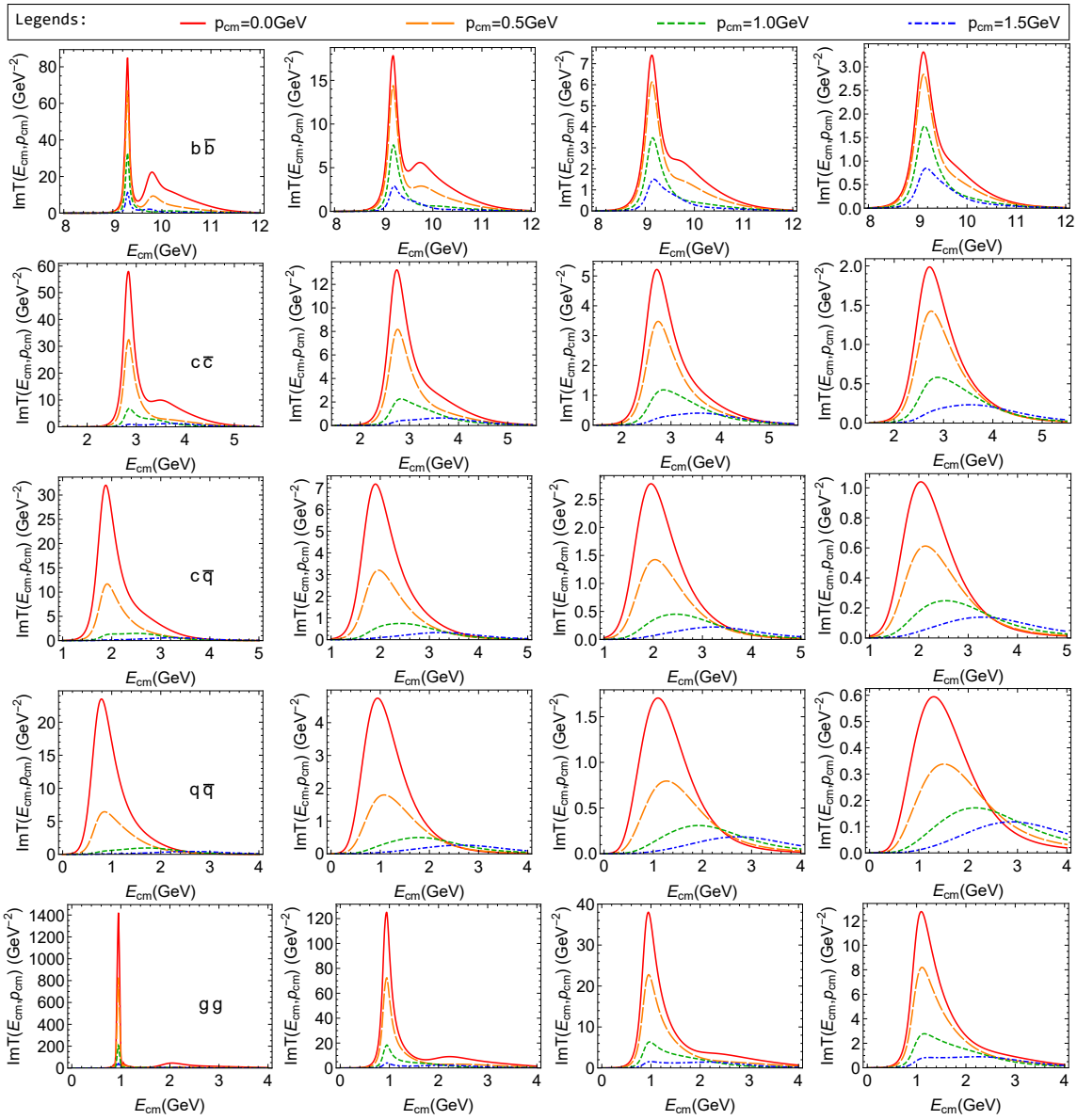

Figure 4.22: Strongly coupled solution for the imaginary part of the color-singlet S-wave T-matrices (without interference effects) in the bottomonium ($b\bar{b}$; first row), charmonium ($c\bar{c}$; second row), D-meson ($c\bar{q}$; third row), light-quark ($q\bar{q}$; fourth row), and glueball (gg, last row) channels. The 4 columns correspond to different temperatures, $T = 0.194$ GeV, $T = 0.258$ GeV, $T = 0.320$ GeV and $T = 0.400$ GeV from top down; in each panel, the T-matrix is displayed for 4 different single-parton momenta ($p_{\rm cm}$) in the two-body CM frame. Reprinted from [1].

5. TRANSPORT PROPERTIES OF THE QGP*

5.1 Introduction

In previous chapters, using a unified T-matrix approach for the bulk and microscopic properties of the QGP and its excitations, we have found multiple solutions, characterized by different potentials, that are consistent with the three sets of lattice data. The existence of multiple solutions may indicate information loss when calculating in imaginary time, leading us to seek additional constraints from other sources. In particular, HQ transport approaches [113, 52, 6, 119] demonstrate that the heavy-meson spectra, nuclear modification factor R_{AA} and elliptic flow v_2, are quantitatively sensitive to the HQ transport coefficients (relaxation rates)—which are governed by the strength of the underlying color interactions. Also, hydrodynamic studies [40, 41] provide information on the viscosity of the QGP. Therefore, calculating transport coefficients and using them in comparison to either experimental data or phenomenological results may help us to better determine the microscopic structure of the QGP.

Along these lines, several pioneering works [68, 70] include calculations of the HQ transport coefficients using the HQ free energy F and internal energy U for the potential kernel. However, both F and U are not the self-consistent solutions discussed in the previous chapter. Therefore, in this chapter we mainly focus on the transport properties predicted by two self-consistent solutions—SCS and WCS. Since the width of the partons' spectral functions in the SCS are large, the HQ transport coefficients are evaluated in an off-shell scheme based on the Kadanoff-Baym equations [73]; these equations are derived using the non-equilibrium Green functions [120], which go beyond the T-matrix

*Part of section 5.4 is reprinted with permission from "Non-perturbative approach to equation of state and collective Modes of the QGP" by Shuai Y. F. Liu and Ralf Rapp, 2018, EPJ Web Conf. **172**, 05001, Copyright 2018 by EDP Sciences.

approach [67, 68, 70] using the conventional on-shell approximation. The viscosity is evaluated using a Kubo formula, which also fully accounts for off-shell effects. Also, we will briefly discuss an improvement to the partial-wave summation used in previous works [67, 68, 70].

This Chapter is organized as follows. In section 5.2, we recollect several features and differences of the WCS and SCS. In section 5.3.1, we introduce the off-shell formalism to calculate HQ transport coefficients, including a correction to a formula used in previous works [67, 68, 70]. In section 5.3.2, we analyze the features of HQ transport coefficients that are calculated using these two types of potentials. In section 5.3.3, we discuss the implementation of these transport coefficients in Langevin simulations to obtain the results for heavy flavor R_{AA} and v_2 observables for these potentials and the implications for discriminating them.

5.2 In-Medium Potentials Based on Lattice QCD

In addition to the potentials of the SCS and WCS, the thermal quantities F and U have been used as potentials to study a large variety of physics, such as transport coefficients [67, 68, 69], quarkonium physics [60], and even light parton properties [66]. These potentials are compared in Fig 5.1; we plot $\tilde{V}_s$ ($\tilde{V}$ of SCS), $\tilde{V}_w$ ($\tilde{V}$ of WCS), internal energy U, and free energy F. The $\tilde{V}_w$ and $\tilde{V}_s$ both lie between U and F, and both potentials tend to be closer to U as temperature increases. The $\tilde{V}_w$ is close to F, especially at low temperature. However, at high temperature, it is significantly larger than the free energy. On the other hand, the $\tilde{V}_s$ is close to U except at $T = 0.194\,\text{GeV}$, where it is approximately in the middle. The $\tilde{V}_s$ is much higher than the $\tilde{V}_w$ at large distance, but they are close to each other at short distance. Also, the gap between $\tilde{V}_s$ and $\tilde{V}_w$ gets smaller as temperature increases.

Taking the derivative of the "potentials", $-dV(r)/dr$, yields the forces. These forces

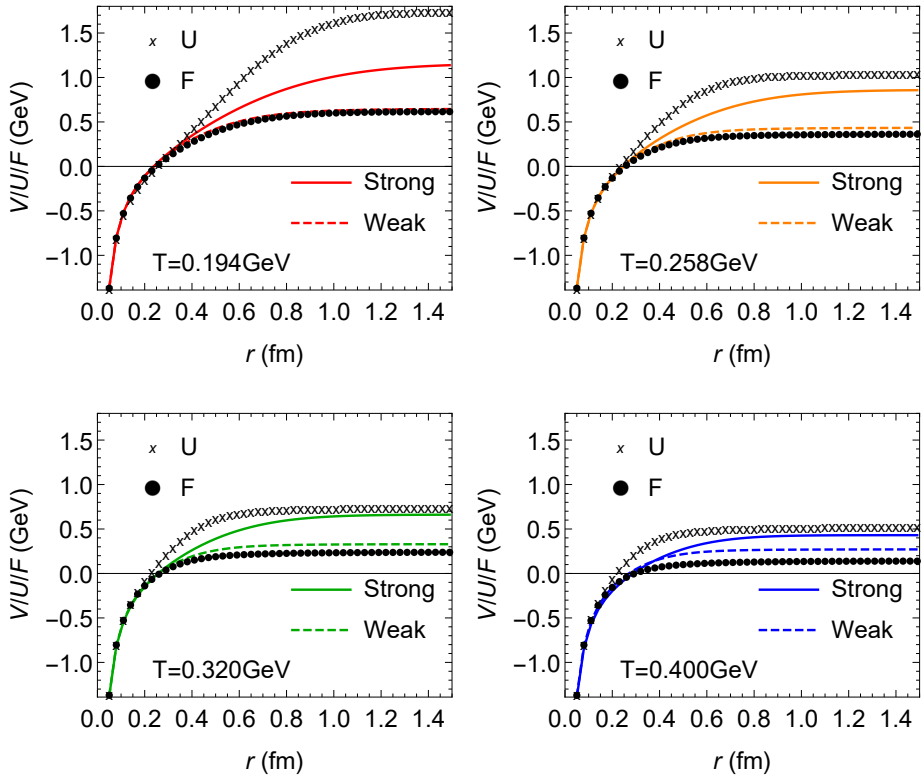

Figure 5.1: The potential of the SCS (solid lines), of the WCS (dashed lines), the internal energy U (crosses) and free energy F (dots) for four temperatures.

are compared in Fig. 5.2 (left). The force for the SCS at large distances is much higher than that for the WCS. At $T = 0.194$ GeV, the force for the SCS is around 0.5 GeV/fm at 1 fm, approximately half of the vacuum string force; at the same distance the force for the WCS is approximately 0.1 GeV/fm. This remnant of the string force is the key difference between the WCS and the SCS, especially since many physical quantities are proportional to r^2, such as the number of particles in the unit volume of a spherical shell. Multiplying the force by $\frac{3}{4}r^2$, the dimensionless quantity $\frac{3}{4}r^2 dV/dr$ can be regarded as an"effective coupling" [1] and is plotted for both the SCS and the WCS in Fig. 5.2 (right). (The factor of 3/4 is included to reach the coupling constant at a short distance.) Again, the WCS and

[1]Due to different origins of the Coulomb and confining terms (different relativistic and color structure), we should be careful about the concept of "effective coupling".

SCS are similar at short distances, but the SCS gives a significantly stronger "coupling" at large distances. The SCS reaches a peak of approximately 2 at $r \approx 0.8\,\text{fm}$. This infrared enhancement is due to a remnant of the confining force—as mentioned earlier.

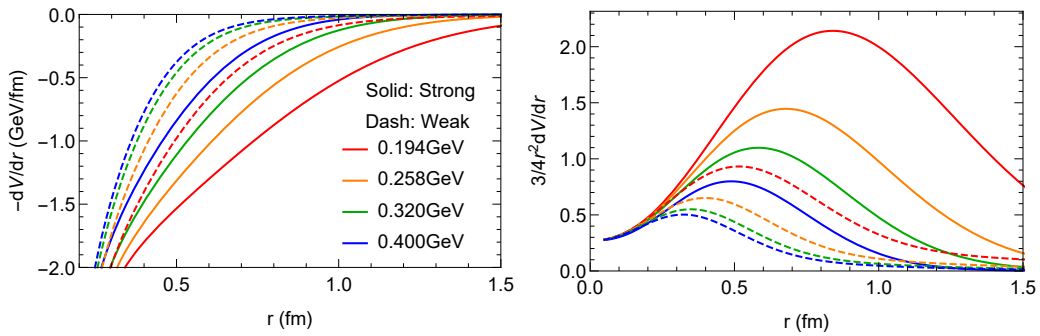

Figure 5.2: In-medium forces $-dV/dr$ (left) and $\frac{3}{4}r^2 dV/dr$ (right) for the SCS (solid lines) and the WCS (dashed lines) for different temperatures (different colors).

.

5.3 Heavy-Quark Transport

5.3.1 Off-Shell Transport Coefficients

Since the partons' spectral functions in the SCS have large widths, as shown in Chapter 4, it is desirable that the Boltzmann and Langevin equations incorporate these large off-shell quantum effects. To realize this goal, we start from the Kadanoff-Baym equations, then use a minimal set of approximations to reduce them to a Boltzmann equation, where quantum effects are encoded in the transition rates. Subsequently, this Boltzmann equation is expanded into a Fokker-Planck equation, which can be converted to Langevin dynamics—wherein quantum effects are encoded in the transport coefficients.

In this paper, we closely follow the formalism for non-equilibrium quantum field theory described in Ref. [120]. For illustrative purposes, we first provide a formal derivation of the relations for the non-relativistic case. However, our final formula for the transport

coefficients account for relativistic effects as discussed in previous chapters. In relative energy-momentum space, with a macroscopic time denoted as t,[2] the equation for the non-equilibrium HQ Green functions, Eq. (4.1), can be expressed as[3]

$$\frac{\partial}{\partial t}[\int d\omega G_Q^<(\omega,\mathbf{p},t)] = \int d\omega\{i\Sigma_Q^<(\omega,\mathbf{p},t)G_Q^>(\omega,\mathbf{p},t) - i\Sigma_Q^>(\omega,\mathbf{p},t))G_Q^<(\omega,\mathbf{p},t)\}. \tag{5.1}$$

The $G_Q^{<,>}(\omega,\mathbf{p},t)$ are the Fourier transforms of the Green functions,

$$G_Q^<(t_2,x_2,t_1,x_1) = i\langle\psi_Q^\dagger(t_2,x_2)\psi_Q(t_1,x_1)\rangle \tag{5.2}$$

$$G_Q^>(t_2,x_2,t_1,x_1) = -i\langle\psi_Q(t_1,x_1)\psi_Q^\dagger(t_2,x_2)\rangle, \tag{5.3}$$

where $\delta t = t_1 - t_2$, $\delta x = x_1 - x_2$, $t = (t_1+t_2)/2$, $x = (x_1+x_2)/2$ are defined by the Wigner transformation. A uniform medium is assumed, so that the $G_Q^{<,>}$ do not depend on x. $\Sigma_Q^{<,>}$ is the selfenergy in the real-time formalism, in which it can be calculated diagrammatically from the underlying scattering processes between the heavy quark and the partons in medium. The Fourier transform of $\Sigma_Q^{<,>}$ uses the same convention as that for $G_Q^{<,>}$. The T-matrix approach is used to derive the expressions for these selfenergies in Ref. [120], Appendix F. For $\Sigma_Q^>$, the expression is

$$\Sigma_Q^>(\omega,\mathbf{p},t) = \mp\sum\int\frac{d\nu d^3\mathbf{q}}{(2\pi)^4}\frac{d\nu' d^3\mathbf{q}'}{(2\pi)^4}\frac{d\omega' d^3\mathbf{p}'}{(2\pi)^4}(2\pi)^4\delta^{(4)} |T(E,\mathbf{P},\mathbf{p},\mathbf{p}')|^2 G_Q^>(\omega',p')G_i^<(\nu,q)G_i^>(\nu',q'), \tag{5.4}$$

[2]Use the same approximation $T \pm t/2 \approx T$ as in Ref. [120], but use t to denote $T = (t_1+t_2)/2$.

[3]For our purpose, translation invariance is enforced—all terms with a gradient of coordinates vanish, so that the Boltzmann equation used to evaluate the transport coefficients can be derived as in Ref. [48].

and for $\Sigma_Q^<$ the expression is

$$\Sigma_Q^<(\omega,\mathbf{p},t) = \mp \sum \int \frac{d\nu d^3\mathbf{q}}{(2\pi)^4}\frac{d\nu' d^3\mathbf{q}'}{(2\pi)^4}\frac{d\omega' d^3\mathbf{p}'}{(2\pi)^4}(2\pi)^4\delta^{(4)} \\ |T(E,\mathbf{P},\mathbf{p},\mathbf{p}')|^2 G_Q^<(\omega',p',t)G_i^>(\nu,q)G_i^<(\nu',q'). \tag{5.5}$$

Here, $\delta^{(4)}$ is shorthand for off-shell energy-momentum conservation, and $\sum$ represents the summation over internal degrees of freedom, such as color, spin, flavor (divided by one HQ degeneracy $d_Q = 6$). $\mathbf{P}$ and E are the total momentum and energy. $T(E,\mathbf{P},\mathbf{p},\mathbf{p}')$ is the retarded T-matrix. The $G_i^{<,>}$ are the Green functions for the light partons in medium. The classical Boltzmann equation is recovered from Eq. (5.1) using the on-shell approximations: $G_x^< = \mp i(2\pi)\delta(\omega - \varepsilon_x(\mathbf{p}))f_x(\mathbf{p},t))$, and $G_x^> = -i(2\pi)\delta(\omega-\varepsilon_x(\mathbf{p}))(1\pm f_x(\mathbf{p},t))$, where $x = Q$ or i including the G's in the expressions for $\Sigma_Q^>$ and $\Sigma_Q^<$ implicitly. These approximations are derived in Ref. [120].[4] However, these approximations neglect off-shell quantum effects. For describing HQ diffusion in a local-equilibrium QGP, not all these approximations are necessary. We have found that the minimal (quasiparticle) approximations required for obtaining a HQ Boltzmann equation are

$$G_Q^<(\mathbf{p},\omega,t) = \mp i\delta(\omega - \varepsilon_Q(\mathbf{p}))f_Q(\mathbf{p},t), G_Q^>(\omega,p) = -i(2\pi)\rho_Q(\omega,p)(1-n_Q(\omega)), \tag{5.6}$$

$$G_i^<(\omega,p) = \mp i(2\pi)\rho_i(\omega,p)n_i(\omega), \qquad G_i^>(\omega,p) = -i(2\pi)\rho_i(\omega,p)(1\pm n_i(\omega)), \tag{5.7}$$

where the quasiparticle approximation is only applied to $G_Q^<(\omega,\mathbf{p},t)$, and all of the other $G^{<,>}$ are taken to be off-shell equilibrium Green functions—in which $\rho_{i,Q}$ and $n_{i,Q}$ are the spectral and distribution functions, respectively, for {light, heavy} partons in equilibrium. Substituting these functions into Eqs. (5.1), (5.4), and (5.5), results in the Boltzmann

[4] Our convention for "$\mp$" (upper/lower denotes boson/fermion) is opposite of that in Ref. [120].

equation

$$\frac{\partial}{\partial t} f(\mathbf{p},t) = \int \frac{d^3\mathbf{k}}{(2\pi)^3} [w(\mathbf{p+k},\mathbf{k}) f(\mathbf{p+k},t) - w(\mathbf{p},\mathbf{k}) f(\mathbf{p},t)], \tag{5.8}$$

where the rate $w(\mathbf{p+k},\mathbf{k})$ is[5]

$$w(\mathbf{p},\mathbf{k}) = \int \frac{d\nu d^3\mathbf{q}}{(2\pi)^3} \frac{d\nu' d^3\mathbf{q}'}{(2\pi)^3} d\omega' (2\pi)^4 \delta^{(4)} |T(E,\mathbf{P},\mathbf{p},\mathbf{k}-\mathbf{p})|^2$$
$$\rho_Q(\omega', |\mathbf{k}-\mathbf{p}|) \rho_i(\nu,q) \rho_i(\nu',q') n_i(\nu) (1 \mp n_i(\nu')) (1 \mp n_Q(\omega')), \tag{5.9}$$

and $\mathbf{k} = \mathbf{p}' - \mathbf{p}$ is the momentum exchange. Since we use equilibrium T-matrices, spectral and distribution functions, the rate $w(\mathbf{p},\mathbf{k})$ does not depends on the dynamical non-equilibrium distribution function $f(\mathbf{p},t)$. So far, our discussion does not include relativistic effects; several modifications are necessary for a relativistic treatment of the problem—as detailed in the following calculation of the HQ transport coefficients.

Expanding the full Boltzmann equation with momentum transfer $\mathbf{k}$ results in the Fokker-Planck equation, which can be converted to a Langevin approach for heavy quarks. This approach provides a direct connection between HQ transport coefficients and the observed heavy-meson spectra. The Fokker-Planck equation is expressed as

$$\frac{\partial}{\partial t} f(p,t) = \frac{\partial}{\partial p_i} \{ A_i(p) f(p,t) + \frac{\partial}{\partial p_j} [B_{ij}(p) f(p,t)] \} \tag{5.10}$$

(using the notations of Ref. [119]). The HQ transport coefficients are defined as weighted

[5]Note that $i\Sigma^{>}(p,\varepsilon(p),t) f(\mathbf{p},t) = \int \frac{d^3\mathbf{k}}{(2\pi)^3} [w(\mathbf{p},\mathbf{k}) f(\mathbf{p},t)]$. Also, when converting the gain term $\Sigma_Q^{<} G_Q^{>}$ to Boltzmann form, it is necessary to use $T(E,\mathbf{P},\mathbf{p},\mathbf{p}') = T(E,\mathbf{P},\mathbf{p}',\mathbf{p})$.

averages over the momentum function,

$$A_i(p) = \int \frac{d^3\mathbf{k}}{(2\pi)^3} w(\mathbf{p},\mathbf{k}) k_i$$
$$B_{ij}(p) = \int \frac{1}{2}\frac{d^3\mathbf{k}}{(2\pi)^3} w(\mathbf{p},\mathbf{k}) k_i k_j. \tag{5.11}$$

In the local equilibrium medium, the HQ transport coefficients, such as drag coefficients $A(p)$ and transverse/longitudinal diffusion coefficients B_0/B_1, are defined through

$$A_i(p) = A(p) p_i$$
$$B_{ij}(p) = B_0(p) P^{\perp}_{ij} + B_1(p) P^{\parallel}_{ij}, \tag{5.12}$$

with the projectors defined as: $P^{\perp}_{ij} = \delta_{ij} - p_i p_j/\mathbf{p}^2$, and $P^{\parallel}_{ij} = p_i p_j/\mathbf{p}^2$. These scalar transport coefficients are weighted integrals

$$\langle X(\mathbf{p}')\rangle \equiv \int \frac{d^3\mathbf{k}}{(2\pi)^3} w(\mathbf{p},\mathbf{k}) X(\mathbf{p}') \tag{5.13}$$

with the coefficients $A(p)$,$B_0(p)$,$B_1(p)$ given by

$$A(p) = \langle 1 - \frac{\mathbf{p}\cdot\mathbf{p}'}{\mathbf{p}^2}\rangle$$
$$B_0(p) = \frac{1}{2}\langle p'^2 - \frac{(\mathbf{p}\cdot\mathbf{p}')^2}{\mathbf{p}^2}\rangle$$
$$B_1(p) = \frac{1}{2}\langle \frac{(\mathbf{p}\cdot\mathbf{p}')^2}{\mathbf{p}^2} - 2\mathbf{p}\cdot\mathbf{p}' + \mathbf{p}^2\rangle \tag{5.14}$$

and the correspondingly $\langle X(\mathbf{p}')\rangle$. Using the expression for $w(\mathbf{p},\mathbf{k})$ in Eq. (5.9) with the replacement $\mathbf{k} - \mathbf{p} \to \mathbf{p}'$, and switching the integration variable to $\mathbf{p}'$, we express $\langle X(\mathbf{p}')\rangle$ in T-matrix form

$$\begin{aligned}\langle X(\mathbf{p}')\rangle = &\sum_i \frac{1}{2\varepsilon_Q(p)} \int \frac{d\mathbf{p}' d\omega'}{(2\pi)^3 2\varepsilon_Q(p')} \frac{d\nu d^3\mathbf{q}}{(2\pi)^3 2\varepsilon_i(q)} \frac{d\nu' d^3\mathbf{q}'}{(2\pi)^3 2\varepsilon_i(q)} \\ &\times \delta^{(4)} \frac{(2\pi)^4}{d_Q} \sum_{a,l,s} |M|^2 \rho_Q(\omega', p') \rho_i(\nu, q) \rho_i(\nu', q') \\ &\times (1 - n_Q(\omega')) n_i(\nu) (1 \pm n_i(\nu')) X(\mathbf{p}').\end{aligned} \tag{5.15}$$

The $\sum_i$ is over all light flavors $u, \bar{u}$, $d, \bar{d}$, $s, \bar{s}$ and g, where the light and strange quarks are taken to have the same mass. We include the relativistic phase factor with the single-particle on-shell energy, denoted by $\varepsilon_{Q,i}(P)$. The matrix elements $|M|^2$ in Eq. (5.15) are related to the T-matrix in the center of mass (CM) frame as

$$\begin{aligned}&\sum_{a,l,s} \left|M^2\right| = [2\varepsilon_Q(p_{\text{cm}})][2\varepsilon_i(p_{\text{cm}})][2\varepsilon_Q(p'_{\text{cm}})][2\varepsilon_i(p'_{\text{cm}})] d_s^{Qi} \\ &\times \sum_a d_a^{Qi} \left| 4\pi \sum_l (2l+1) T_{Q,i}^{a,l}(E_{\text{cm}}, p_{\text{cm}}, p'_{\text{cm}}) P_l\left(\cos\theta_{\text{cm}}\right) \right|^2,\end{aligned} \tag{5.16}$$

where $T_{Q,i}^{a,l}(E_{\text{cm}}, p_{\text{cm}}, p'_{\text{cm}})$ is the T-matrix calculated in the CM frame in color channel a and partial-wave channel l. The CM energy E_{cm}, incoming momentum p_{cm}, outgoing momentum p'_{cm}, and angle $\cos\theta_{\text{cm}}$ are expressed as functions of E, $\mathbf{p}$, $\mathbf{q}$, $\mathbf{p}'$, $\mathbf{q}'$, as discussed in Sec. 2.3. The two-body color/spin degeneracy factor is denoted as $d_{a,s}^{Qi}$. The $P_l\left(\cos\theta_{\text{cm}}\right)$ are Legendre polynomials, but the partial-wave resummation is different from that described in Ref. [67], Eq. (8), and in Refs. [68, 70].[6] We can express the square of a partial wave summation as a partial wave expansion: $\left|\sum_l (2l+1) c_l P_l(x)\right|^2 = \sum_l (2l+1) b_l P_l(x)$, where each b_l is a function of the $\{c_l\}$.[7] In this work, we include 9 partial-wave ampli-

[6] $64\pi^2 = d_s^{Qi}(4\pi)^2$, and $(s - m_q^2 + m_Q^2)^2(s + m_q^2 - m_Q^2)^2)/s^2 = 16\varepsilon_Q(p_{\text{cm}})\varepsilon_q(p_{\text{cm}})\varepsilon_Q(p_{\text{cm}})\varepsilon_q(p_{\text{cm}})$.

[7] It is possible to derive these relations with a large number of partial waves using Mathematica or other computer algebra system (CAS).

tudes, $c_0, \ldots, c_8$ for the evaluation of transport coefficients. However, for the partial waves of the amplitude squared, keeping only the first few coefficients b_0, b_1 and b_2, is sufficient for convergence.

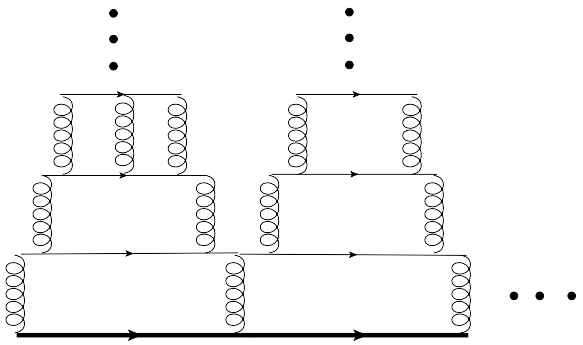

Figure 5.3: An example of a many-body diagram.

5.3.2 Charm Quark Transport Coefficients

In this section, we discuss the resulting transport coefficients, in particular, the drag coefficient $A(p)$ that characterizes the relaxation rate for the charm quark at each momentum. We focus on the results for the SCS and WCS. In Sec. 5.3.4, drag coefficients calculated using free energy as the potential kernel are compared to those calculated using the internal energy as the potential kernel.

As shown in Fig 5.4 (upper left), for small momentum, the drag coefficients of the SCS, $A_s(p)$, are approximately three times larger than those of the WCS, $A_w(p)$, at $T = 0.194\,\text{GeV}$, while $A_s(p)$ is only 15 percent larger than $A_w(p)$ at $T = 0.400\,\text{GeV}$. A key reason for this large enhancement at low momentum and low temperature is the remnant of the long-range confining force—as shown in Figs. 5.1 and 5.2. It allows the charm quark to interact with more neighboring partons. At higher temperatures, the confining

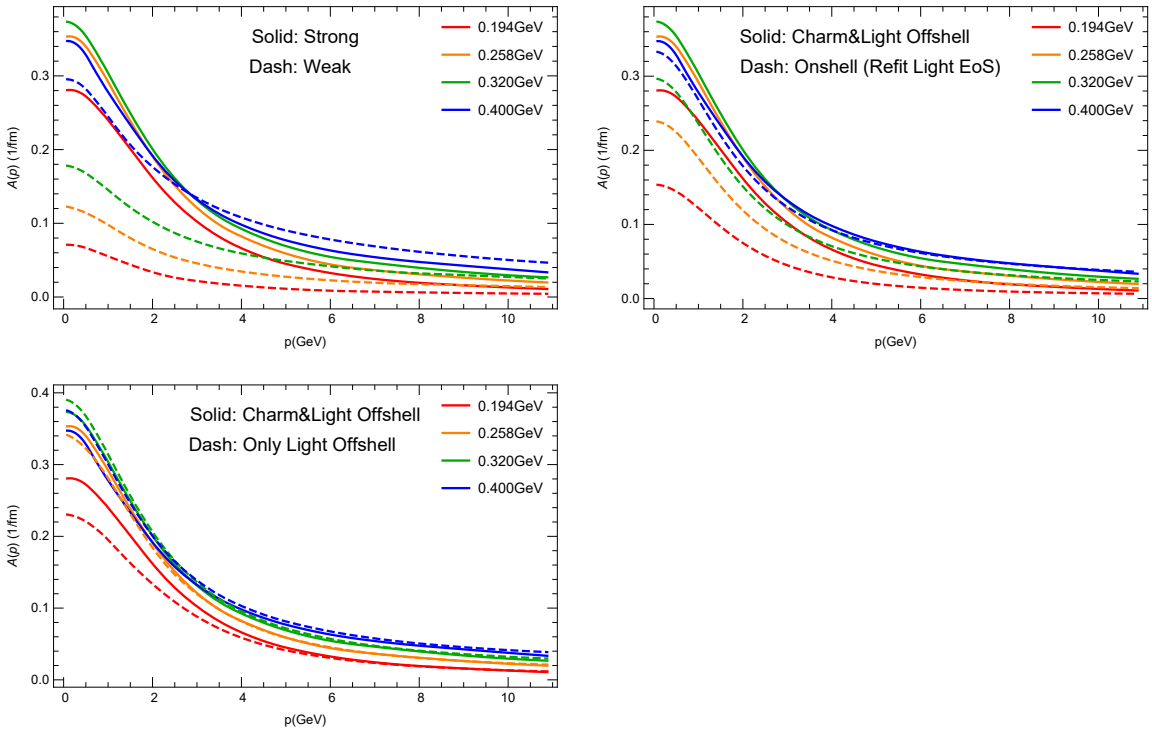

Figure 5.4: Friction coefficients $A(p)$, as a function of the incoming HQ 3-momentum, for four temperatures. First row: (left) the full off-shell cases for the SCS and WCS are compared; (right) the full off-shell case of the SCS is compared to the on-shell light-parton case. In the second row, two off-shell SCS cases are compared: those using full off-shell and those using off-shell light parton with outgoing on-shell charm quarks.

potential is much more screened, and the higher thermal momentum probes the force at shorter distances, similar for the WCS and SCS, so that the difference between $A_s(p)$ and $A_w(p)$ is reduced. Another reason for the enhancement are large off-shell effects due to the large widths of the spectral functions. This is a genuine many-body effect, since the width of the parton is caused by many-body collisions—as illustrated in Fig. 5.3. To elucidate the effects, we compare the drag coefficients with and without off-shell physics in the upper right panel of Fig. 5.4, where the off-shell effects almost double the transport coefficients in the small momentum and low temperature region. This large effect is partly due to a thermal enhancement, since a broadening of the spectral functions allows to probe

off-shell energies in the low energy region where the thermal factor is enhanced exponentially. Besides the thermal enhancements, the broad spectral functions allow the integral to probe the strong bound state significantly below the threshold in the off-shell T-matrices, which also significantly enhances the transport coefficients. This extends the original findings discussed in Refs. [50, 67, 68]—the resonance near the threshold is very efficient in thermalizing the heavy quark. The lower panel of Fig. 5.4 is a plot comparing full off-shell results to results that only include off-shell effects for light quarks (with on-shell outgoing charm quark), which demonstrate the effects of using an off-shell outgoing charm quark. This additional off-shell effect results in a 20% enhancement of transport coefficients at low temperature, since the further enlargement of phase space accesses more contributions from deeply-bound resonance states. However, if resonance states are close to threshold (or melt) so that the "on-shell" or "off-shell for light partons" setup already includes this resonance contribution, further off-shell treatment does not provide significant enhancement; this is indicated in the high temperature regions of the $A(p)$ plots—upper right and lower panels of Fig. 5.4. In the case of including the outgoing off-shell charm quarks, the thermal "enhancement" is actually a blocking effect that would otherwise cause the $A_s(p)$ of the full off-shell case to be smaller than that of the "off-shell for light partons" case at high temperature and low momentum. For the WCS, results from the full off-shell case agree well with results from the quasi-particle case, since the widths of spectral functions are small.

At high momentum, the HQ drag coefficients are dominated by the Coulomb term, which are intensified by relativistic corrections (Breit enhancement for the Coulomb term and suppression for the string term). Since the Coulomb screening mass for the WCS at high temperatures is smaller, for large momentum the $A_w(p)$ is larger than $A_s(p)$. For large momentum, the $A_s(p)$ of the full off-shell case tends to be closer to its quasi-particle case, since the spectral functions become more like those of quasi-particles for

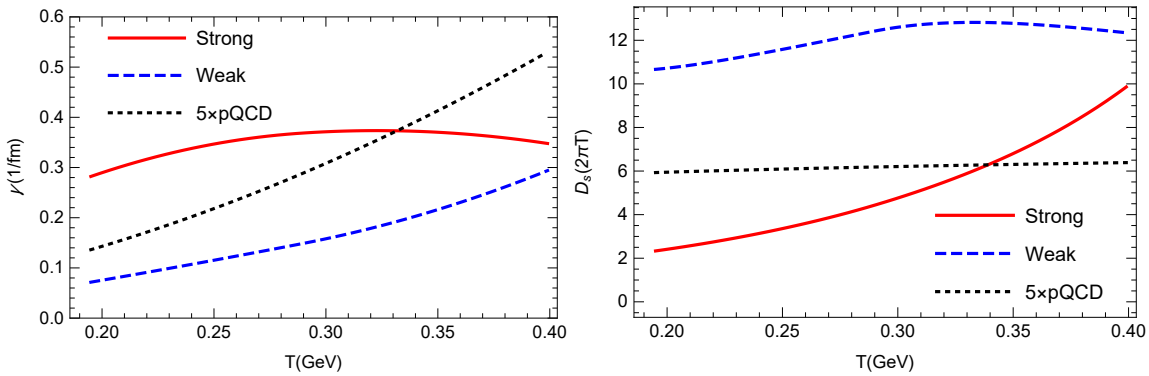

Figure 5.5: Temperature dependences of the relaxation rate, $\gamma = A(p)|_{p\to 0}$ (left), and the spatial diffusion coefficient, $D_s = T/(\gamma M_c)$ (right, in units of the thermal wave length $D_s(2\pi T)$). For pQCD results, we use $g = 2.24$, a Debye and thermal parton masses of gT, and a charm mass of 1.5 GeV. The pQCD cross sections are multiplied by 5 in order to present all curves on a similar scale.

large momentum—as discussed in Chapter 4.

Figure 5.5 illustrates the temperature dependence of the relaxation rate γ and spatial diffusion coefficient, $D_s(2\pi T)$, for the WCS and SCS. As a reference, we show the 5 times the perturbative QCD (pQCD)[8] relaxation rate and its corresponding spatial diffusion coefficients. The temperature behavior of the relaxation rates and spatial diffusion coefficients for the WCS is closer to the perturbative scenario, wherein γ increases monotonically with temperature, and $D_s(2\pi T)$ does not have a large temperature dependence. However, for the SCS, γ exhibits non-monotonic behavior; this can be understood as a competition between decreasing interaction strength and increasing density. The increase of $D_s(2\pi T)$ with temperature demonstrates that the coupling strength of the medium decreases as temperature increases. According to the plots of $D_s(2\pi T)$, at $T = 0.2$ GeV the strongly coupled solution is approximately 15 times stronger than the pQCD solution. In the SCS, the confining string term is crucial for the properties of the medium. Since the string tension carries a non-trivial dimension, the temperature behavior of γ and $D_s(2\pi T)$

[8]Born amplitudes with $\alpha_s = 0.4$.

are different than results of a scale-invariant approach—such as pQCD or AdS/CFT.

5.3.3 Langevin Simulation and Comparison to Experiments

The above transport coefficients have been implemented in Langevin simulations described in [113, 52] to obtain the D meson observables by our collaborator Min He [121]. Since our current calculations are limited to temperatures 0.194–0.400 GeV and momenta 0–10 GeV, an extrapolation is required for the implementation into the Langevin approach. Since the behavior of quasi-particle results is similar to full results at high momentum, as discussed in previous section, we extrapolate $A(p)$ to high momentum using its quasi-particle results and multiply them by a constant (with respect to momentum) to smoothly connect them. For extrapolation to lower and higher temperatures, we first extrapolate for $D_s(2\pi T)$ and M_c, as shown in Fig. 5.6. Then, we use $A(0) = T/(D_s M_c)$ for the extrapolation of $A(0)$ to lower and higher temperatures. The momentum dependence of $A(p)$ in this temperature region is taken to be the same as for $A(p)$ at $T = 0.194$ GeV (0.400 GeV) for low (high) temperature as shown in the two right panels of Fig. 5.6

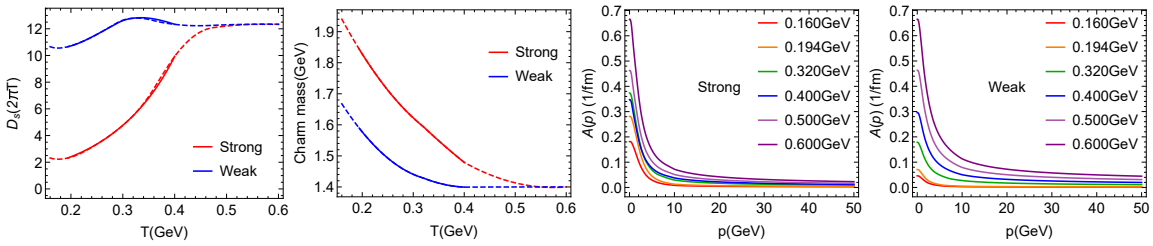

Figure 5.6: Extrapolation results for $D_s(2\pi T)$, M_c, $A_s(p)$ and $A_w(p)$ (from left to right).

After extrapolation, the transport coefficients are inserted into the Langevin equa-

tions [122]

$$d\mathbf{x} = \frac{\mathbf{p}}{\varepsilon_c} dt \tag{5.17}$$

$$d\mathbf{p} = \Gamma(p)\,\mathbf{p} dt + \sqrt{2dtD(p)}\boldsymbol{\rho}, \tag{5.18}$$

where the relaxation rate $\Gamma(p)$ and diffusion coefficient $D(p)$ are taken to be $\Gamma(p) = A(p)$ and $D(p) = B_0(p) = B_1(p) = T\varepsilon_c(p)\Gamma(p)$, and $\boldsymbol{\rho}$ is a random number determined from the Gaussian distribution function $P(\boldsymbol{\rho}) = (2\pi)^{-3/2} e^{-\boldsymbol{\rho}/2}$. Using the Langevin equations, we simulate Brownian motion of the charm quark in a background provided by hydrodynamic evolution of the QGP fireball. As shown in Fig. 5.7, the large drag slows down the heavy quarks which enhances the low-momentum spectra as demonstrated in the nuclear modification factor, R_{AA} (left panel). The drag force also pushes the heavy quarks to flow together with the medium, which generates the elliptic flow, v_2, of the heavy quarks (right panel).

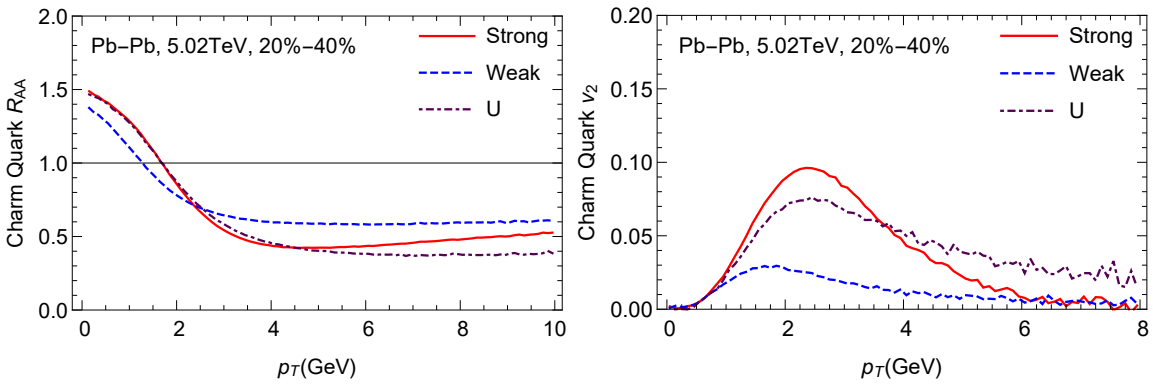

Figure 5.7: The R_{AA} (left panel) and v_2 (right panel) charm quarks.

As the fireball expands, the system approaches the pseudo-critical temperature. Charm

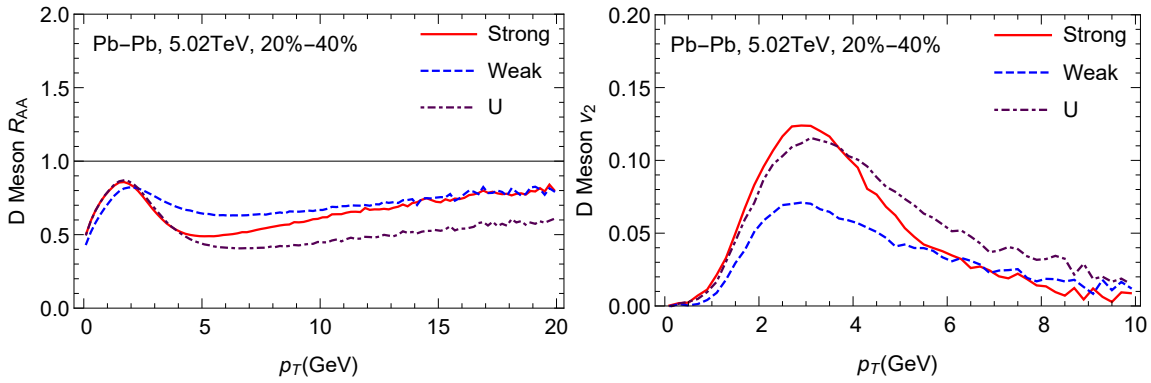

Figure 5.8: Comparison of the calculated D-meson $R_{\rm AA}$ and v_2 by a hydrodynamic simulation for Pb-Pb collision at the LHC [6].

quarks hadronize into D mesons through recombination with surrounding light quarks or independent fragmentation [123, 6]; this provides D-meson observables, as shown in Fig. 5.8. Recombination, acting as another interaction between charm quarks and the medium, drives D-meson spectra closer to equilibrium, thereby resulting in a depletion at very low p_T to develop a flow "bump" in the D-meson $R_{\rm AA}$ in the low p_T region. At high p_T, recombination yields to fragmentation, and consequently the D-meson $R_{\rm AA}$ tends toward that of the charm quark (modulo further suppression due to D-meson diffusion in hadronic-phase diffusion). Coalescence also enhances the D-meson v_2 by adding the thermalized light quark flow. These effects can be seen by comparing the v_2 of the charm quarks in Fig. 5.7 to the final D-meson v_2 in Fig. 5.8.

Comparing to experimental results [43, 44], we find that the observations prefer the SCS results and reject the WCS results, suggesting that the microscopic picture for QGP is closer to those described by the SCS. However, the predictions for the SCS are still below the experimental results—especially at high momentum, which indicates that radiative processes are important for the high momentum region [124]. It could also mean that the potential $\tilde{V}_s$ needs to be still larger than its current value. The R_{AA} and v_2 of the SCS

qualitatively agree with previous U results [70], even though the underlying physics is somewhat different i.e., drawing from different ranges of the underlying force. Also, as we have checked, the U result is not a self-consistent solution of the procedure described in the previous chapters. Therefore, in order to finally determine the underlying physics of QGP, we need information from both experiments and lQCD.

5.3.4 Comparing *V*, *F*, and *U*

The weakly coupled limit, F, and strongly coupled limit, U, of the potential have been utilized as limiting cases in various studies of HQ and quarkonium interactions in URHICs. Thus, it is necessary to illustrate the difference between our potentials V extracted from the self-consistent fit and the F, U. As shown in Fig. 5.4, we plot the force $-dV/dr$ in Fig. 5.9 and $\frac{3}{4}r^2 dV/dr$ in Fig. 5.10. The internal energy is strongest at short distances, the V_s (strong) is the largest at moderately long range. The weakly coupled solution V_w (weak) and F are quite similar at low temperature, but at high temperature V_w has a significantly stronger force than the free energy. In this section, transport coefficients will be calculated using the on-shell quasiparticle formalism, in order to isolate potential effects from off-shell effects. As shown in Fig. 5.11, the charm-quark mass is different, due to different infinite distance limits of the potentials, but the light-parton masses are chosen to be the same, obtained by a quasiparticle fit to EoS using the Fock mass ansatz [1] with V_s.

The results of the drag coefficients are shown in Fig. 5.12. At low momentum and low temperature, V_s and U both lead to large drag coefficients, when compared to F and V_w. As shown in Figs. 5.9 and 5.10, the force of V_s at long distance is comparable to that of U; their $A(p)$ at low momentum are also comparable, since low-momentum $A(p)$ probes the long range force. At high momentum, the $A(p)$ calculated using internal energy is much larger than others, which is due to its large force at short distances. Since V_s, V_w, and F have similar forces at short distances, they approach each other at high momentum. The

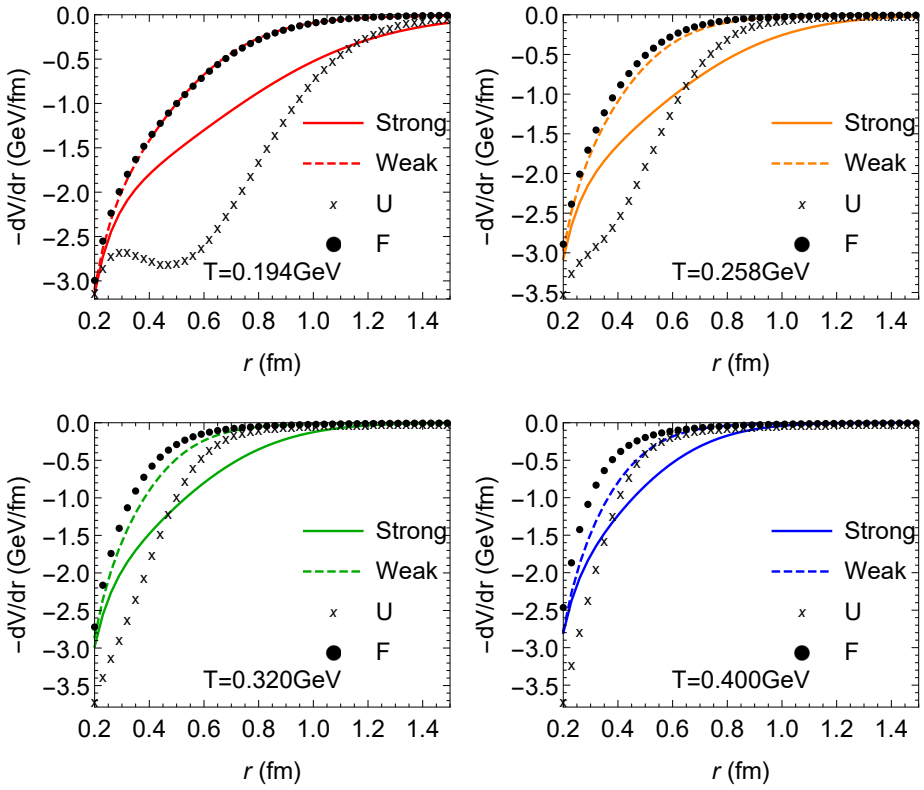

Figure 5.9: Force for V_s (solid line), V_w (dashed line), U (crosses) and F (dots) at different temperatures.

relaxation rate $\gamma = A(p)|_{p\to 0}$ and the spatial diffusion coefficients for all on-shell cases are shown in Fig. 5.13.

5.3.5 Perturbative vs Nonperturbative

Even though the QGP is a strongly coupled system that requires non-perturbative methods, there are some regions that may be studied perturbatively. In the calculation of the transport coefficients, there are three areas that require non-perturbative techniques: (1) the potential has a confining term with a long range force; (2) the resummation of the T-matrix that leads to the resonance contributions to the transport coefficients; (3) the off-shell effects from the large widths of the partons. In this section, we compare the full calculation of the drag coefficients with the coefficients that only include part of the above

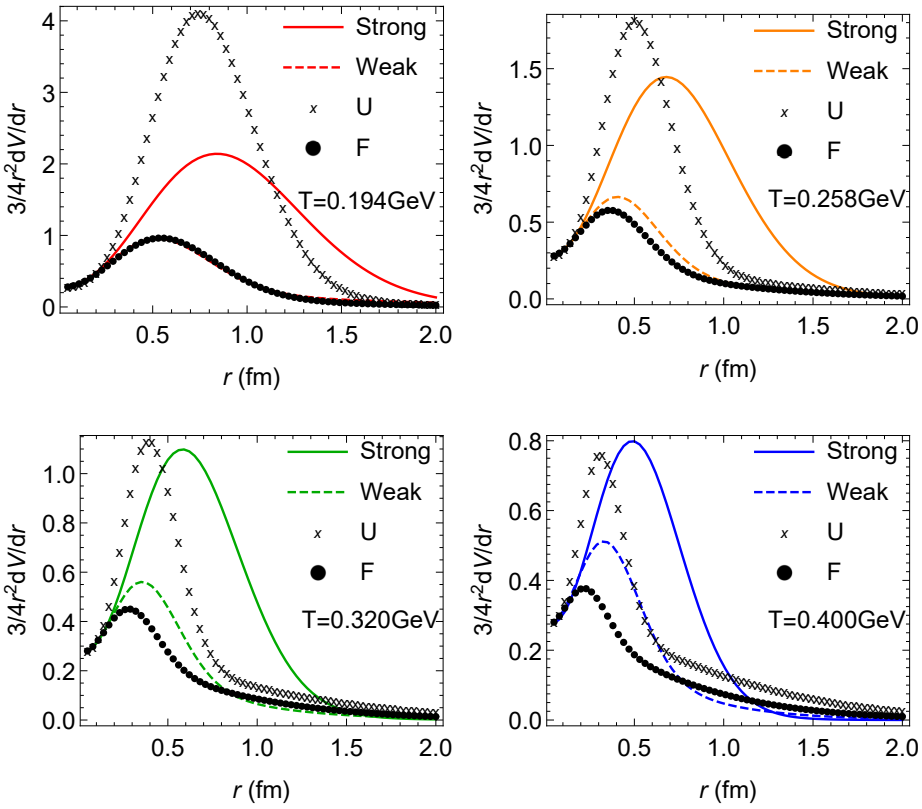

Figure 5.10: The quantity $\frac{3}{4}r^2dV/dr$ is dimensionless and scaled to recover the strong coupling constant, α_s at short distance. Here it is plotted for several potentials: V_s (solid line), V_w (dashed line), U (crosses) and F (dots).

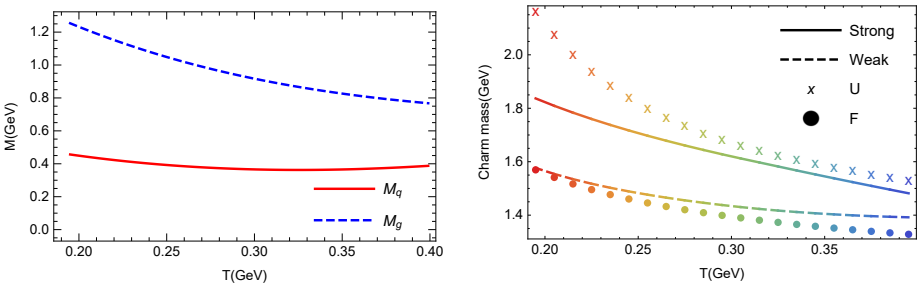

Figure 5.11: Light-parton masses (left) and charm-quark masses for V_s (solid line), V_w (dashed line), U (crosses) and F (dots) (right), used for the comprehensive calculations displayed in Figs 5.12 and 5.13.

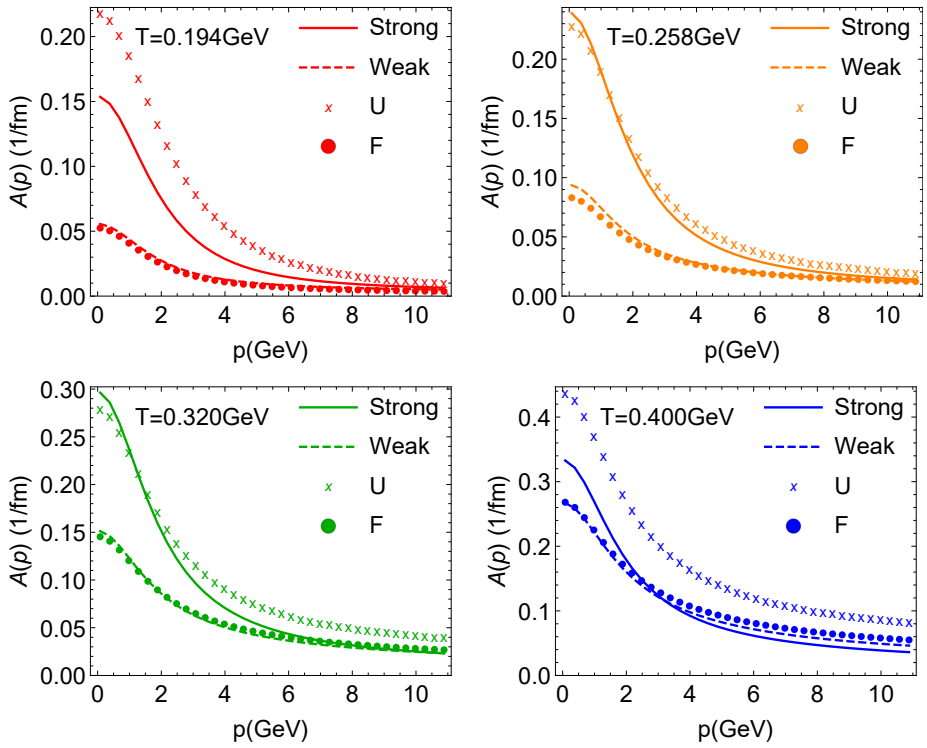

Figure 5.12: On-shell friction coefficients for V_s (solid line), V_w (dashed line), U (crosses) and F (dots).

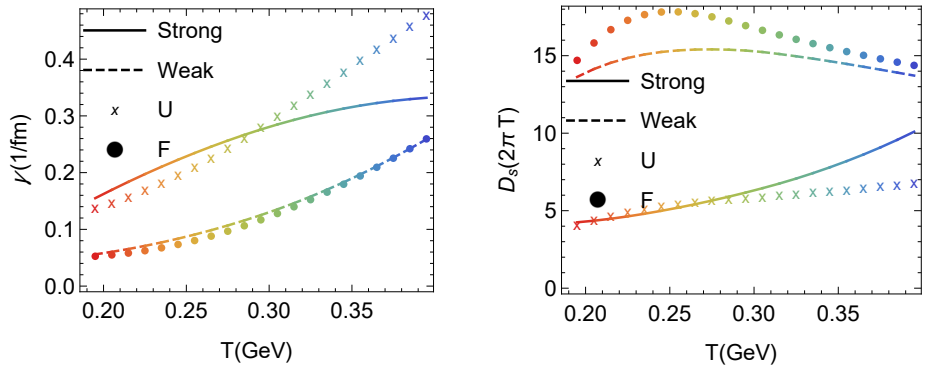

Figure 5.13: On-shell relaxation rates for V_s (solid line), V_w (dashed line), U (crosses) and F (dots) (left) and their corresponding spatial diffusion coefficients $D_s(2\pi T)$ (right).

non-perturbative physics, to highlight their effects.

As shown in Fig. 5.14, the "On-shell Born" and "On-shell" curves approach each other

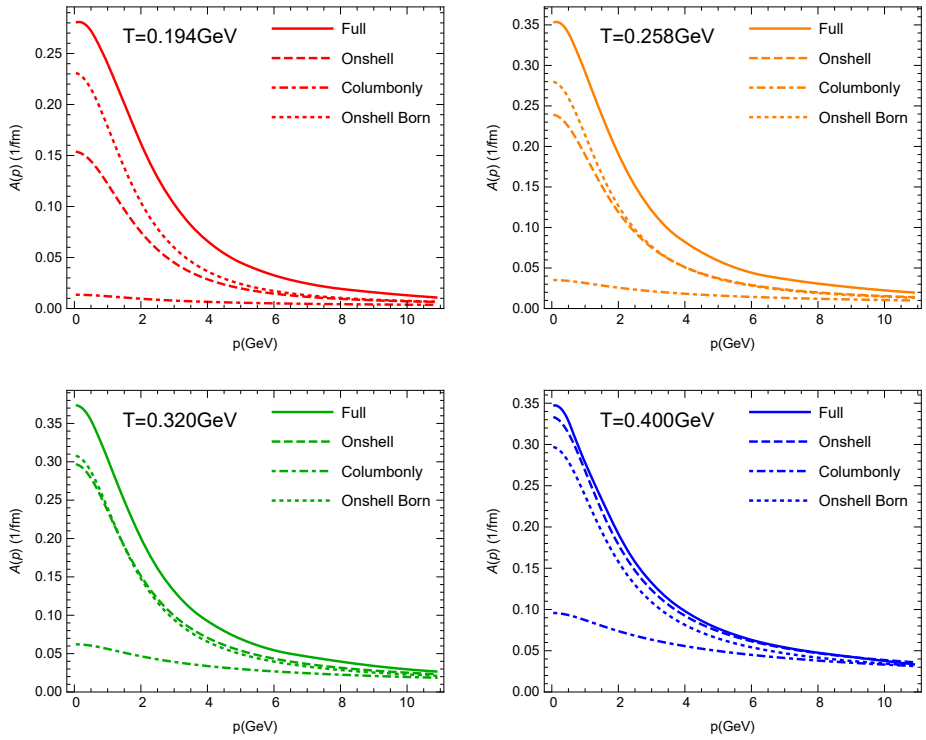

Figure 5.14: Comparison of the effects of different ingredients on the HQ transport coefficients. “Full” denotes full off-shell results for the SCS. “Coulomb only” describes on-shell results using only the Coulomb term in the potential. “Born” results only use the Born potential term without resummation (including the confining potential). Here, we use the quasi-particle mass shown in Fig. 5.11.

at high momentum. The reason for this may be related with the reason that Born approximation coincides with full solution and classical solution in non-relativistic Coulomb scattering. However, at low temperature the “Coulomb only” results are approximately $1/2$ of the “On-shell" and “On-shell Born" results. This suggests that even for high momentum charm quarks, there is still enough phase space from the soft momentum exchange to allow the confining force to contribute significantly to the friction coefficients. Therefore, the perturbative calculation of $A(p)$ (elastic) that does not effectively include the confining term may be unreliable at low temperatures—even at $p = 10\,\text{GeV}$. However, the drag coefficients for the full results are significantly larger than others, even at high momentum, when the temperature is low. This difference at high momentum may be due the different

medium parton properties in the off-shell case and the on-shell case at high momentum. The on-shell Born results are surprisingly close to full results within a few 10's of percents. This is, however, deceptive. If we include a second Born contribution, the drag coefficients will be five/two times larger at low/high momentum, indicating poor convergence of the perturbative series—in agreement with the findings of Ref. [125]. This is another reminder that a proper resummation in the nonperturbative region is mandatory.

5.4 Viscosity for Hydrodynamics

Besides the spatial diffusion coefficients, the shear viscosity is another important transport coefficients of the QGP. In the AdS/CFT approach [42], it is conjectured that the shear viscosity to entropy ratio has a lower bound, $4\pi\eta/s = 1$. Here, we calculate the viscosity η in our approach using the Kubo formula for the energy-momentum tensor. Using the leading-density energy-momentum tensor [126] with relativistic extension, the viscosity is expressed as

$$\eta = \lim_{\omega\to 0}\sum_i \frac{\pi d_i}{\omega}\int \frac{d^3\mathbf{p}d\lambda}{(2\pi)^3}\frac{p_x^2 p_y^2}{\varepsilon_i^2(p)}\rho_i(\omega+\lambda,p)\rho_i(\lambda,p)[n_i(\lambda)-n_i(\omega+\lambda)]\,, \tag{5.19}$$

where d_i denotes the partons' degeneracies, and $n_i(\omega)$ denotes their thermal distribution functions. Higher-order corrections are expected to be small [127, 128, 129, 130], which we have verified within our approach.

The dimensionless quantities $\mathcal{D}_s(2\pi T)$ and $4\pi\eta/s$ characterize the interaction strength of the bulk medium, which are shown in the left panel of Fig 5.15. The SCS has a small transport coefficient that increases as temperature increases, which demonstrates a strongly coupled medium at low temperature slowly transitioning into a more weakly coupled medium. The WCS has quite a large value for the transport coefficient, and it is almost constant with respect to temperature, which is not favored by the phenomenologi-

cal extraction of the transport coefficients from experiments [131, 132]. The ratio of these two dimensionless transport coefficients has been suggested to characterize the medium [133] and is shown in the right panel of Fig 5.15. This ratio is believed to be close to 1 in the strongly coupled limit [42, 134] and 5/2 in a weakly region accessible through perturbation theory [135]. The tendency of the SCS is a smooth transition between these two regions as temperature increases. On the other hand, the WCS has a ratio close to 5/2 over the entire temperature range, in agreement with the above insights.

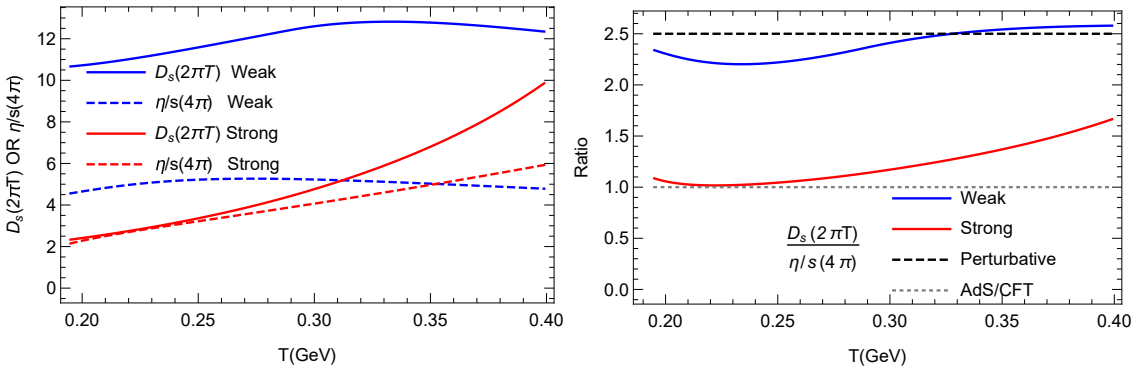

Figure 5.15: The $D_s(2\pi T)$ and $\eta/s(4\pi)$ for both SCS and WCS cases (left); The ratio of $D_s(2\pi T)$ to $\eta/s(4\pi)$ for both SCS and WCS cases (right), compared to the putative strongly and weakly coupled limits.Reprinted from [7].

6. CONCLUSION AND PERSPECTIVE*

We have set up a selfconsistent thermodynamic T-matrix approach to study the bulk and microscopic properties of the QGP in a unified framework, encompassing both light- and heavy-flavor degrees of freedom. Starting from an effective partonic Hamiltonian with a universal color force, including remnants of the confining force and relativistic corrections, we have computed one- and two-body thermodynamic Green's and spectral functions selfconsistently, treating bound and scattering states on an equal footing. Compared to earlier works, a full off-shell treatment is implemented to account for quantum many-body effects more rigorously, in particular the collisional widths of the QGP constituents. Moreover, our approach enables systematic constraints on the inputs to the Hamiltonian, *i.e.*, the two-body potential and two effective light-parton mass parameters, by comparing to a variety of lattice-QCD data.

Our calculation of the equation of state has been carried out in the LWB formalism with selfconsistently computed light-parton selfenergies and T-matrices. Importantly, we managed to resum the Luttinger-Ward functional using a matrix-log technique, which is critical to account for the dynamical formation of bound (or resonance) states in the thermodynamics of the system. The main constraints on the two-body driving kernel are derived from the HQ free energy, $F_{Q\bar{Q}}$, which we have also computed selfconsistently from the T-matrix for static quarks embedded in the QGP. Based on a parametric ansatz for an in-medium Cornell potential, we have fitted lattice-QCD data for $F_{Q\bar{Q}}$ and further checked our results against euclidean correlator ratios in the bottomonium and charmonium sectors. Together with the EoS, for which the fit of pertinent lQCD data can be largely controlled through the two bare light-parton masses in the Hamiltonian, this constitutes a compre-

*Part of this chapter is reprinted with permission from "T-matrix approach to quark-gluon plasma" by Shuai Y. F. Liu and Ralf Rapp, 2018, Phys. Rev. C **97**, 034918, Copyright 2018 by APS.

hensive quantum many-body framework for light and heavy partons and their two-body correlations in the QGP. We have solved this problem through a multi-layered numerical iteration procedure in our fit to 3 sets of lQCD data, where a typical accuracy at a few-percent level can be achieved. The main predictive power of the approach resides in the emerging spectral and transport properties of the QGP, including the prevalent degrees of freedom in the EoS.

In our construction of selfconsistent solutions, it turns out that the above set of lQCD constraints does not uniquely specify the input for the driving kernel. We have classified its possible range by a weakly- and a strongly-coupled solution. In the former, the input potential comes close to a lower limit set by the HQ free energy itself (not unlike what has been discussed based on direct Bayesian extraction methods [71]). The resulting light-parton spectral functions have rather moderate widths, well below their masses, and thus yield well-defined quasiparticles, as well as rather sharp but loosely bound resonances near T_c. The latter remain subleading, at a 10% level, in their contribution to the EoS. In contrast, the strongly-coupled solution is characterized by a potential that appreciably exceeds the free energy (not unlike recent lQCD extractions reported in Ref. [136]). The emerging partonic spectral widths are much enhanced; they become comparable to the parton masses and thus dissolve quasiparticle structures for low-momentum modes near T_c. At the same time, broad but well-defined two-particle bound states (mesons) emerge and become the leading contribution to the EoS, thus signaling a transition in the degrees of freedom in the system. At high momenta, parton quasiparticles reemerge and bound-state correlations are much suppressed. This solution, in particular, critically hinges on a proper treatment of the quantum effects induced by the large scattering rates.

While we believe that the strongly coupled solution is clearly the more attractive one (including its transition from quarks to hadrons and a qualitatively liquid-like behavior with interaction energies comparable to the parton masses), a more quantitative charac-

terization of this notion is in order. Therefore, we have applied the SCS and WCS to investigate the HQ transport problem. With a generalization to include the off-shell effects for HQ transport coefficients based on the Kadanoff-Baym equation, we find the drag coefficients of the SCS to be significantly larger than for the WCS in the low-momentum and low-temperature region. Using these transport coefficients in HQ Langevin simulations, the calculated heavy-meson spectra show a v_2 that is significantly larger in the SCS than in the WCS. The former is favored by the experimental data. We have also calculated the ratio η/s. We find that the η/s of the SCS has a promisingly small value, while the η/s for the WCS is again unfavorable in hydrodynamic phenomenological studies. Comparing the phenomenology using these transport coefficients with experimental data allows us to conclude that the quantum microscopic picture of the QGP is closer to that described by the SCS. Another simple insight is supporting this conclusion: Converting the heavy-quark diffusion coefficient into a thermalization and scattering rate, one can straightforwardly deduce that values of $2\pi T\mathcal{D}_s \simeq 3$ translate into quark scattering rates of order 1 GeV; this implies the dissolution of light quasiparticles, fully consistent with our numerical findings. The large widths also require the underlying potential V to markedly exceed the free energy, $F_{Q\bar{Q}}$, independent of model details [57].

For future applications, an ambitious line is to test the predicted spectral properties more directly; in the quarkonium sector this presumably requires the formulation of quantum transport approaches for heavy-ion collisions as recently discussed in the literature [137, 138, 139, 140, 141], which, in turn, can take advantage of heavy-quark diffusion properties computed with the same underlying interaction. The most direct connection remains the dilepton production rate, where again constraints from lQCD data can be straightforwardly utilized. Another area accessible to our approach is the investigation of finite chemical potential in the QCD phase diagram, starting with the calculation of quark susceptibilities. However, the description of phenomena associated with dynamical chi-

ral symmetry breaking, which are expected to become important at temperatures below $T \simeq 0.185$ GeV [142], will require an extension of the current formalism to explicitly include condensation mechanisms. This is more challenging but, we believe, still feasible.

REFERENCES

[1] S. Y. F. Liu and R. Rapp, Phys. Rev. C **97**, 034918 (2018).

[2] A. Mocsy, P. Petreczky, and M. Strickland, Int. J. Mod. Phys. A **28**, 1340012 (2013).

[3] G. Aarts, C. Allton, M. B. Oktay, M. Peardon, and J.-I. Skullerud, Phys. Rev. D **76**, 094513 (2007).

[4] G. Aarts *et al.*, JHEP **11**, 103 (2011).

[5] HotQCD Collaboration, A. Bazavov *et al.*, Phys. Rev. D **90**, 094503 (2014).

[6] M. He, R. J. Fries, and R. Rapp, Phys. Lett. B **735**, 445 (2014).

[7] S. Y. F. Liu and R. Rapp, EPJ Web Conf. **172**, 05001 (2018).

[8] E. V. Shuryak and I. Zahed, Phys. Rev. D **70**, 054507 (2004).

[9] P. W. Anderson, Science **177**, 393 (1972).

[10] M. E. Peskin and D. V. Schroeder, *An Introduction to quantum field theory* (Addison-Wesley, Reading, USA, 1995).

[11] K. G. Wilson, Phys. Rev. D **10**, 2445 (1974), [,45(1974)].

[12] E. V. Shuryak, World Sci. Lect. Notes Phys. **71**, 1 (2004), [World Sci. Lect. Notes Phys.8,1(1988)].

[13] E. Eichten *et al.*, Phys. Rev. Lett. **34**, 369 (1975).

[14] E. Eichten, K. Gottfried, T. Kinoshita, K. D. Lane, and T.-M. Yan, Phys. Rev. D **17**, 3090 (1978), [Erratum: Phys. Rev.D21,313(1980)].

[15] E. Eichten, K. Gottfried, T. Kinoshita, K. D. Lane, and T.-M. Yan, Phys. Rev. D **21**, 203 (1980).

[16] S. Godfrey and N. Isgur, Phys. Rev. D **32**, 189 (1985).

[17] S. Capstick and N. Isgur, Phys. Rev. D **34**, 2809 (1986), [AIP Conf. Proc.132,267(1985)].

[18] G. S. Bali and K. Schilling, Phys. Rev. D **46**, 2636 (1992).

[19] CMS, V. Khachatryan *et al.*, Phys. Lett. B **765**, 193 (2017).

[20] R. Rapp and E. V. Shuryak, Phys. Lett. B **473**, 13 (2000).

[21] R. Rapp, Phys. Rev. C **63**, 054907 (2001).

[22] PHENIX, A. Adare *et al.*, Phys. Rev. Lett. **98**, 172301 (2007).

[23] STAR, B. I. Abelev *et al.*, Phys. Rev. Lett. **98**, 192301 (2007), [Erratum: Phys. Rev. Lett.106,159902(2011)].

[24] ALICE, B. Abelev *et al.*, Phys. Rev. Lett. **109**, 072301 (2012).

[25] T. Matsui and H. Satz, Phys. Lett. B **178**, 416 (1986).

[26] L. Grandchamp and R. Rapp, Phys. Lett. B **523**, 60 (2001).

[27] Y.-p. Liu, Z. Qu, N. Xu, and P.-f. Zhuang, Phys. Lett. B **678**, 72 (2009).

[28] X. Zhao and R. Rapp, Nucl. Phys. A **859**, 114 (2011).

[29] T. Song, K. C. Han, and C. M. Ko, Phys. Rev. C **84**, 034907 (2011).

[30] R. Rapp and X. Du, Nucl. Phys. A **967**, 216 (2017).

[31] M. E. Peskin, Nucl. Phys. B **156**, 365 (1979).

[32] G. Bhanot and M. E. Peskin, Nucl. Phys. B **156**, 391 (1979).

[33] Y. Liu, C. M. Ko, and T. Song, Phys. Rev. C **88**, 064902 (2013).

[34] S. Chen and M. He, Phys. Rev. C **96**, 034901 (2017).

[35] X. Du, R. Rapp, and M. He, Phys. Rev. C **96**, 054901 (2017).

[36] CMS, S. Chatrchyan *et al.*, Phys. Rev. Lett. **109**, 222301 (2012).

[37] STAR, K. H. Ackermann *et al.*, Phys. Rev. Lett. **86**, 402 (2001).

[38] D. Teaney, J. Lauret, and E. V. Shuryak, Phys. Rev. Lett. **86**, 4783 (2001).

[39] P. F. Kolb, P. Huovinen, U. W. Heinz, and H. Heiselberg, Phys. Lett. B **500**, 232 (2001).

[40] P. Romatschke and U. Romatschke, Phys. Rev. Lett. **99**, 172301 (2007).

[41] H. Song and U. W. Heinz, Phys. Rev. C **77**, 064901 (2008), 0712.3715.

[42] P. Kovtun, D. T. Son, and A. O. Starinets, Phys. Rev. Lett. **94**, 111601 (2005).

[43] ALICE, B. Abelev *et al.*, JHEP **09**, 112 (2012).

[44] ALICE, B. Abelev *et al.*, Phys. Rev. Lett. **111**, 102301 (2013).

[45] STAR, L. Adamczyk *et al.*, Phys. Rev. Lett. **113**, 142301 (2014).

[46] STAR, L. Adamczyk *et al.*, Phys. Rev. Lett. **118**, 212301 (2017).

[47] H. van Hees, V. Greco, and R. Rapp, Phys. Rev. C **73**, 034913 (2006).

[48] B. Svetitsky, Phys. Rev. D **37**, 2484 (1988).

[49] M. Golam Mustafa, D. Pal, and D. Kumar Srivastava, Phys. Rev. C **57**, 889 (1998), [Erratum: Phys. Rev.C57,3499(1998)].

[50] H. van Hees and R. Rapp, Phys. Rev. **C71**, 034907 (2005).

[51] G. D. Moore and D. Teaney, Phys. Rev. C **71**, 064904 (2005).

[52] M. He, R. J. Fries, and R. Rapp, Phys. Rev. Lett. **110**, 112301 (2013).

[53] Y. Aoki, G. Endrodi, Z. Fodor, S. D. Katz, and K. K. Szabo, Nature **443**, 675 (2006).

[54] S. Borsanyi *et al.*, JHEP **11**, 077 (2010).

[55] P. Petreczky and K. Petrov, Phys. Rev. D **70**, 054503 (2004).

[56] O. Kaczmarek and F. Zantow, Phys. Rev. D **71**, 114510 (2005).

[57] S. Y. F. Liu and R. Rapp, Nucl. Phys. A **941**, 179 (2015).

[58] S. Datta, F. Karsch, P. Petreczky, and I. Wetzorke, Phys. Rev. **D69**, 094507 (2004).

[59] A. Jakovac, P. Petreczky, K. Petrov, and A. Velytsky, Phys. Rev. D **75**, 014506 (2007).

[60] D. Cabrera and R. Rapp, Phys. Rev. D **76**, 114506 (2007).

[61] A. Mocsy and P. Petreczky, Phys. Rev. D **77**, 014501 (2008).

[62] HotQCD Collaboration, A. Bazavov *et al.*, Phys. Rev. D **86**, 034509 (2012).

[63] F. Karsch, E. Laermann, S. Mukherjee, and P. Petreczky, Phys. Rev. D **85**, 114501 (2012).

[64] J.-P. Blaizot, E. Iancu, and A. Rebhan, Thermodynamics of the high temperature quark gluon plasma, in *In *Hwa, R.C. (ed.) et al.: Quark gluon plasma* 60-122*, 2003.

[65] D. H. Rischke, Prog. Part. Nucl. Phys. **52**, 197 (2004).

[66] M. Mannarelli and R. Rapp, Phys. Rev. C **72**, 064905 (2005).

[67] H. van Hees, M. Mannarelli, V. Greco, and R. Rapp, Phys. Rev. Lett. **100**, 192301 (2008).

[68] F. Riek and R. Rapp, Phys. Rev. C **82**, 035201 (2010).

[69] F. Riek and R. Rapp, New J. Phys. **13**, 045007 (2011).

[70] K. Huggins and R. Rapp, Nucl. Phys. A **896**, 24 (2012).

[71] Y. Burnier, O. Kaczmarek, and A. Rothkopf, Phys. Rev. Lett. **114**, 082001 (2015).

[72] J. M. Luttinger and J. C. Ward, Phys. Rev. **118**, 1417 (1960).

[73] G. Baym and L. P. Kadanoff, Phys. Rev. **124**, 287 (1961).

[74] G. Baym, Phys. Rev. **127**, 1391 (1962).

[75] S. Y. F. Liu and R. Rapp, J. Phys. Conf. Ser. **779**, 012034 (2017).

[76] W. Lucha, F. F. Schoberl, and D. Gromes, Phys. Rept. **200**, 127 (1991).

[77] S. Y. F. Liu and R. Rapp, (2016), arXiv:1612.09138.

[78] E. E. Salpeter and H. A. Bethe, Phys. Rev. **84**, 1232 (1951).

[79] R. Blankenbecler and R. Sugar, Phys. Rev. **142**, 1051 (1966).

[80] R. H. Thompson, Phys. Rev. D **1**, 110 (1970).

[81] R. M. Woloshyn and A. D. Jackson, Nucl. Phys. B **64**, 269 (1973).

[82] F. J. Dyson, Phys. Rev. **85**, 631 (1952).

[83] S. Weinberg, *The quantum theory of fields. Vol. 2: Modern applications* (Cambridge University Press, 2013).

[84] L. P. Kadanoff and G. A. Baym, *Quantum statistical mechanics* (Benjamin, 1962).

[85] W.-D. Kraeft, D. Kremp, W. Ebeling, and G. Röpke, *Quantum statistics of charged particle systems* (Springer, 1986).

[86] P.-A. Pantel, D. Davesne, and M. Urban, Phys. Rev. A **90**, 053629 (2014), 1409.3482, [Erratum: Phys. Rev.A94,no.1,019901(2016)].

[87] J. I. Kapusta and C. Gale, *Finite-temperature field theory: Principles and applications* (Cambridge Univ. Press, 2006).

[88] R. Brockmann and R. Machleidt, Phys. Rev. C **42**, 1965 (1990).

[89] M. Schmidt, G. Röpke, and H. Schulz, Annals of Physics **202**, 57 (1990).

[90] R. Rapp and J. Wambach, Phys. Rev. **C53**, 3057 (1996).

[91] G. Lacroix, C. Semay, D. Cabrera, and F. Buisseret, Phys. Rev. D **87**, 054025 (2013).

[92] G. Lacroix, C. Semay, and F. Buisseret, Phys. Rev. C **91**, 065204 (2015).

[93] N. Nakanishi, Prog. Theor. Phys. Suppl. **43**, 1 (1969).

[94] G. E. Brown, A. D. Jackson, and T. T. S. Kuo, Nucl. Phys. A **133**, 481 (1969).

[95] R. Rapp and J. Wambach, Phys. Lett. B **315**, 220 (1993).

[96] R. Rapp and J. Wambach, Phys. Lett. B **351**, 50 (1995).

[97] G. E. Brown, C.-H. Lee, M. Rho, and E. Shuryak, Nucl. Phys. A **740**, 171 (2004).

[98] M. I. Haftel and F. Tabakin, Nucl. Phys. A **158**, 1 (1970).

[99] A. L. Fetter and J. D. Walecka, *Quantum theory of many-particle systems* (Courier Dover Publications, 2003).

[100] J. P. Blaizot, E. Iancu, and A. Rebhan, Phys. Rev. D **63**, 065003 (2001).

[101] D. Blaschke, A. Dubinin, and L. Turko, (2016), 1611.09845.

[102] J.-P. Blaizot and G. Ripka, *Quantum theory of finite systems* (MIT press Cambridge, 1986).

[103] R. Haussmann, W. Rantner, S. Cerrito, and W. Zwerger, Phys. Rev. A **75**, 023610 (2007).

[104] A. Rothkopf, T. Hatsuda, and S. Sasaki, Phys. Rev. Lett. **108**, 162001 (2012).

[105] A. Beraudo, J.-P. Blaizot, and C. Ratti, Nucl. Phys. A **806**, 312 (2008).

[106] M. Laine, O. Philipsen, P. Romatschke, and M. Tassler, JHEP **0703**, 054 (2007).

[107] A. Bazavov, Y. Burnier, and P. Petreczky, Nucl. Phys. A **932**, 117 (2014).

[108] L. D. Faddeev, Sov. Phys. JETP **12**, 1014 (1961), [Zh. Eksp. Teor. Fiz.39,1459(1960)].

[109] Y. Burnier, O. Kaczmarek, and A. Rothkopf, JHEP **12**, 101 (2015).

[110] E. Megias, E. Ruiz Arriola, and L. Salcedo, JHEP **0601**, 073 (2006).

[111] E. Megias, E. Ruiz Arriola, and L. Salcedo, Phys. Rev. D **75**, 105019 (2007).

[112] A. Beraudo, J. Blaizot, P. Faccioli, and G. Garberoglio, Nucl. Phys. A **846**, 104 (2010).

[113] M. He, R. J. Fries, and R. Rapp, Phys. Rev. C **86**, 014903 (2012).

[114] X. Zhao and R. Rapp, Phys. Rev. C **82**, 064905 (2010).

[115] Y. Liu, B. Chen, N. Xu, and P. Zhuang, Phys. Lett. B **697**, 32 (2011).

[116] A. Emerick, X. Zhao, and R. Rapp, Eur. Phys. J. A **48**, 72 (2012).

[117] M. Strickland and D. Bazow, Nucl. Phys. A **879**, 25 (2012).

[118] H. Berrehrah, E. Bratkovskaya, T. Steinert, and W. Cassing, Int. J. Mod. Phys. E **25**, 1642003 (2016).

[119] F. Prino and R. Rapp, J. Phys. G **43**, 093002 (2016).

[120] P. Danielewicz, Annals Phys. **152**, 239 (1984).

[121] S. Y. F. Liu, M. He, and R. Rapp, in prepartion (2018).

[122] M. He, H. van Hees, P. B. Gossiaux, R. J. Fries, and R. Rapp, Phys. Rev. E **88**, 032138 (2013).

[123] L. Ravagli and R. Rapp, Phys. Lett. B **655**, 126 (2007).

[124] S. Cao, G.-Y. Qin, and S. A. Bass, Phys. Rev. C **88**, 044907 (2013).

[125] S. Caron-Huot and G. D. Moore, Phys. Rev. Lett. **100**, 052301 (2008).

[126] D. N. Zubarev, *Nonequilibrium statistical thermodynamics* (Plenum Publishing Corporation, 1974).

[127] M. Iwasaki, H. Ohnishi, and T. Fukutome, (2006), hep-ph/0606192.

[128] M. Iwasaki, H. Ohnishi, and T. Fukutome, J. Phys. G **35**, 035003 (2008).

[129] R. Lang and W. Weise, Eur. Phys. J. A **50**, 63 (2014).

[130] S. Ghosh, Int. J. Mod. Phys. A **29**, 1450054 (2014).

[131] F. Scardina, S. K. Das, V. Minissale, S. Plumari, and V. Greco, Phys. Rev. C **96**, 044905 (2017).

[132] J. E. Bernhard, J. S. Moreland, S. A. Bass, J. Liu, and U. Heinz, Phys. Rev. C **94**, 024907 (2016).

[133] R. Rapp and H. van Hees, in *Quark-Gluon Plasma 4*, edited by R. Hwa and X. N. Wang, p. 111, World Scientific, Singapore, 2010, arXiv:0903.1096.

[134] S. S. Gubser, Phys. Rev. D **76**, 126003 (2007).

[135] P. Danielewicz and M. Gyulassy, Phys. Rev. D **31**, 53 (1985).

[136] P. Petreczky and J. Weber, Nucl. Phys. A **967**, 592 (2017).

[137] Y. Akamatsu, Phys. Rev. D **91**, 056002 (2015).

[138] J.-P. Blaizot, D. De Boni, P. Faccioli, and G. Garberoglio, Nucl. Phys. A **946**, 49 (2016).

[139] N. Brambilla, M. A. Escobedo, J. Soto, and A. Vairo, (2017), arXiv:1711.04515.

[140] D. De Boni, JHEP **08**, 064 (2017).

[141] J.-P. Blaizot and M. A. Escobedo, (2017), arXiv:1711.10812.

[142] T. Bhattacharya *et al.*, Phys. Rev. Lett. **113**, 082001 (2014).

[143] E. Shuryak and I. Zahed, Phys. Rev. D **69**, 046005 (2004).

APPENDIX A

POTENTIAL APPROXIMATION FOR LIGHT PARTONS

In this section we discuss several issues related to the implementation of the potential approximation for light-quark interactions. Historically, the Cornell potential has been a successful tool for quark-based hadron spectroscopy; 3D reductions of the 4D Bethe-Salpeter equation (BSE) are also widely used in effective hadronic approaches to hadronic vacuum physics, including light mesons like π-π interactions. In particular, the Cornell potential incorporates essential nonperturbative aspects of the QCD force, *i.e.*, a confining force. Our approach is a finite-temperature version of this framework, where remnants of the confining force will turn out to play a crucial role to render a strongly coupled system. The recovery of the vacuum vector-meson masses at low QGP temperatures in the SCS as shown in Sec. 4.2.4 (where the potential is close to its vacuum form) is a direct manifestation of a “realistic" vacuum limit of the approach in the light-quark sector. As we remarked in the text, interactions believed to be essential for spontaneous chiral symmetry breaking (such as instanton-induced forces) are not included, but we recall that recent lQCD computations have found that the effects of chiral symmetry breaking have essentially vanished once the temperature has reached about 30 MeV above the chiral crossover temperature, $T_{\rm pc}^{\chi} \simeq 0.155\,$GeV [142].

There are several further considerations. The reduction of the relativistic 4D Bethe-Salpeter equation (BSE) [78] into 3D scattering equations has been scrutinized, *e.g.*, in Ref. [81] and discussed in Sec. 2.1. In particular, within in the Blankenbecler-Sugar (BbS) scheme [79] as shown in Eq. (2.4) and Eq. (2.5), the BSE can be equivalently separated into two coupled equations, where the kernel of the first (leading) equation is potential-like, while the second (subleading) equation quantifies the off-energy-shell corrections to the

potential kernel. The philosophy is to expand the BSE around the potential solution using a parametrically small correction $GG - \mathcal{E}_{(2)}$ in Eq. (2.5) (R_2V in Ref. [79]), rather than to expand around the free-wave solution using the coupling constant and/or velocity (as in NRQCD) as a small parameter. In particular, such an expansion does not rely on a non-relativistic hierarchy. This series usually exhibits a fast convergence [79, 81], suggesting that the leading potential solution is already close to the full solution. In many cases, the higher-order off-shell corrections can be effectively absorbed in an adjustment of the potential. In the present case, the fits of the potential to lQCD data may approximately encode such corrections. Finally, we recall that for $2 \to 2$ on-shell scattering in the CM system the in- and outgoing momenta moduli of the particles are equal, *i.e.*, there is no energy transfer in the collision. We also recall that while the two-body interaction is approximated by an instantaneous force, the many-body quantum approach fully accounts for the dynamics (energy dependence) of the one- and two-particle propagators (and T-matrices) in the system. Additional considerations can be found in Refs. [8, 143].